

Science and Technology of Nuclear Installations

# Subchannel Analysis, CFD Modeling and Verifications, CHF Experiments and Benchmarking

Guest Editors: Baowen Yang, Yassin A. Hassan,  
Jianqiang Shan, Bin Zhang, Junli Gou, and Liangzhi Cao





---

**Subchannel Analysis, CFD Modeling  
and Verifications, CHF Experiments  
and Benchmarking**

Science and Technology of Nuclear Installations

---

**Subchannel Analysis, CFD Modeling  
and Verifications, CHF Experiments  
and Benchmarking**

Guest Editors: Baowen Yang, Yassin A. Hassan, Jianqiang Shan,  
Bin Zhang, Junli Gou, and Liangzhi Cao



---

Copyright © 2014 Hindawi Publishing Corporation. All rights reserved.

This is a special issue published in “Science and Technology of Nuclear Installations.” All articles are open access articles distributed under the Creative Commons Attribution License, which permits unrestricted use, distribution, and reproduction in any medium, provided the original work is properly cited.

## Editorial Board

Nusret Aksan, Switzerland  
A. C. M. Alvim, Brazil  
Won Pil Baek, Republic of Korea  
Stephen M. Bajorek, USA  
George Bakos, Greece  
Jozsef Banati, Sweden  
Ricardo Barros, Brazil  
A. B. Salah, Belgium  
Giovanni B. Bruna, France  
Nikola Čavlina, Croatia  
Xu Cheng, China  
Leon Cizelj, Slovenia  
A. Clausse, Argentina  
Francesco D' Auria, Italy  
Marcos P. de Abreu, Brazil  
Giovanni Dell'Orco, France  
J. C. Ferreri, Argentina  
Nikolay Fil, Russia  
Cesare Frepoli, USA  
Giorgio Galassi, Italy  
Regina Galetti, Brazil

Michel Giot, Belgium  
Valerio Giusti, Italy  
Horst Glaeser, Germany  
Satish Kumar Gupta, India  
Ali Hainoun, Syria  
Keith E. Holbert, USA  
Kostadin Ivanov, USA  
Yacine Kadi, Republic of Korea  
Ahmed Khedr, Egypt  
Tomasz Kozłowski, USA  
Tomoaki Kunugi, Japan  
Mike Kuznetsov, Germany  
H.-Y. Lee, Republic of Korea  
B. Limmeechokchai, Thailand  
Jiri Macek, Czech Republic  
Annalisa Manera, USA  
Borut Mavko, Slovenia  
Oleg Melikhov, Russia  
Rafael Miró, Spain  
JOZEF Misak, Czech Republic  
Rahim Nabbi, Germany

Manmohan Pandey, India  
Yuriy Parfenov, Russia  
Yves Pontillon, France  
Nik Popov, Canada  
Piero Ravetto, Italy  
Francesc Reventos, Spain  
Enrico Sartori, France  
Carlo Sborchia, France  
Massimo Sepielli, Italy  
Arkady Serikov, Germany  
James F. Stubbins, USA  
Iztok Tiselj, Slovenia  
Rizwan Uddin, USA  
Eugenijus Ušpuras, Lithuania  
Richard Wright, Norway  
Chao Xu, China  
X. George Xu, USA  
Yanko Yanev, Bulgaria  
Zhiwei Zhou, China  
Enrico Zio, Italy  
Massimo Zucchetti, Italy

# Contents

**Subchannel Analysis, CFD Modeling and Verifications, CHF Experiments and Benchmarking,**

Baowen Yang, Yassin A. Hassan, Jianqiang Shan, Bin Zhang, Junli Gou, and Liangzhi Cao

Volume 2014, Article ID 209747, 2 pages

**CFD Turbulence Study of PWR Spacer-Grids in a Rod Bundle,** C. Peña-Monferrer, J. L. Muñoz-Cobo, and S. Chiva

Volume 2014, Article ID 635651, 15 pages

**Uniform versus Nonuniform Axial Power Distribution in Rod Bundle CHF Experiments,** Baowen Yang,

Jianqiang Shan, Junli Gou, Hui Zhang, Aiguo Liu, and Hu Mao

Volume 2014, Article ID 462460, 9 pages

**Effect of Flow Blockage on the Coolability during Reflood in a  $2 \times 2$  Rod Bundle,** Kihwan Kim,

Byung-Jae Kim, Young-Jung Youn, Hae-Seob Choi,

Sang-Ki Moon, and Chul-Hwa Song

Volume 2014, Article ID 247862, 9 pages

**Subchannel Analysis of Wire Wrapped SCWR Assembly,** Jianqiang Shan, Henan Wang, Wei Liu,

Linxing Song, Xuanxiang Chen, and Yang Jiang

Volume 2014, Article ID 301052, 8 pages

**Direct Numerical Simulation and Visualization of Subcooled Pool Boiling,**

Tomoaki Kunugi and Yasuo Ose

Volume 2014, Article ID 120604, 11 pages

**Influence of Spacer Grid Outer Strap on Fuel Assembly Thermal Hydraulic Performance,** Jingwen Yan,

Yuxiang Zhang, Baowen Yang, Weicai Li, and Yuemin Zhou

Volume 2014, Article ID 602062, 9 pages

## Editorial

# Subchannel Analysis, CFD Modeling and Verifications, CHF Experiments and Benchmarking

**Baowen Yang,<sup>1</sup> Yassin A. Hassan,<sup>2</sup> Jianqiang Shan,<sup>1</sup> Bin Zhang,<sup>1</sup>  
Junli Gou,<sup>1</sup> and Liangzhi Cao<sup>1</sup>**

<sup>1</sup> School of Nuclear Science and Technology, Xi'an Jiaotong University, No. 28 Xianning West Road, Xi'an 710049, China

<sup>2</sup> 335Q Zachry Engineering Center, Department of Nuclear Engineering, Texas A&M University, College Station, TX 77843-3133, USA

Correspondence should be addressed to Baowen Yang; [bwy@mail.xjtu.edu.cn](mailto:bwy@mail.xjtu.edu.cn)

Received 29 June 2014; Accepted 29 June 2014; Published 20 July 2014

Copyright © 2014 Baowen Yang et al. This is an open access article distributed under the Creative Commons Attribution License, which permits unrestricted use, distribution, and reproduction in any medium, provided the original work is properly cited.

In the heart of light water reactors, though the nuclear fuel elements are a source of energy, they are also the root of potential threat for nuclear accidents. The investigation and understanding of the multiphase, multiphysics, and multiscale subchannel systems in the reactor core are the key to an economical and safe operation of a nuclear power plant. There are several unique features associated with such subchannel systems including strong interchannel interaction, flow structure coupling, nonuniform heat source (both axially and radially), periodic flow obstruction and mixing through mixing vane grids along the length of fuel assembly, and strong multiphysics coupling. These unique features present the upmost challenging and critical task for nuclear fuel efficiency and safety. As one of the most active areas of nuclear thermal-hydraulics, research on subchannel analysis and CFD modeling and verifications, as well as rod bundle CHF experiments and benchmarking is of great interest to the nuclear fuel design and reactor safety. Due to the technical difficulty, time consumption, and high cost involved in the conventional large scale subchannel mixing and rod bundle CHF experiments for light water reactors, CFD modeling has become the major trend in predicting the local conditions in complicated subchannel geometry. The advancements in CFD modeling from single phase turbulent mixing to multiphase CFD modeling techniques involving Euler-Euler two-fluid modeling, large Eddy simulation (LES), direct numerical simulation (DNS), or Lattice Boltzmann methods (LBM), and so forth, helped reveal ample details of local conditions in the complicated subchannel system.

It is with great anticipation that the advancement of CFD modeling might facilitate further understanding of various thermal-hydraulic phenomena, such as excursion of flow instability and turbulent mixing, as well as various mechanisms leading to the limiting conditions of critical heat flux (CHF). However, the progress in modeling efforts have continued facing monumental challenges in single and multiphase experiments involving interphase tracking, non-intrusive measurement in highly obstructed narrow channels and flow visualization concerning wide ranges of thermal-hydraulic conditions (from low pressure, low temperature to high pressure, high temperature), as well as validation, verification, and uncertainty qualification of rod bundle experimental data for CFD benchmarking. This special issue invited investigators to contribute original research articles as well as review papers across the following topics: (1) recent development in fuel design tools, CFD modeling, benchmarking, and verification techniques; (2) VV/UQ and rod bundle CHF experiments and verifications; (3) mechanistic modeling and empirical DNB correlations for BWR and PWR fuel; (4) effect of parameters on CHF; (5) reactor core protection against DNB; (6) fuel reliability and inspection.

Six papers were selected for this special issue. The paper by B. Yang et al. titled “*Uniform versus nonuniform axial power distribution in rod bundle CHF experiments*” presents potential limitations of using uniform rod bundle CHF data for CHF correlation development of light water reactors with nonuniform axial power distribution (APD). The paper “*Effect of flow blockage on the coolability during reflood in*

*a 2 × 2 rod bundle*” by K. Kim et al. reveals the experimental study on the thermal behavior and effect of the ballooned region on the coolability using a 2 × 2 rod bundle test facility during the reflood phase of a large-break-loss-of-coolant accident (LBLOCA) in a pressurized-water reactor (PWR). The paper of J. Shan et al. titled “*Subchannel analysis of wire wrapped SCWR assembly*” provides subchannel analysis and experimental investigation of a wire-wrapped SCWR assembly. In the paper “*Direct numerical simulation and visualization of subcooled pool boiling*,” by T. Kunugi and Y. Ose, perform direct numerical simulation of the subcooled pool boiling phenomena in order to clarify the heat transfer characteristics and discuss the mechanism in their paper. The influence of outer strap design on fuel assembly thermal hydraulic performance is studied using a commercial computational fluid dynamics (CFD) code, ANSYS CFX, and a subchannel analysis code, FLICA, in the paper entitled “*Influence of spacer grid outer strap on fuel assembly thermal hydraulic performance*” by J. Yan et al. Finally, the paper of C. Peña-Monferrer et al. titled “*CFD turbulence study of PWR spacer-grids in a rod bundle*” analyzes the turbulence effects of different types (a split-type and a swirl-type) of spacer-grid geometries on single-phase turbulent mixing in a PWR (pressurized water reactor) rod bundle.

## **Acknowledgment**

The editors of this special issue express their sincere gratitude to all authors of all the remitted papers (selected or not) for their contribution.

*Baowen Yang  
Yassin A. Hassan  
Jianqiang Shan  
Bin Zhang  
Junli Gou  
Liangzhi Cao*

## Research Article

# CFD Turbulence Study of PWR Spacer-Grids in a Rod Bundle

C. Peña-Monferrer,<sup>1</sup> J. L. Muñoz-Cobo,<sup>1</sup> and S. Chiva<sup>2</sup>

<sup>1</sup> Institute for Energy Engineering, Universitat Politècnica de València, Camino de Vera, s/n, 46022 Valencia, Spain

<sup>2</sup> Department of Mechanical Engineering and Construction, Universitat Jaume I, Avenida Sos Baynat, s/n, 12071 Castellón de la Plana, Spain

Correspondence should be addressed to S. Chiva; [schiva@emc.uji.es](mailto:schiva@emc.uji.es)

Received 7 October 2013; Accepted 13 February 2014; Published 30 June 2014

Academic Editor: Bao-Wen Yang

Copyright © 2014 C. Peña-Monferrer et al. This is an open access article distributed under the Creative Commons Attribution License, which permits unrestricted use, distribution, and reproduction in any medium, provided the original work is properly cited.

Nuclear fuel bundles include spacers essentially for mechanical stability and to influence the flow dynamics and heat transfer phenomena along the fuel rods. This work presents the analysis of the turbulence effects of a split-type and swirl-type spacer-grid geometries on single phase in a PWR (pressurized water reactor) rod bundle. Various computational fluid dynamics (CFD) calculations have been performed and the results validated with the experiments of the OECD/NEA-KAERI rod bundle CFD blind benchmark exercise on turbulent mixing in a rod bundle with spacers at the MATIS-H facility. Simulation of turbulent phenomena downstream of the spacer-grid presents high complexity issues; a wide range of length scales are present in the domain increasing the difficulty of defining in detail the transient nature of turbulent flow with ordinary turbulence models. This paper contains a complete description of the procedure to obtain a validated CFD model for the simulation of the spacer-grids. Calculations were performed with the commercial code ANSYS CFX using large eddy simulation (LES) turbulence model and the CFD modeling procedure validated by comparison with measurements to determine their suitability in the prediction of the turbulence phenomena.

## 1. Introduction

A PWR requires a design with enough safety margins regarding the critical heat flux (CHF). The value of the CHF is largely altered by the presence of the spacer-grids geometry in the fuel assemblies and is predicted generally by means of empirical departure from nucleate boiling (DNB) correlations.

In the last years, the influence of flow obstacles on the CHF has been studied. Pioro et al. [1] confirm, with various types of flow obstacles, the strong influence on CHF of the distance from an upstream flow obstacle and how the CHF enhancement decays exponentially with the distance from the flow obstacle. Furthermore, several studies that include experimental research [2–4] and computational simulations [5–9] have been conducted in order to study the effect of the spacer-grid on the coolant.

In recent years, the use of CFD numerical tools in nuclear engineering area has grown rapidly and some codes based in those numerical techniques are well-established, and state-of-the-art of them is employed in the nuclear engineering

area. CFD tools are widely used to provide supplementary information relevant to safety margin, and especially their use is becoming widespread in modeling situations showing a strong multidimensional and turbulent flow behavior. However, it is not very mature in some specific areas, and hence the possibility of validating the complex physical phenomena happening in nuclear structures as spacer-grids is highly appreciated as these results could be of great value for future studies of spacer-grid including heat transfer from the rods and as a basis of spacer-grid simplifications.

Turbulent flow structures in the subchannels of a rod bundle are largely influenced by the design of the spacer-grids and modifying the heat transfer from heat structure to the coolant in operational transients or accidents scenarios. Local characteristics of the turbulent flow in subchannels of a rod bundle are sensitive to numerical and physical models used in CFD analysis of which the tools should be widely validated using a proper set of experimental data.

The simulation of the spacer-grid requires advanced turbulent model. Since a long time ago, many contributions have been focused on the use of LES technique showing

its capability reproducing the important features of wall-bounded turbulent flows. Since 1963, the Smagorinsky [10] formulation for resolving the subgrid scales has been used and the near-wall predictions have improved [11–15]. Thence, further progress and the availability of faster computers have permitted the use of LES turbulence models in industrial applications as can be shown in several detailed reviews over this year [16–20].

The second international benchmark exercise on the turbulent mixing in a rod bundle is the OECD/NEA-KAERI rod bundle CFD benchmark exercise based on the MATiS-H (Measurement and Analysis of Turbulent Mixing in Subchannels—Horizontal) experiments [21]. These experiments provide data to reveal fundamental characteristics of the turbulent mixing in subchannels and confirm the use of the CFD codes as a tool for later use in modeling spacer-grids characteristics, like pressure drop, quantifying the CHF margin reliably for normal operation condition, and operational transients, and also allowing eventually the use of CFD codes for predicting the DNB under accidental conditions.

The following sections contain an exhaustive description of how the case is configured to obtain an even balance between maintaining a low computational demands and fulfilling the requirements according to the NEA Best Practice Guidelines (BPG) [22] of the CFD simulation. A description of the experimental facility and the conducted experiments are described in Section 2 Benchmark Test Description; the results obtained in those experiments will be used for the validation of the CFD models. A comprehensive description of the model is described in Section 3 CFD Simulation Setup; it accounts for the whole modeling process used to obtain results to validate with the experiments. These models are simulated using a LES turbulence model within reach of a regular workstation without significant loss of accuracy in the predicted results. Results for spacer-grids with split and swirl mixing vanes were presented in the blind benchmark, and results of velocity, RMS velocity, and vorticity at different streamwise and spanwise locations downstream of the vanes of the spacer-grid are used for the validation of the model in Section 4 Results and Discussion as well as an analysis of the resulting flow characteristics in the rod bundle. Finally, Section 5 Conclusions summarizes the conclusions and remarks of the work presented in this paper.

## 2. Benchmark Test Description

The MATiS-H, located at the Korea Atomic Energy Research Institute (KAERI), Daejeon, Korea, is illustrated in Figure 1. The test rig consists of a channel of 170 mm side length and 4.670 mm long and a  $5 \times 5$  rod bundle of 25.4 mm of rod diameter and 3.863 mm long operating at  $Re \sim 50000$ . The hydraulic diameter of the channel,  $D_H$ , is 24.27 mm. The spacer-grid with mixing vanes, 2.6 times larger than the size of PWR fuel bundles, is located inside the channel for generating lateral turbulent mixing in subchannels.

The movable flow straightener allows expected identical inlet flow conditions upstream of the spacer. The distance

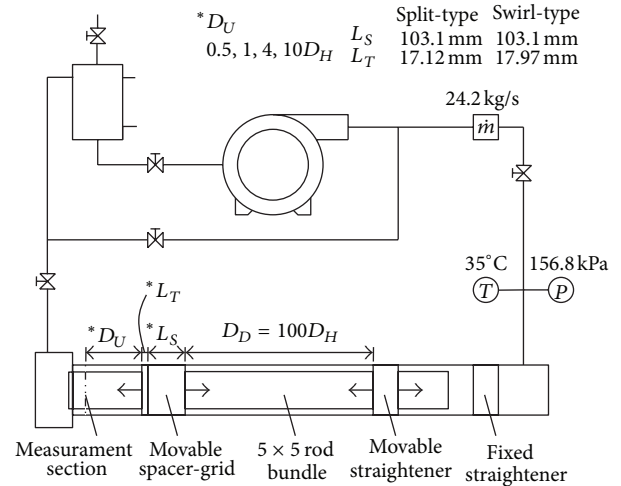


FIGURE 1: Schematic diagram of the MATiS-H test facility and location of measurements.

$D_D$  is set at  $100 D_H$  to have a fully developed flow profile at the inlet to the spacer-grid. A measurement section is fixed at a position 10 mm upstream of the end of the rod bundle. The spacer-grid, of dimension  $L_S$ , can be moved axially to increase the downstream distance of the measurement section to determine the distance upstream of the spacer-grid ( $D_U$  in Figure 1). Different experiments are carried out varying  $D_U$  from 0.5 to  $10 D_H$  to cover the decay of the turbulence produced by the spacer-grid.

The experiments have been performed for two different types of mixing vanes: split-type (Figure 2(b)) and swirl-type (Figure 2(a)). In both cases, axial and lateral velocities were measured with Laser Doppler Anemometry (LDA) probes for  $U$ ,  $V$ , and  $W$  measurements. Turbulent intensities and vorticity in subchannels were then evaluated from the velocity measurements.

## 3. CFD Simulation Setup

In this section, the simulation setup developed for investigating spacer-grid effects in MATiS-H is presented. An extensive description of geometry modeling, meshing, and CFD setup of the physical models will be provided.

**3.1. Computational Domains.** The main purpose of the simulation is to obtain results downstream of the spacer-grid. The model was classified in different domains for better adapting to the experimental scenario. The proposed decomposition of the test model is outlined in Figure 3.

- (i) Domain B (half domain is represented as explained later in Section 3.3.2) is the most important domain as it contains the spacer-grid. This is, in turn, split into two subdomains jointly simulated by fluid-fluid interface boundary condition. The first region of  $9 D_H$  contains fully developed flow and one can design mesh sizes bigger as consequence of the low velocity gradients.

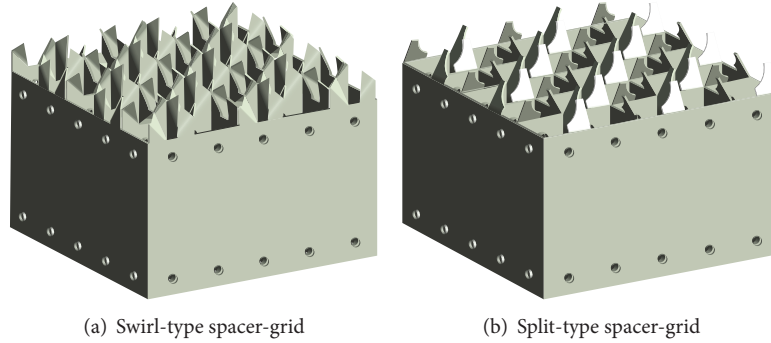


FIGURE 2: Types of spacer-grids tested in MATiS-H.

- (ii) Domain A is used to compute suitable inlet profiles for Domain B as the known value at the inlet of the test rig is the mass flow rate. It is a bare rod bundle of  $90 D_H$  and starts from the movable flow straightener upstream of the spacer-grid (see Figure 1).
- (iii) Domain C was modeled in order to determine the influence of the proximity of the measurement section (10 mm). The simulation results corroborate the low influence of the immediate vicinity of this domain on the measurement section. As a result, Domain C was not considered in the final CFD simulations with spacer-grids. Domain C does not have such influence, and all the measurements to validate the model can be done with only one simulation per spacer-grid of  $10 D_H$  downstream of the spacer-grid.

**3.2. Boundary Conditions.** Assuming the decomposition mentioned in the previous section, Figure 4 shows a schematic representation of the boundary conditions for the CFD simulations.

The inlet boundary condition for Domain B is established with the velocity, turbulence kinetic energy, and turbulence energy dissipation data obtained at the end of Domain A. The uniformity of the flow at the inlet of Domain A must be guaranteed by the movable flow straightener (Figure 1).

The assumed fully developed flow at the inlet of Domain B was tested evaluating the turbulence decay in the streamwise direction in the  $90 D_H$  of the bare rod bundle and it was concluded that the values of kinetic turbulence energy are almost stabilized at the final of this domain.

The outlet boundary condition is always established as a constant pressure for both simulations. It has been tested that the pressure drop on the isothermal system does not influence the water properties, as density and viscosity. The  $\Delta P$  value would be neglected and the pressure value obtained located at the inlet of the test rig (Figure 1) is used as a constant pressure outlet boundary condition. To obtain the exact pressure value at the outlet, it requires the simulations of straighteners, rod bundle supports, flow breaker, and out end, but it is not the focus of the present paper.

The boundary condition at the wall is established as automatic near-wall treatment, which automatically switches

from wall functions to a low-Reynolds near-wall formulation as the mesh is refined [23].

**3.3. Geometry Modeling and Simplifications.** The experiment proposed in this benchmark has a relative huge test section considering the flow characteristics happening there. Consequently, a modeled simulation of the whole experiment becomes heavier and the efforts to reduce computational requirements are appreciated. Hence, a set of measures and simplifications have been performed to achieve a feasible simulation as described in this section.

**3.3.1. Grid Strap Simplification.** The specifications of the spacer-grid geometry model show a gap between walls and the end of chamfer strap. This narrow distance can lead to numerical errors; however, the reduction in the cross section cannot be neglected. For such cases, a geometrical simplification in the grid straps has been performed. Straight straps are considered, and full intersection between rods and external wall channel is accomplished as shown in Figure 5.

**3.3.2. Periodicity Pattern.** The channel itself, without spacer-grid influence, has both horizontal and vertical symmetry. However, the presence of spacer-grids produces a local variation of the flow depending on the vanes direction. It leads to an asymmetric flow downstream of the vanes that complicates the model simplification with symmetries and requires the meshing of the entire model. The spacer-grids used in the experiments of the benchmark have an asymmetric geometrical configuration of the vanes. Nevertheless, during the preliminary steps of the geometric modeling procedure, a repetitive pattern was detected. The configuration of the vanes produces the opposite effect in one half of the domain than in the other half. In Figure 6, it can be noticed the vanes directions for both types of spacer-grids. Figure 6 shows the bending direction of the vanes for the split-type spacer-grid marked with R (Right), L (Left), U (Up), and D (Down). Looking at the vanes colored in red and applying a rotation of  $180^\circ$  around the center of the channel, it can be appreciated that each vane has the opposite direction regarding the vane in the same new position (e.g., up-down and left-right). It means that things happening in one half of the domain can be considered without modeling the other part of the geometry.

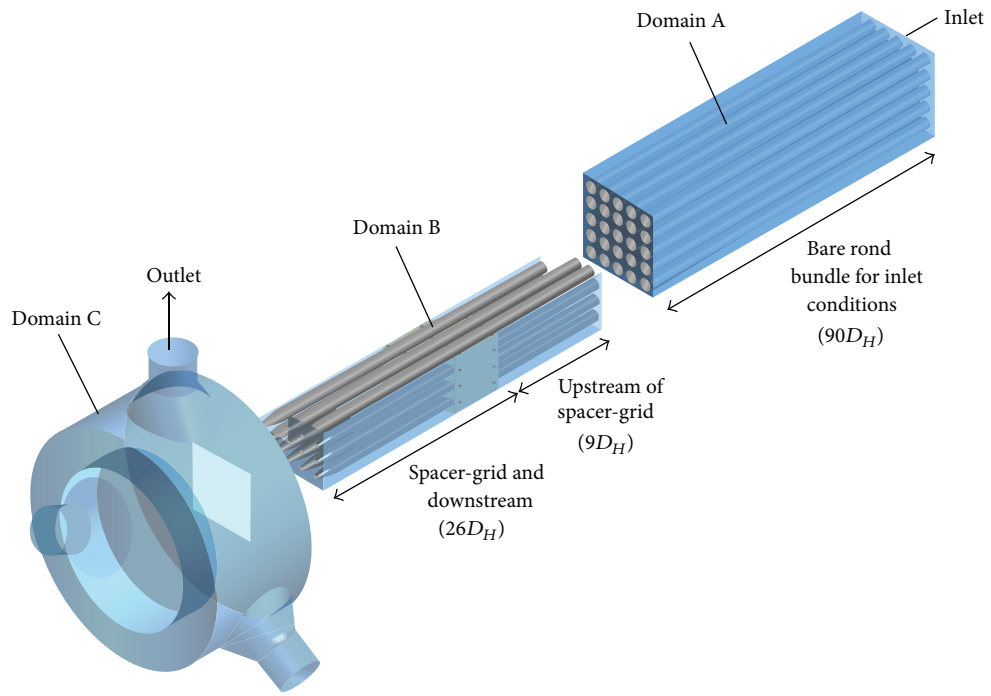


FIGURE 3: Domain decomposition of the test rig.

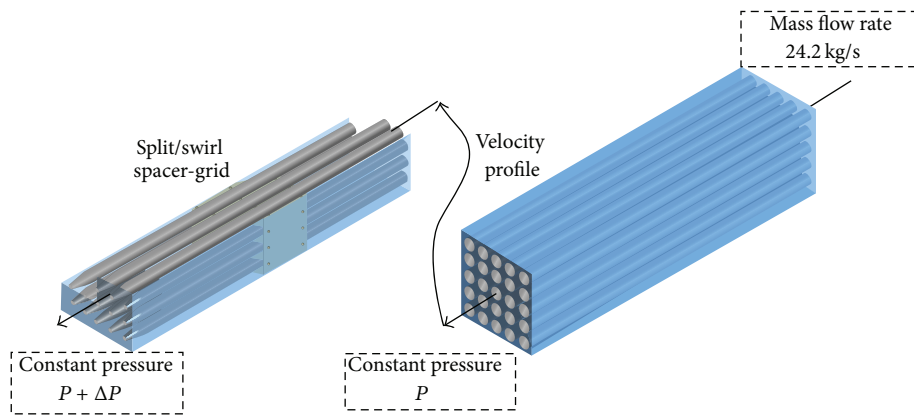


FIGURE 4: Inlet and outlet boundary conditions for the bare rod bundle and the model with the spacer-grid.

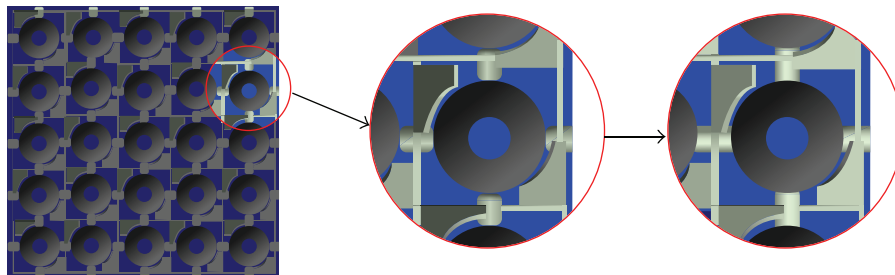


FIGURE 5: Geometrical simplified model of the grid strap.

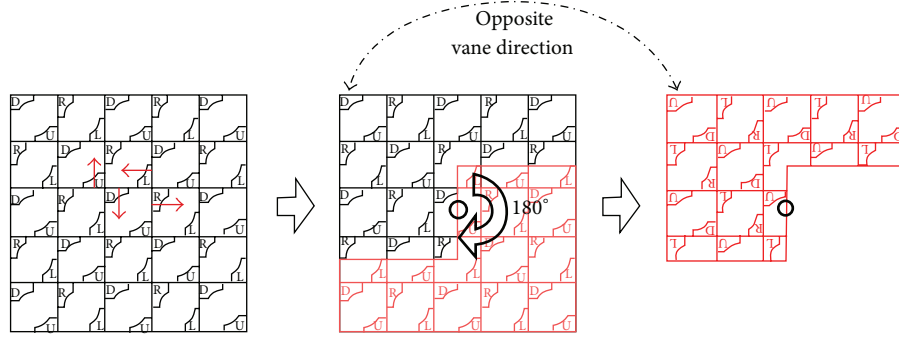


FIGURE 6: Geometrical simplified model of the grid strap.

TABLE 1: Mesh detail summary.

Spacer type	Cell elements [million]	$y^+$ range (average) [—]	Max. cell length streamwise/spanwise [m]
Swirl	25.98	0.09–2.63 (1.08)	$3 \cdot 10^{-4}/1.8 \cdot 10^{-3}$
Split	25.53	0.06–2.98 (1.13)	$3 \cdot 10^{-4}/1.8 \cdot 10^{-3}$

A periodic boundary condition has been applied to this model. This boundary condition is used when the physical geometry of interest and the expected pattern of the flow solution have a periodically repeating nature. The interface model defines the way the solver models the flow physics across the interface.

Only half of the domain can be modeled applying the required cut (from the center of the channel) in the geometry and implementing boundary interface using “rotational periodicity” [24]. The two sides of the periodic interface can be mapped by a single rotational transformation about an axis. The axis of the rotational transformation must be defined in the streamwise direction with the center in the middle of the channel. To test the correct performance of that simplification, the whole model without periodicity conditions and the new model with half domain with the rotational periodicity were simulated (Figure 7). The results show the velocity profiles for the case with periodicity boundary conditions matching those obtained with the entire model. Therefore, it will save half of the mesh nodes and much more in terms of computing time as the relation between the number of nodes and the run time does not increase linearly.

**3.4. Grid Generation.** The mesh was created using the ANSYS ICEM CFD 13.0 software and tested its quality in the aspect ratio, angles, skewness, and other quality criteria. The mesh type of Domain A is based on a block mesh as the absence of geometry irregularities allows higher quality mesh. However, Domain B containing the spacer-grid has irregularities that hinder obtaining a suitable mesh as possible.

Aware of the importance of meshing, one of the major parts of the effort devoted to the project has focused on obtaining a mesh as uniform as possible with an optimum size to cover the variations of fluid characteristics.

As demonstrated in [25] using a grid following the Taylor microscales, the spanwise mesh resolution and the cubicity of the cells are a crucial feature of the grid in channel flows. In that contribution, special attention has been taken in each subchannel having the consistent spanwise and streamwise mesh resolution, a uniform distribution, and a beneficial cell topology. Due to the different flow characteristics, the mesh subdomain upstream of the spacer-grid has an axial size twice of the spacer-grid and upstream regions. The cross section mesh distribution is the same in both cases.

In addition, since the complexity of the geometry, a large number of nodes should be considered. An agreement between the number of nodes (meeting the BPG), which affects the accuracy of the prediction, and the computational resources required has to be found.

Domain B mesh was generated with the following procedure:

- (1) scaling the geometry to reduce the cell size in the axial direction to obtain an exhaustive control of the cell axial size (the coefficient to scale varies for the upstream and spacer-grid areas);
- (2) generation of the volume mesh with the octree mesh method;
- (3) creation of the specified prism elements in successive layers away from the wall. A total of 10 layers with an exponential growth rate between them are applied; due to the narrow distance between some spacer-grid walls, the number of layers must be adapted to avoid bad quality of the elements and collisions between layers;
- (4) performing a “Tetra to Hexa” conversion with the ICEM tool “12 tetra to 1 hexa” to save cells and provide spatial uniformity;
- (5) resizing the mesh to its original axial size.

As a result of this procedure, two meshes were obtained with the characteristics shown in Table 1.

The result of this mesh procedure and its influence on the flow will be shown. Figure 8(a) establishes the intersection planes for the mesh analysis, and Figure 8(b) shows the mesh distribution in the cross plane.

Regarding the cross section mesh, an ordinary subchannel has been selected and the zoom detail in the near wall

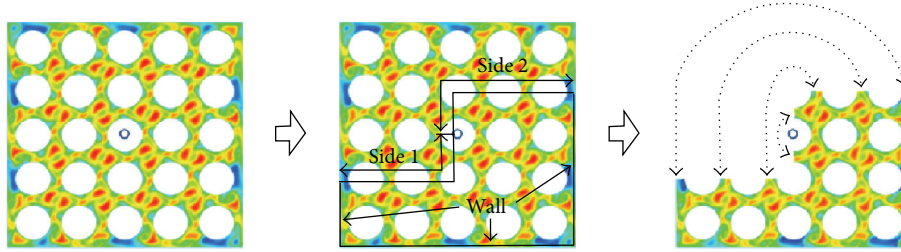


FIGURE 7: Rotational periodicity boundary condition.

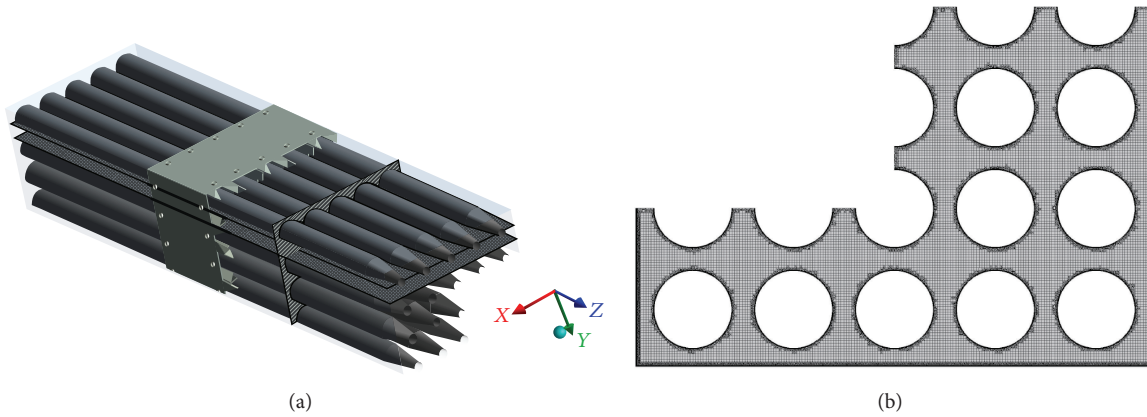


FIGURE 8: Planes selected across the model (a) and mesh distribution for the cross section plane (b).

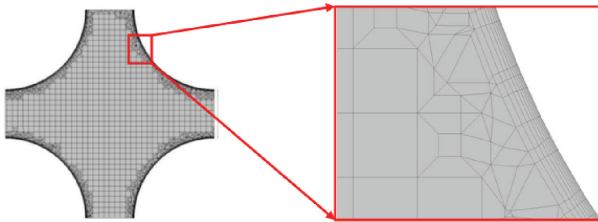


FIGURE 9: Subchannel mesh distribution with near-wall mesh detail.

presented (Figure 9). The wall detail shows the fine mesh near the wall and the complex transition between the layers and the core region. The height of the first prism layer is defined to reach the target  $y^+$  and a minimum number of prism layers are established. The height ratio (ratio in which the height of the next layer is specified with exponential law) is dynamically adapted in order to assort the geometry irregularities.

The mesh of the two longitudinal planes shown in Figure 10 is as follows: one intersects rods and the other intersects spacer-grid wall.

The mesh distribution near the wall must deal to reach the criteria of NEA BPGs in a good agreement between the  $y^+$  and the Courant number. The range of  $y^+$  for both spacer-grids is from 0.06 to 2.98 with average values of 1.13 for split-type and 1.08 for swirl-type. Figure 11 shows the local effects on the Courant number of the flow near the wall. Far away from the wall near 1 values are obtained.

The vane configuration has a direct influence in the meshing procedure, particularly, in the transversal and longitudinal mesh sizes. In the current simulation, the maximum cell size has been considered equivalent for both spacer-grid types. It is required to highlight the influence of the discretization in order to know the assumed error in benefit of the computational resources and know the possible weakness points of the used model. In case of the swirl vane, gradual changes of the flow occur, but for split vanes higher gradients are present. Consequently, for the same spatial discretization, the vane area shows more local numerical irregularities (Figure 12(b)) for the split-type rather than for the swirl-type (Figure 12(a)).

A detailed zoom of the mesh near the vanes for split and swirl spacer is shown in Figure 13.

**3.5. Turbulence Modeling.** The turbulence model selected for solving Domain A is the RANS shear stress transport (SST) model [23] because of the simplicity of the flow in this area. The same turbulence model has been used for the simulation to initialize values in Domain B for the LES simulation. The Smagorinsky subgrid-scale model [23] was used because of its solid mathematical and physical background instead of the WALE model, although theoretically it is more appropriate for wall bounded flows. To account for the near-wall effect, the turbulent viscosity is damped by means of a length minimum and viscosity damping functions.

**3.6. Advection Schemes and Convergence Control.** For the solver control parameters, a high-resolution advection

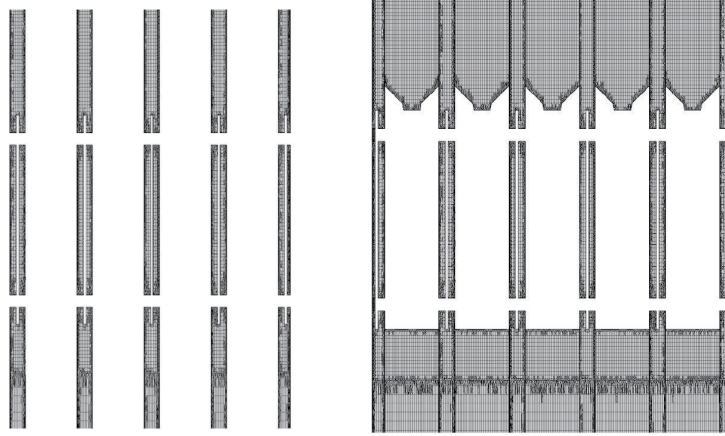


FIGURE 10: Subchannel mesh distribution with near-wall mesh detail.

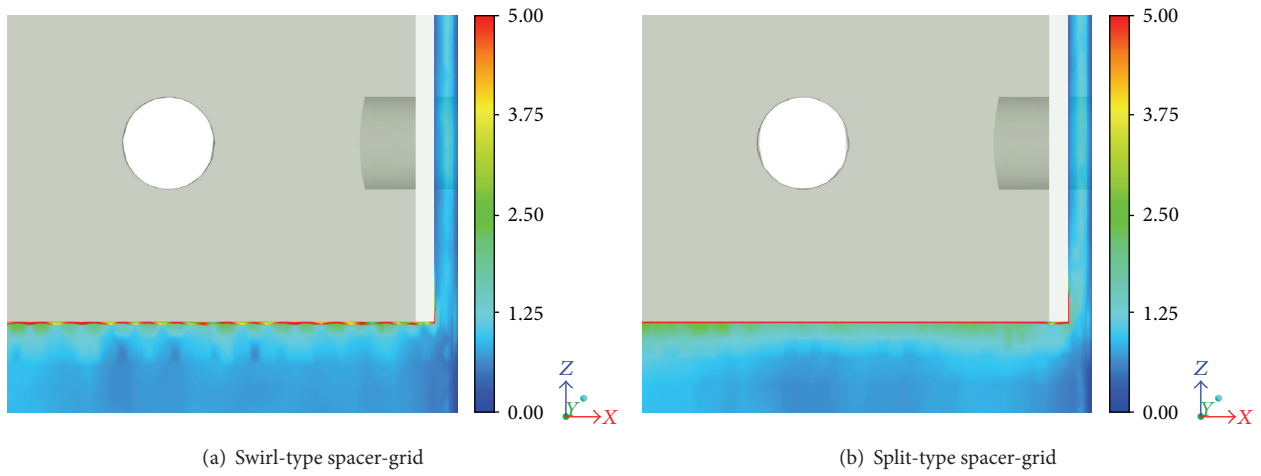


FIGURE 11: Local effects on the courant number.

scheme (2nd or higher order) has been chosen when using the SST turbulence model. For the LES simulation, we have used the central differencing scheme and second order backward Euler transient scheme. The target maximum number of coefficient loops per each time step has been selected to optimize the computational time. The selected value of 4 maximum number of coefficient loops showed optimal computational time without loss of precision. The convergence criteria for the RMS residual were set to a target value of  $1 \cdot 10^{-6}$  for both turbulence models.

For LES turbulence model, as an unsteady simulation, a total time must be provided and it is needed to specify enough time to provide a valid statistic. An optimal time has been determined based on temporal evolution of some monitored variables in a set of points. The statistical begins at a sufficient time that it is not influenced by the initial values. The summary of simulations for SST and LES turbulence models is shown in Table 2.

#### 4. Results and Discussion

The CFD results presented were run in a  $2 \times 6$ -core Intel Xeon E5645 at 2.40 GHz workstation using ANSYS CFX Academic

TABLE 2: Convergence criteria and advection scheme.

Turbulence model	Advection scheme	Time step [s]	Physical time [s]
SST	2nd or higher order	$4.6 \cdot 10^{-2}$	Steady state
LES	Central difference	$7 \cdot 10^{-4}$	1.25

Research, Release 13.0. For Domain B simulation, Table 3 shows a summary of times and related information for each spacer-grid type. A fixed time step was selected to permit a resulting RMS Courant number near 1. A total time large enough to obtain statistics steadiness have been determined.

The next sections will show a set of results to study the flow pattern modifications due to its pass through the spacer-grid elements. The validation of the CFD model through comparison with the experimental data is performed at strategic locations in the domain considering both mean and profile values (Section 4.1). As additional information, some figures are obtained from the CFD results in order to see the flow behavior produced by the spacer-grids as a

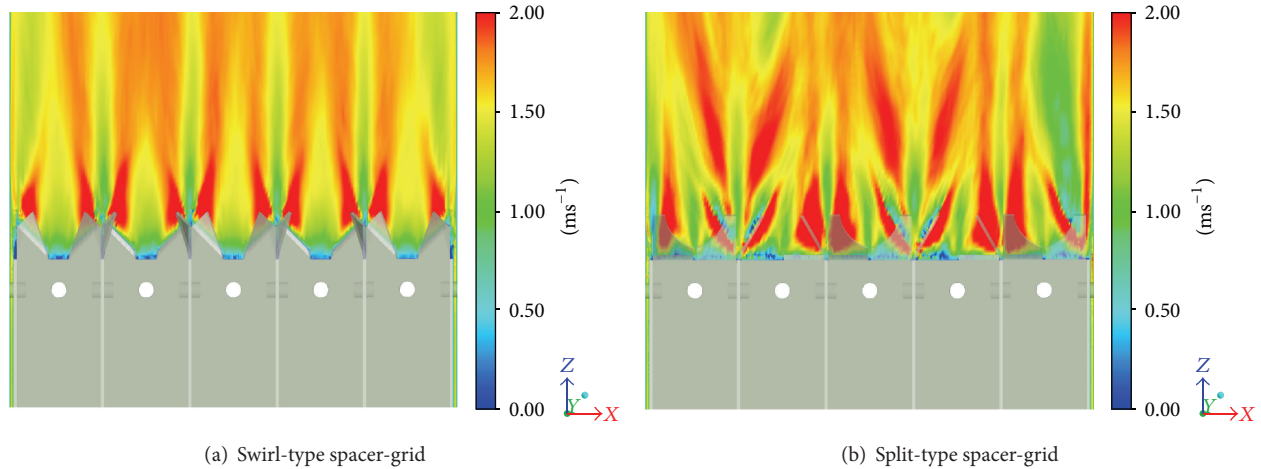


FIGURE 12: Local effects on the streamwise velocity.

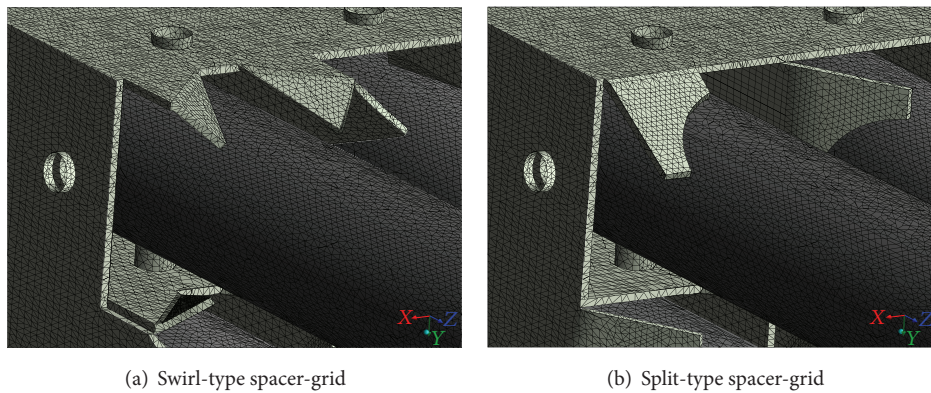


FIGURE 13: Mesh vane detail.

graphic illustration of the evolution of the turbulent flow (Section 4.2).

**4.1. Comparison between CFD Simulation and Experimental Results: Model Validation.** The following pages show the comparison between experimental data and the CFD results. The comparison includes profiles for time-averaged velocity and time-averaged RMS values of the fluctuating components for all three velocity components at two different distances from the wall of  $y_{wall} = 3.71$  mm and  $y_{core} = 68.44$  mm. In order to observe the decay of the turbulence, three different axial positions  $1 D_H$ ,  $4 D_H$ , and  $10 D_H$  from the origin of the system of coordinates as marked in Figure 14 are analyzed. Furthermore, an ordinary subchannel has been chosen in order to analyze the local effects as the circulation and vorticity in the individual subchannel.

Generally, the split spacer-grid produces more turbulence than the swirl-type spacer-grid and its effects go to  $10 D_H$  downstream. This situation differs depending on the distance from the wall being in the center of the channel more influenced by the neighboring vanes.

The comparison of the CFD results with the measured data at the two different distances from the wall for mean and

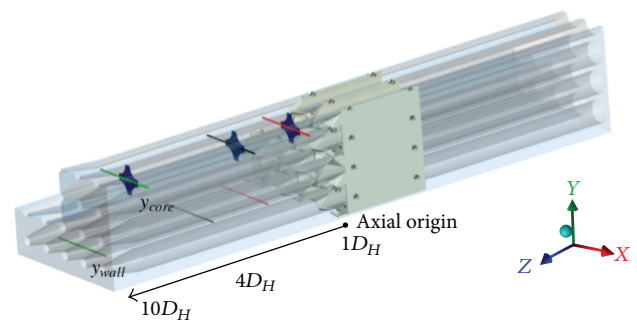


FIGURE 14: Subchannel and measurement lines at different axial positions from the specified origin coordinate system.

RMS velocity values in the three axial positions for the three components  $u$ ,  $v$ , and  $w$  is shown in Figures 15 and 16 for both swirl-type and split-type spacer-grid spacers. The horizontal axis represents the position from the center of the channel to the wall and is normalized with the rod-to-rod pitch distance ( $P = 33.12$  mm). Mean and RMS velocities in the vertical axis are normalized with the streamwise bulk velocity ( $W_{bulk} = 1.5$  m/s). Sets of charts in Figures 15 and 16 show experimental

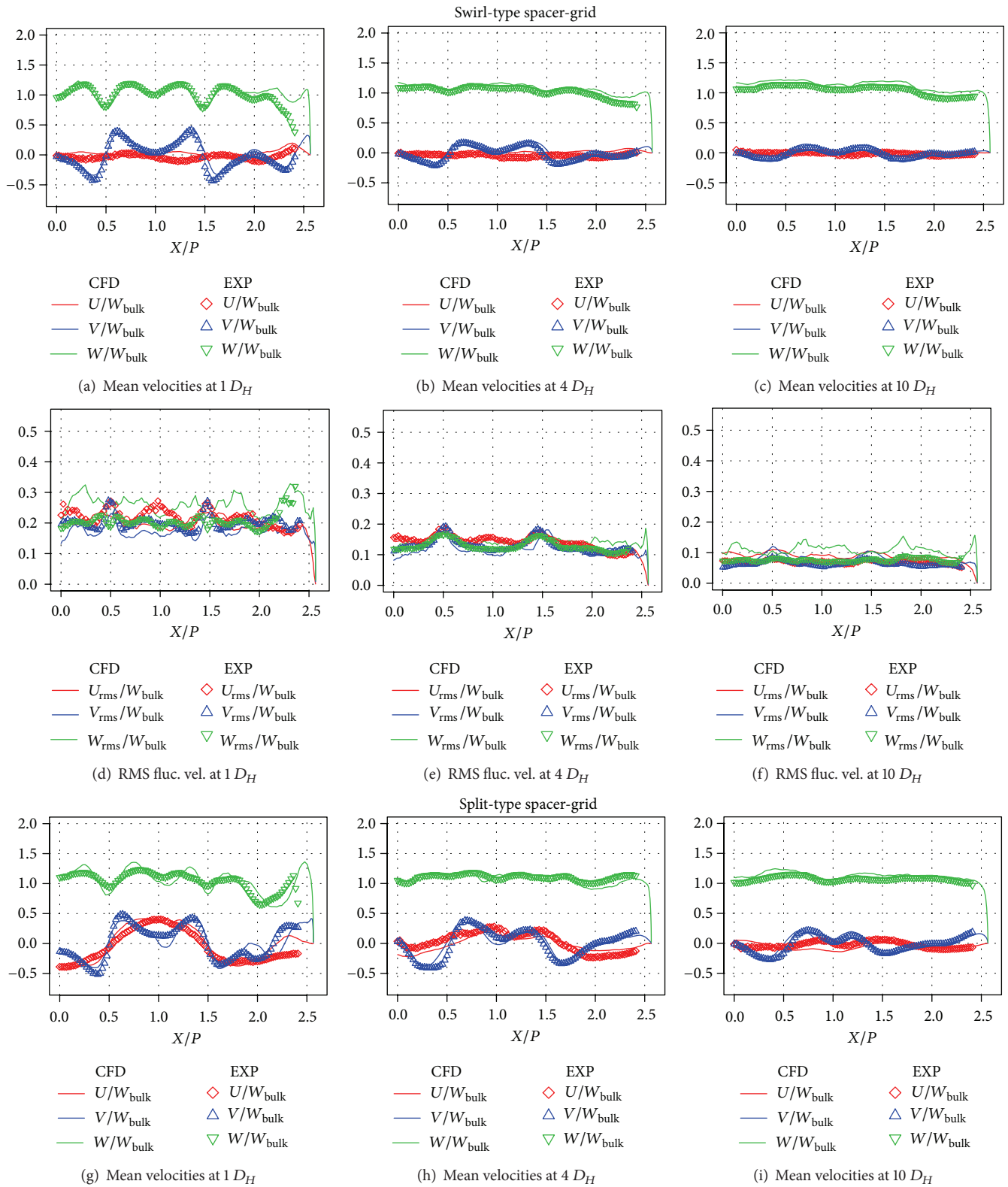


FIGURE 15: Continued.

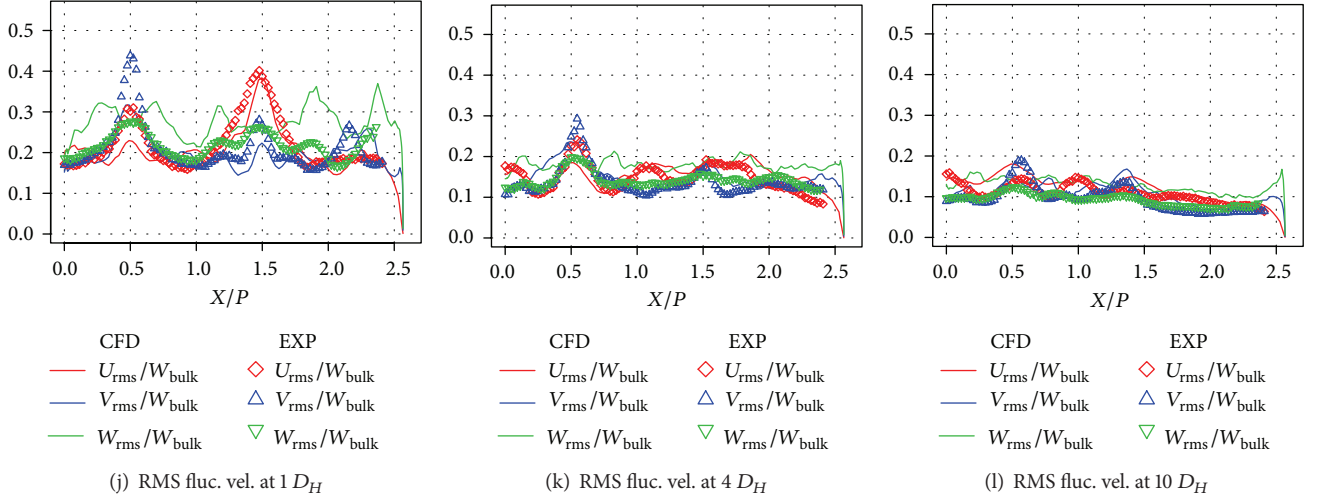


FIGURE 15: Mean and RMS velocity components at  $y_{core}$  elevation for split spacer-grid type. The horizontal axis represents normalized distance from the center of the channel to the wall, while the vertical represents normalized velocities or RMS fluctuations.

TABLE 3: Summary of the CFD simulations.

Type	Total time [hrs]	Number of cores	RMS Courant	Statistic initial time [s]	Physical averaging time [s]
Split	367	12	1.30	0.28	1.25
Swirl	345	12	1.12	0.28	1.25

data represented as dots, while the results obtained by means of CFD simulation are represented as lines. The color red is used for  $u$  component, blue for  $v$ , and green for  $w$ .

The results obtained in the simulations show a good capability to capture the turbulence phenomena and the procedure of production of turbulence and dissipation. Velocity profiles for all the components as those shown in Figures 15(a) to 15(c) and 16(a) to 16(c) clearly show a good agreement for peaks and valleys, while in Figures 15(g) to 15(i) and 16(g) to 16(i) small differences are presented; nevertheless, the trend remains fitted to the experimental data. It is attributed to a need of a local grid refinement in the mesh for the split spacer-grid where high velocity gradients appear. The assumption of a small error was accepted in benefit of the computational resources required as well as the influence on the time step in order to keep the Courant number under the required value. These mentioned figures also show how the turbulence model used is capturing with the same agreement the velocity profiles near the wall and far away from the wall. The dissipation turbulence downstream of the spacer-grid is noticed from distance  $1 D_H$  to  $4$  and  $10 D_H$  where the profiles are almost flattened.

RMS fluctuating velocities show general overpredicted values especially near the focus of turbulence (Figures 15(d), 15(j), 16(d), and 16(j)). The prediction improves as the fluctuation decreases downstream of the spacer-grid (Figures 15(e), 15(f), 15(k), and 15(l)). The turning points determining the relative maximum and minimum values seem to fit the experimental data. As mentioned before, the grid size plays an important role, but there is a big influence of the subgrid-scale model and the wall damping functions

requiring further investigation. More experimental results are required to validate the turbulence behavior between the rods in a subchannel.

Values of circulation expressed as  $\oint \omega_z dx dy$ , where  $\omega_z$  is the streamwise component of vorticity, are compared with experimental data for the designated subchannel (see Figure 17). As expected, the subchannel circulation for the split-type spacer-grid is around twice bigger than the swirl-type spacer-grid. Simulation results have the same trend in the split-type, but the swirl-type has a discrepancy at  $1 D_H$ .

**4.2. Study of the Flow Structure Produced by the Spacer-Grids.** Once the model has been validated, some information about the flow behavior produced by the spacer-grids will be studied. Following figures extracted from the CFD results are illustrated with reflection applied in the postprocessing stage for a better visualization.

Figure 18 shows the effect of split and swirl spacer-grids on the flow. Streamlines representing the flow leaving the spacer around only one rod are illustrated. It is appreciated as for the split-type Figure 18(b) the flow influences directly the other subchannels, while for swirl-type Figure 18(a) the effect remains in the same subchannel.

In Figure 19, the turbulence dissipation process in three different measuring planes is appreciated. Values of time-averaged velocity, time-averaged RMS values of the fluctuating velocity in the streamwise component are presented.

In Figure 19, it is highlighted that regardless of the type of spacer-grid, the flow distribution at  $10 D_H$  is quite similar, but the swirl has a more symmetric distribution of velocity and RMS fluctuation values since  $4 D_H$  downstream from the spacer-grid. The split-type shows some undesired minimum

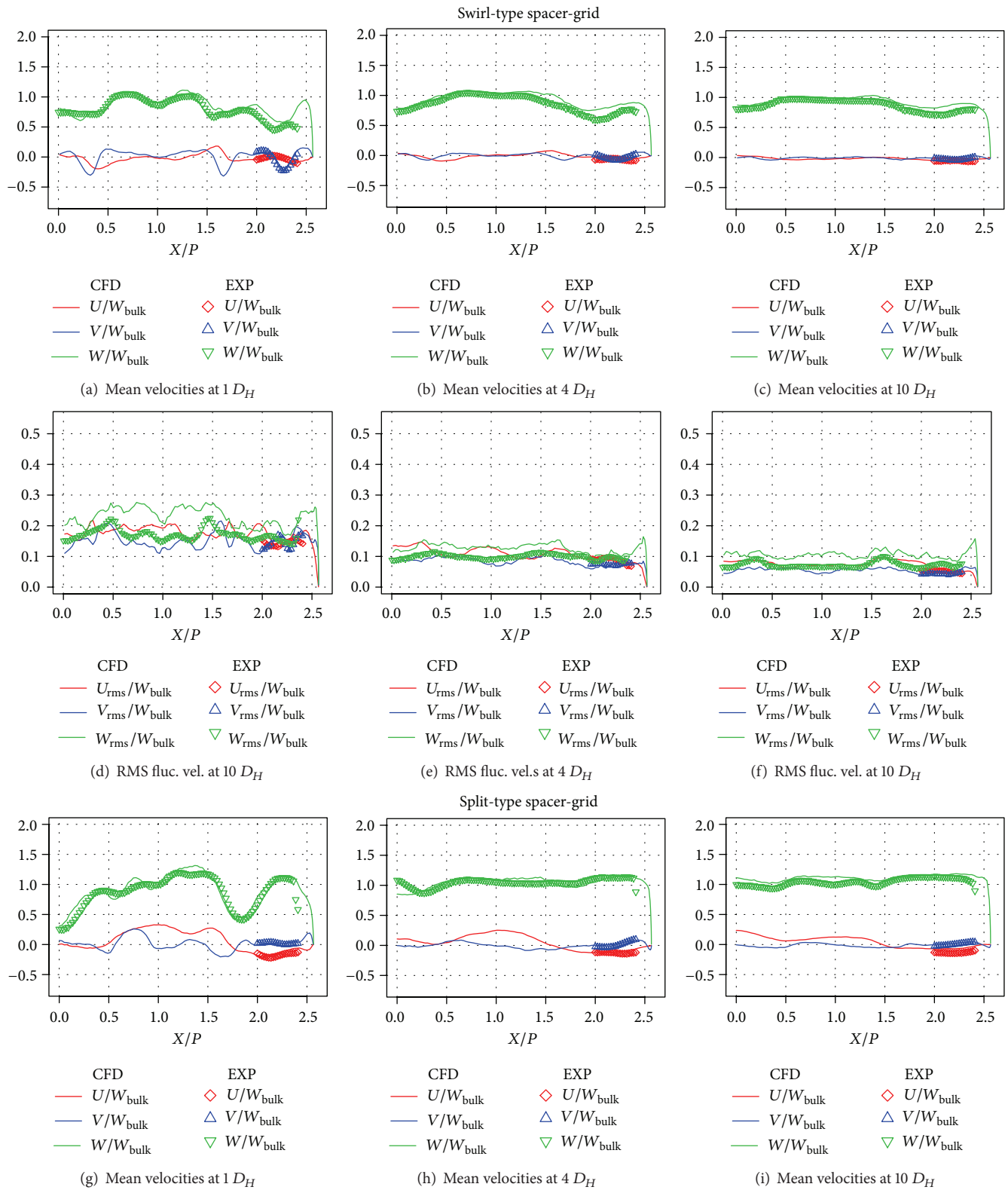


FIGURE 16: Continued.

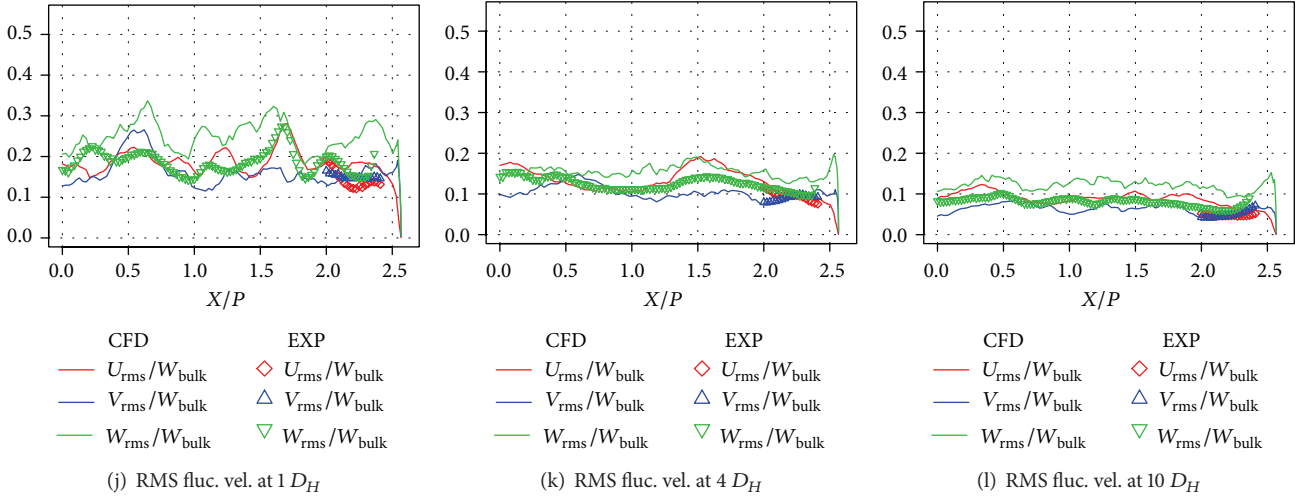


FIGURE 16: Mean and RMS velocity components at  $y_{wall}$  elevation for split spacer-grid type. The horizontal axis represents normalized distance from the center of the channel to the wall, while the vertical represents normalized velocities or RMS fluctuations.

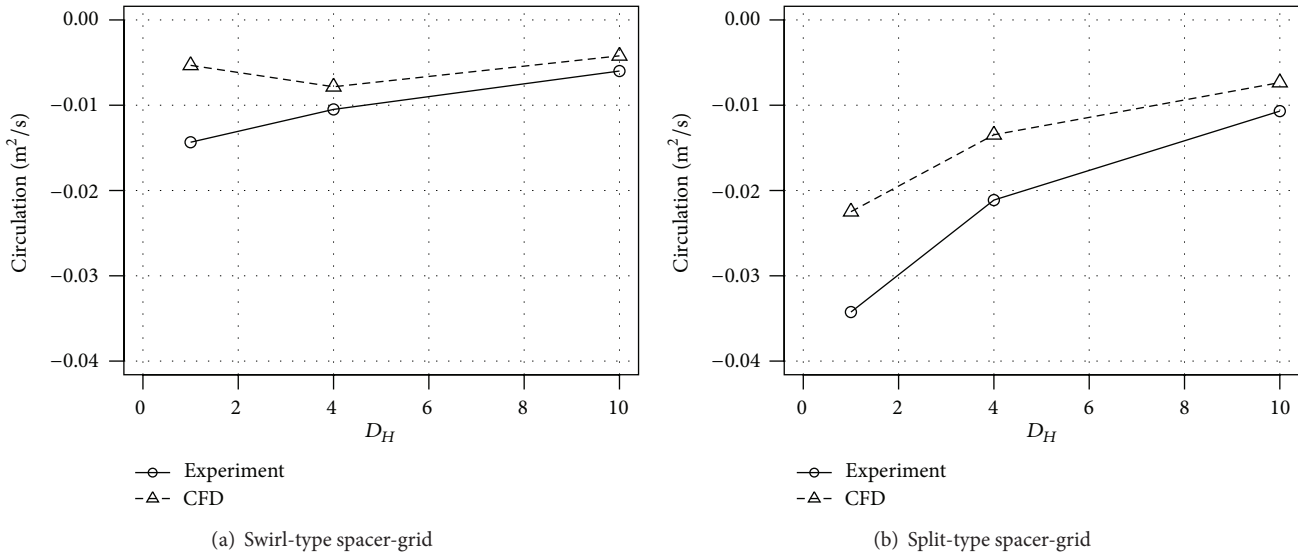


FIGURE 17: Evolution of the circulation along the streamwise direction.

peaks at the corners. For the mean velocities, it can be observed that the split type influences the flow far after the vanes. At  $10 D_H$ , the presence of high gradients at two opposite corners can be noticed, while the swirl maintains almost uniformity from  $4 D_H$ . The RMS are quite stable in both cases and seem more similar. In case of the axial vorticity evolution, there are higher values in the subchannels of the split-type in comparison with the swirl-type.

In order to illustrate the local effect that the spacer-grids have in each subchannel, the evolution of the mean streamwise vorticity along the downstream of the spacer is shown in Figure 20 for the designated subchannel (see Figure 14). The turbulence produced by the vanes of the split-type spacer-grid affects fairly the near-wall region, and it could have a positive effect on the local heat extraction from the wall. In case of the swirl-type, the vorticity gradient

is more uniform increasing the capability for homogenized temperature distribution in the core of the subchannel.

### 5. Conclusions

A CFD model for a rod bundle with a spacer-grid has been performed. The design procedure of modeling, meshing, physical model applied, and considered assumptions to model the related experiment has been described in the previous chapter, and the results and discussion were presented for two types of spacer-grid, split, and swirl mixing vanes.

It has been demonstrated that the described procedure to simulate PWR spacer-grids in rod bundles is valid to obtain realistic fluid mechanic predictions. The LES turbulence model implemented on a general purpose commercial code

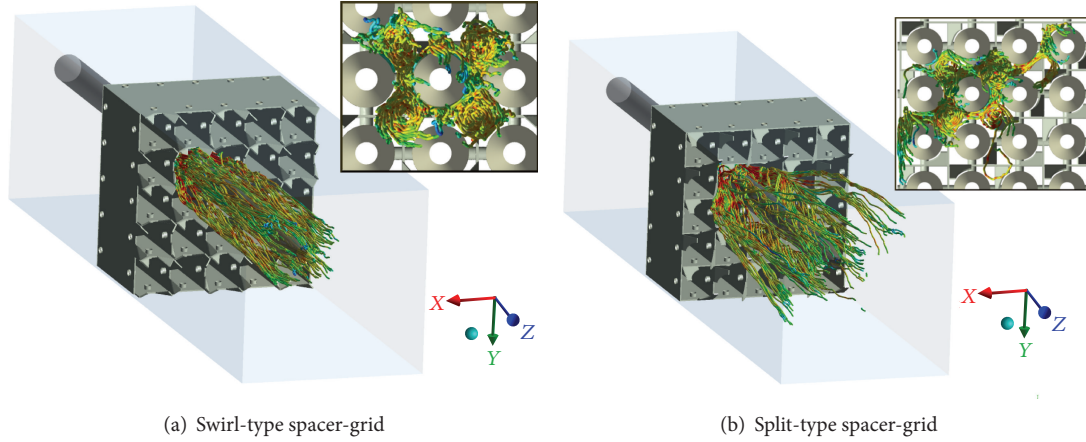


FIGURE 18: Streamlines of flow leaving the spacer around one rod for split spacer-grid. The streamlines represent the velocity in a chosen time step in a range from 0 to 2.3 m/s of a red-to-blue color scale.

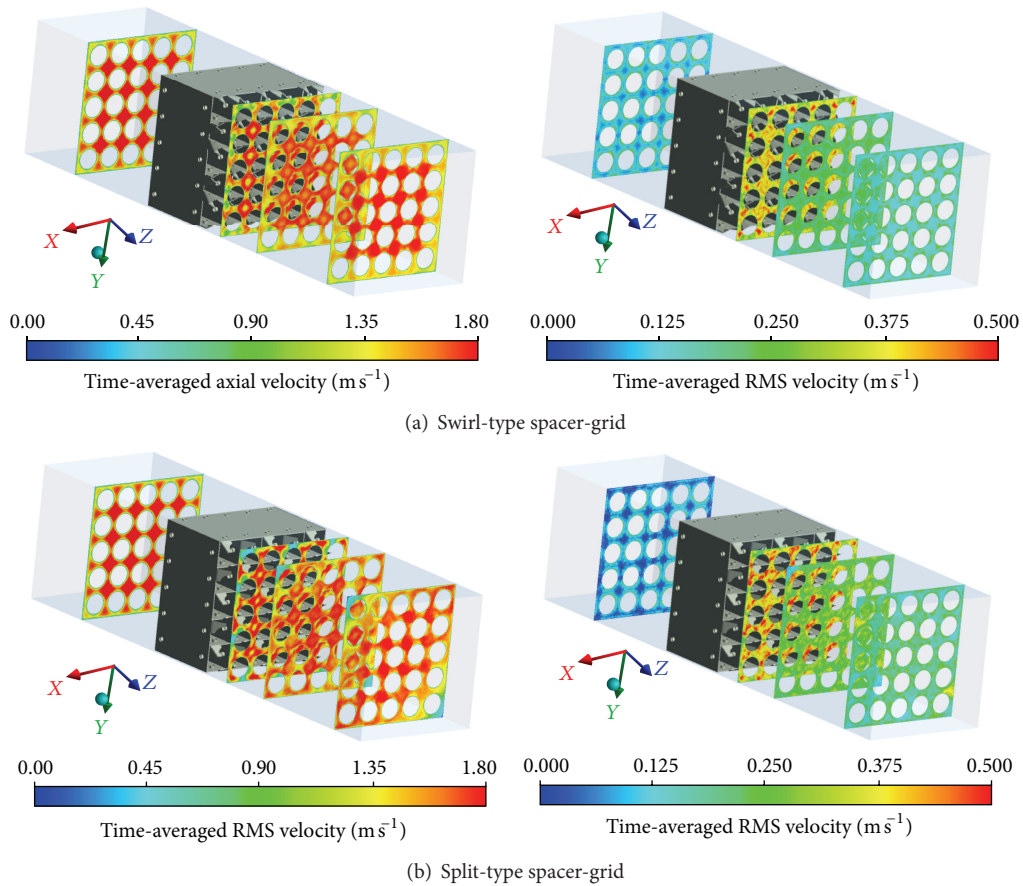


FIGURE 19: Time-averaged velocity, RMS fluctuating velocity at  $1 D_H$ ,  $4 D_H$ , and  $10 D_H$  downstream of the spacer-grid.

as the one used in this paper was satisfactory predicting the turbulent results. The simplifications added in the modeling stage reduce the simulation time substantially and allow a LES simulation with the performance of a regular workstation.

The turbulence production and dissipation evolution obtained in the simulation fit well the experimental data.

Velocity and RMS fluctuating evolve with a similar trend as the experimental data for two distinct spacer-grids. The circulation data in the subchannel adequately conforms the evolution along the flow direction verified with the experiments. Therefore, an analysis focusing on the mixing temperature can be done as the turbulence phenomena are being modeled properly.

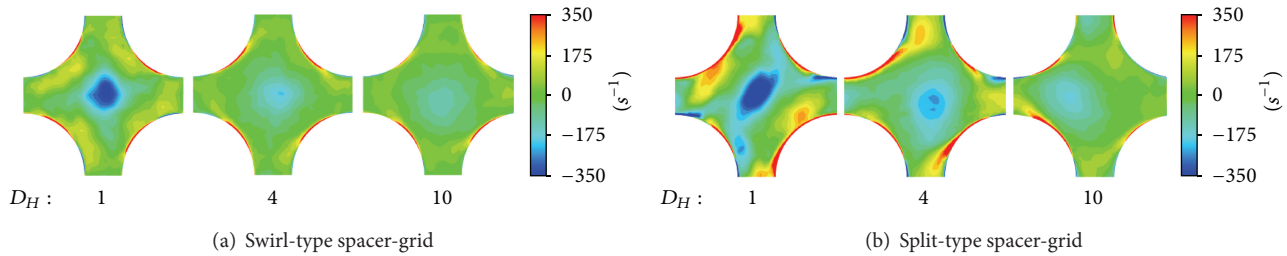


FIGURE 20: Vorticity contours at  $1 D_H$ ,  $4 D_H$ , and  $10 D_H$  downstream of the spacer-grid.

Further work should focus on the influence of the turbulence enhancement due to spacer-grids in the temperature profiles in the subchannels and the resulting CHF. Furthermore, the validated CFD model will be useful as a basis to create correlations to consider the spacer-grid turbulence generation without its detailed model to use in subchannel codes.

### Conflict of Interests

The authors declare that there is no conflict of interests regarding the publication of this paper.

### Acknowledgments

The authors sincerely thank the Consejo de Seguridad Nuclear (CSN) (Spanish Nuclear Safety Council) and the “Plan Nacional de I+D+i” Project EXPERTISER ENE2010-21368-C02-01 and ENE2010-21368-C02-02 for funding the project.

### References

- [1] I. L. Pioro, D. C. Groeneveld, S. S. Doerffer, Y. Guo, S. C. Cheng, and A. Vasić, “Effects of flow obstacles on the critical heat flux in a vertical tube cooled with upward flow of R-134a,” *International Journal of Heat and Mass Transfer*, vol. 45, no. 22, pp. 4417–4433, 2002.
- [2] S. K. Yang and M. K. Chung, “Turbulent flow through spacer grids in rod bundles,” *Journal of Fluids Engineering*, vol. 120, no. 4, pp. 786–791, 1998.
- [3] D. Caraghiaur, H. Anglart, and W. Frid, “Experimental investigation of turbulent flow through spacer grids in fuel rod bundles,” *Nuclear Engineering and Design*, vol. 239, no. 10, pp. 2013–2021, 2009.
- [4] Y. A. Hassan, M. E. Conner, and Z. Karoutas, “Experimental benchmark data for PWR rod bundle with spacer-grids,” *Nuclear Engineering and Design*, vol. 253, pp. 396–405, 2012.
- [5] H. Anglart, O. Nylund, N. Kurul, and M. Z. Podowski, “CFD prediction of flow and phase distribution in fuel assemblies with spacers,” *Nuclear Engineering and Design*, vol. 177, no. 1–3, pp. 215–228, 1997.
- [6] S.-H. Ahn and G.-D. Jeun, “Effect of spacer grids on CHF at PWR operating conditions,” *Journal of the Korean Nuclear Society*, vol. 33, pp. 283–297, 2001.
- [7] M. R. Nematollahi and M. Nazifi, “Enhancement of heat transfer in a typical pressurized water reactor by different mixing vanes on spacer grids,” *Energy Conversion and Management*, vol. 49, no. 7, pp. 1981–1988, 2008.
- [8] A. Pazirandeh, S. Ghaseminejad, and M. Ghaseminejad, “Effects of various spacer grid modeling on the neutronic parameters of the VVER-1000 reactor,” *Annals of Nuclear Energy*, vol. 38, no. 9, pp. 1978–1986, 2011.
- [9] S. Jayanti and K. Rajesh Reddy, “Effect of spacer grids on CHF in nuclear rod bundles,” *Nuclear Engineering and Design*, vol. 261, pp. 66–75, 2013.
- [10] J. Smagorinsky, “General circulation experiments with the primitive equations,” *Monthly Weather Review*, vol. 91, no. 3, pp. 99–164, 1963.
- [11] D. Lilly, “The representation of small-scale turbulence in numerical simulation experiments,” Tech. Rep., 1966.
- [12] M. Germano, U. Piomelli, P. Moin, and W. H. Cabot, “A dynamic subgrid-scale eddy viscosity model,” *Physics of Fluids A: Fluid Dynamics*, vol. 3, no. 7, pp. 1760–1765, 1991.
- [13] J. W. Deardorff, “A numerical study of three-dimensional turbulent channel flow at large reynolds numbers,” *Journal of Fluid Mechanics*, vol. 41, no. 2, pp. 453–480, 1970.
- [14] J. W. Deardorff, “The use of subgrid transport equations in a third dimensional model of atmospheric turbulence,” *Journal of Fluids Engineering*, vol. 95, no. 3, pp. 429–438, 1973.
- [15] P. Moin, *Large Eddy Simulation of Incompressible Turbulent Channel Flow*, Department of Mechanical Engineering, Stanford University, Stanford, Calif, USA, 1978.
- [16] B. Galperin and S. Orszag, *Large Eddy Simulation of Complex Engineering and Geophysical Flows*, Cambridge University Press, Cambridge, UK, 1993.
- [17] M. Ciofalo, “Large-Eddy simulation: a critical survey of models and applications,” in *Advances in Heat Transfer*, vol. 25, pp. 321–419, Elsevier, 1994.
- [18] M. Lesieur and O. Métais, “New trends in large-eddy simulations of turbulence,” *Annual Review of Fluid Mechanics*, vol. 28, pp. 45–82, 1996.
- [19] J.-L. Guermond, J. T. Oden, and S. Prudhomme, “Mathematical perspectives on Large Eddy Simulation models for turbulent flows,” *Journal of Mathematical Fluid Mechanics*, vol. 6, no. 2, pp. 194–248, 2004.
- [20] P. Sagaut, *Large Eddy Simulation for Incompressible Flows: An Introduction*, *Scientific Computation*, Springer, New York, NY, USA, 2006.
- [21] J. R. Lee, J. Kim, and C. -H. Song, “Synthesis of the turbulent mixing in a rod bundle with vaned spacer grids based on the OECD-KAERI CFD benchmark exercise,” *Nuclear Engineering and Design*, 2014.
- [22] J. Mahaffy et al., “Best practice guidelines for the use of CFD in nuclear reactor safety applications,” NEA/CSNI/R(2007)5, 2007.

- [23] ANSYS Academic Research, *Release 13.0, Help System*, ANSYS CFX-Solver Theory Guide, ANSYS Inc., 2010.
- [24] ANSYS Academic Research, *Release 13.0, Help System*, ANSYS CFX-Solver Modeling Guide, ANSYS Inc., 2010.
- [25] J. Meyers, B. Geurts, and P. Sagaut, *Quality and Reliability of Large-Eddy Simulations*, vol. 12 of *ERCOFTAC Series: European Research Community on Flow, Turbulence and Combustion*, Springer, Berlin, Germany, 2008.

## Research Article

# Uniform versus Nonuniform Axial Power Distribution in Rod Bundle CHF Experiments

**Baowen Yang, Jianqiang Shan, Junli Gou, Hui Zhang, Aiguo Liu, and Hu Mao**

*Science and Technology Center for Advanced Fuel Research & Development, School of Nuclear Science and Technology, Xi'an Jiaotong University, Xi'an 710049, China*

Correspondence should be addressed to Junli Gou; [junligou@mail.xjtu.edu.cn](mailto:junligou@mail.xjtu.edu.cn)

Received 30 December 2013; Accepted 7 May 2014; Published 27 May 2014

Academic Editor: Bin Zhang

Copyright © 2014 Baowen Yang et al. This is an open access article distributed under the Creative Commons Attribution License, which permits unrestricted use, distribution, and reproduction in any medium, provided the original work is properly cited.

Rod bundle experiments with axially uniform and nonuniform heat fluxes are examined to explore the potential limitations of using uniform rod bundle CHF data for CHF correlation development of light water reactors with nonuniform axial power distribution (APD). The case of upstream burnout is presented as an example of unique phenomena associated with nonuniform rod bundle CHF experiments. It is a result from combined effect of axial nonuniform power shape and different interchannel mixing mechanisms. In addition, several key parameters are investigated with respect to their potential impacts on the thermal-hydraulic behaviors between rod bundles with uniform and nonuniform APDs. This type of misrepresentation cannot be amended or compensated through the use of correction factors due to the lack of critical information in the uniform rod bundle CHF testing as well as the fundamental difference in the underlining driving mechanisms. Other potential issues involved with the use of uniform rod bundle CHF data for nonuniform APD system applications also present strong evidence concerning the limitations and inadequacy of using uniform rod bundle CHF data for the correlation, prediction, and design limit calculation for safety analysis.

## 1. Introduction

In the light water reactors, one of the limiting conditions for safety operations is determined by the heat transfer capacity between the cooling water and the fuel clad, limited by the departure from nucleate boiling (DNB) or dryout (DO) phenomena, while local heat flux exceeds critical heat flux (CHF). Due to complex subchannel geometry as well as the broad range of thermal-hydraulic conditions, the measurement, prediction, and enhancement of the CHF limits for the light water reactor continue to be a challenging task [1]. The advancement of mixing vane grid and fuel assembly design increases the concerns of high flux density requirements that come with increasing fuel burnup and the broad range thermal-hydraulic conditions (extending from high pressure, high flow, down to low pressure, and low flow after the Fukushima accident, especially for the advanced reactor design using passive cooling concept) [2]. Furthermore, the expected CHF performance as well as power margin improvement is becoming a critical issue

which not only demands design improvement for a high CHF performance mixing vane grid design, but also requires accurate and representative CHF measurement as well as predicting scheme. Since the closing of CHF test facility at Columbia University (CU-HTRF) [3], there is a growing concern not only for the lack of standard for the requirement on how and when the rod bundle CHF data from the newly established vendor-operated rod bundle CHF test facility should be independently verified or calibrated, but also on the trend of continuing relaxing requirements for rod bundle CHF correlation development and CHF prediction mechanism, as well as safety analysis evaluation.

In the past, the practice of conservative approach in analyzing, correlating, and applying any experimental data for nuclear design, operation, and safety analysis has limited any extrapolation of applicable ranges (operating or geometry range) supported by reliable and validated experimental data, especially when different thermal-hydraulic mechanism might be involved in the extended areas. Recently, with pressure from increasing demand on high power density

and broader range of operating condition as well as the lack of fully benchmarked rod bundle CHF testing facility, progressive computational and statistical schemes are aggressively applied to analyze limited amount of available data through various optimal correlation and statistical analysis schemes. In some cases, the so-called “statistical poolability” scheme was applied to utilize unrelated CHF data (with different test geometries or conditions) and to extrapolate the application range of the CHF correlation to a totally untested domain for the particular fuel design disregarding significant difference in underlining fuel design characteristics as well as major difference in basic physical phenomena. Without actual improvement in the fuel design, the recent advancement in data treatment methodologies, the increasingly aggressive data analysis and optimization schemes, and the relaxing in requirements on rod bundle CHF experimental data have taken away more and more safety margins without proper experimental verification and supports. Similar voice was raised by Herer that “optimized correlations and advanced methodologies reduce this margin” [4]. This concern is especially valid considering the void of a totally benchmarked and fully established facility after the closing of Columbia University, Heat Transfer Research Facility (HTRF). Even with the continuous claims of so called “benchmarking facility” in recent publications [5, 6], most of the data presented in these papers were limited to very narrow range of test conditions with selected grid design only.

With the recent reducing safety margin in data analysis due to the overly optimized correlation and aggressive data treatment methodologies, the requirements for experimental accuracy as well as the reliability of “representation” between the simulated experiment and the targeted thermal-hydraulic event have again become the focus of attention. In particular, several critical issues concerning the “accuracy” and/or “representation” in various aspects of rod bundle CHF experiments have become subjects of review and/or concern. These issues include, but are not limited to, the impacts of rod bow on CHF performance (Can the bow rod penalty derived from over 30-year-old uniform rod bundle CHF data with very primitive vaneless grids still be applicable for the current advanced fuel application?), the interpretation and usage of cold rod CHF data, the steadiness of rod bundle CHF testing operation, the effect of heater length, the impact of various experimental measurement uncertainties, and the application of uniform rod bundle CHF data in CHF correlation development, prediction, and safety analysis for the reactor core with nonuniform APD. Some examples of measurement uncertainties include the root cause and propagation of the measurement uncertainty of each individual measurement (especially the primary measurement, such as the inlet temperature, the flow rate, the heat flux measurement, etc.), the operating uncertainty (uncertainty and repeatability between experimental operations, between test bundles, and between test facilities), heat loss measurement and calculation as well as its application. Other potential concerned issues also include variations in experimental or operational design and setups, involving but are not limited to bundle tilt or misalignment, rod bow,

excessive heat loss, bypass flow (in or out), uneven rod-to wall gap distribution, local flow blockage, and so forth.

In this paper, the particular issue of applying uniform rod bundle CHF data for the development of CHF correlation, prediction, and design limit safety analysis of nuclear reactor with nonuniform axial power distribution is examined. Several potential limitations and inadequacy in this type of application are explored. The limitations or lack of true representation in uniform rod bundle CHF data is mainly due to underlining deviations in simulating the thermal hydraulic phenomena leading to CHF event, which include but are not limited to the following.

(1) There is a lack of heated length effect or true heated length effect in uniform axial heated rod bundle CHF experiments. This type of heated length effect is normally observed in the CHF data from rod bundles with nonuniform axial power distribution under high quality, low pressure conditions.

(2) In the uniform rod bundle CHF test, there is also a lack of combined local heat flux and quality effect on initiating or triggering the critical heat flux limit that is dominated by either departure from nuclear boiling (DNB) or dryout (DO) events. With the uniform axial power distribution, the CHF (or physical burnout, including DO and DNB events) always occurs near the end of the heater length where the maximum quality is the predominating cause of driving the CHF event. In an axial uniform heated system, it is very difficult to simulate high subcooled DNB events with high subcooled, high local heat flux and relatively low local quality conditions as often observed in high axial heat flux peaking nonuniform heating systems.

(3) In the uniform rod bundle CHF testing, there is also lack of information related to burnout location driven by local heat flux and/or local heat flux gradient which can be only observed in a nonuniform APD heating system. Therefore, information from uniform rod bundle CHF data cannot be used to predict burnout location in a nonuniform rod bundle assembly. This is one of the main reasons why the burnout location predictability is usually very low for CHF correlation developed based on uniform CHF data or nonuniform CHF data with nonprototypical test conditions, heater length, or power profile. A recent example of PWR rod bundle CHF correlation developed based on mostly uniform data (with few 12 feet nonuniform rod bundle CHF data) demonstrates an extreme low predictability (below 50%) of burnout location for 14 feet cosine nonuniform CHF test cases. For the same reason, in an exit peak skew power profile (top peak mu-sign-mu power shape) case, since most of the CHF events occur near the exit peak location, this type of nonuniform APD does not really contain much of variation in combining heat flux and quality impact on burnout location. Therefore, this type of data should not be used in the statistics in evaluating the location predictability of a correlation in predicting the CHF location for a system with axial nonuniform power profile.

(4) It is impossible to properly derive the needed  $F$ -factor using uniform rod bundle CHF test data. In fact, it would require several sets of nonuniform CHF data with different APDs, including axial uniform APD, to correlate and obtain

a reasonable  $F$ -factor value to cover the conventional range of PWR thermal-hydraulic conditions.

(5) The effect of different grid spacing related terms (dg: distance to upstream grid; gsp: grid spacing; or Cgsp: current grid spacing, etc.) is very difficult or extremely complicated to simulate using heater rods with uniform axial power profile. This is especially true when intermediate flow mixers are used that lead to not only potentially different gsp or dg term with possibility of upstream burnout, but also the possibility of the effect from different upstream grid designs (either MVG or intermediate flow mixing device) and alignment.

(6) There is no information related to burnout location in a nonuniform APD heating system (except for the exit peak skew power distribution) that can be obtained in uniform APD rod bundle CHF experiments. In the past, uniform rod bundle CHF data obtained using different upstream grids (either regular MVG or intermediate flow mixing device (or flow mixer)) were treated indiscriminately. That is, the intermediate flow mixing device (MSMG, IFM, or any short form of the MVG that is used in between two regular MVGs) was treated as a regular MVG grid with uniform rod bundle CHF. The only difference in this consideration is full span or half span. With gradually diverting design in not only mixing vane but also dimple, spring type, grid strap, and other key components, there is increasing potential of significant difference in thermal-hydraulic performance between regular mixing vane grid and the intermediate flow mixing grid/device. In a case example of intermediate flow mixing device (MSMG or IFM) application, different grid performance between regular MVG and the intermediate flow mixer was observed during the nonuniform heat flux CHF testing where the majority of CHF occurred at immediate downstream of regular MVG grid, instead of immediate downstream of the most expected intermediate flow mixer due to its relatively shorter grid height. This type of different mixing performance was very difficult to examine with uniform APD rod bundle CHF experiments. It was often mistakenly neglected when uniform heater rod was used for rod bundle CHF testing with only one grid spacing term where the particular grid type (MVG or intermediate flow mixer (or mixing device)) of the grid upstream of CHF event was not taken into consideration.

## 2. Uniform ADP for Nonuniform ADP Application-Tong's $F$ -Factor Approach

In the history of rod bundle CHF correlation development, both uniform and nonuniform axial flux shapes (AFS) have been tested for various fuel designs.

A rod bundle CHF experiment with an axial uniform power distribution costs much less (at least two- to three-folds) than a similar rod bundle CHF testing using a nonuniform axial power distribution. With most relatively slow events (mostly dry out (DO) type CHF) and easily predicted burnout location (near the end of heater rod), the rod bundle CHF experiment with uniform axial heat flux distribution is a much easier option than a nonuniform APD. Based on both economic and technical considerations, uniform APD is

often used as the substitute for the much challenging nonuniform APD rod bundle CHF experiments for the purpose of CHF correlation development, CHF prediction, and design limit (DL) safety analysis.

In order to apply CHF data from uniform APD rod bundles for Non-uniform APD reactor core application, it is a common practice to apply Tong's  $F$ -factor for power shape correction to account for the total accumulated energy input at any given axial elevation.

It is well known that, for predicting CHF, a method has been derived by Tong through introducing an  $F$ -factor to account for the effect of the heat flux profile on the local CHF value. Derived from empirical correlation based on data obtained using rod bundles with different APDs, the  $F$ -factor is often used for test bundles with both uniform and nonuniform power profiles to account for the energy accumulated in the bubble layer up to the concerned location [7]. Most PWR CHF correlations, like W-3 and FC2000, use this method to consider the impact of the axial heat flux shape. The  $F$ -factor is defined as

$$F = \frac{q_{CHF,U}}{q_{CHF}}, \quad (1)$$

where  $q_{CHF,U}$  is the CHF calculated by means of the correlation for a axially uniform heat flux shape and  $q_{CHF}$  is the CHF in the case of a nonuniform heat flux. An energy balance for the bubble layer provides the analytical expression of  $F$  (Tong):

$$F = \frac{K}{q(l_{DNB})(1 - e^{-K(l_{DNB}-l_o)})} \int_{l_o}^{l_{DNB}} q(z) e^{-K(l_{DNB}-z)} dz, \quad (2)$$

where  $l_{DNB}$  is the location of DNB,  $l_o$  is the elevation of onset of the boiling,  $q(z)$  is the local heat flux and  $K$  is an experimental coefficient describing the heat and mass transfer effectiveness at the bubble-layer/subcooled-liquid-core interface as given by

$$K = \frac{b_1(1-X)^{b_2}}{G^{b_3}}, \quad (3)$$

$X$  is the local quality,  $G$  is the local mass flux, and  $b_1$ ,  $b_2$ , and  $b_3$  are optimized coefficients of the  $F$ . These coefficients are usually optimized using the non-uniform rod bundle CHF data. These values are usually different depending on each correlation. For example, in BW-2 Correlation,  $b_1 = 0.15$ ,  $b_2 = 4.31$ , and  $b_3 = 0.478$ ; on the other hand, in W-3 Correlation,  $b_1 = 0.44$ ,  $b_2 = 7.9$ , and  $b_3 = 1.72$ , and so forth.

The  $F$ -factor indicates the memory effect of the upstream heat flux profile on the CHF and accounts for the difference in the amount of energy accumulated in the bubble layer up to the location of interest. The quantity  $1/K$ , which shows up in the exponential function, defines an exponentially decaying behavior with respect to the axial distance below the CHF location because  $K$  decreases as the quality increases as given in (3). The starting elevation of integration may be taken to be either the inception of local boiling or the inlet. In the limit of very high qualities ( $X > 0.2$ ), DNB is no longer

the dominant CHF mechanism, and the occurrence of CHF might be considered as a global phenomenon, with little dependence on the local value of the heat flux.

### 3. Challenges to the Application of Uniform APD CHF Experiment to Simulate a Non-Uniform APD System

The above  $F$ -factor is based on integrated energy approach considering only total energy input up to a certain local elevation for a uniform or nonuniform heated channel. This  $F$ -factor correction reflects mostly the total quality up to the concerned elevation, without any implication or gradient of the local heat flux. The application of  $F$ -factor heavily relies on the assumption that the DNB is no longer a dominant CHF mechanism.

Although adjustment factor, such as Tong's  $F$ -factor, is usually applied for correction of uniform CHF data for Non-uniform APD, this local adjustment does not represent the true local condition, especially the condition that might have impacts on the mixing performance as well as the occurring of DNB, such as local heat flux peaking.

As shown in Figure 1, for the axially uniformly heated test section, the CHF will most likely occur at the exit of the test section where the quality is at its maximum. That is, the CHF will most likely occur as a maximum quality driven event. On the other hand, for an axially nonuniform heated rod, with the exception of exit peak skew power shape, the CHF does not always occur at a certain elevation (exit peak or channel exit); rather, it often occurs at a location based on the combined effect of local quality and heat flux peaking. For an axial cosine effect of power shape, the actual burnout (or CHF) often occurs at various elevations, from the mid-span area (upstream and downstream of mid-span) all the way up to near about 10% from the end of heated length (but not at the end of heated length, except for a very extremely low peaking power shape such as the uniform axial APD case or exit power peaking case). The actual burnout location for an axially nonuniform power distribution heater tube is depending on the operating condition, the actual power shape, grid alignment/configuration, the grid span, and, most importantly, the actual mixing and turbulent promoting performance of the mixing vane grid.

In a typical nonuniform APD case of rod bundle CHF with a cosine axial power distribution, under normal operating condition and similar mixing vane grid and similar grid spacing at each elevation, as shown in Figures 2 and 3, the CHF often occurs near 2/3 elevation of the entire heated length. However, the actual mixing effect of any given mixing promoter at any elevation is often affected by the type of mixing promoters, difference in grid spacing, mixing vane grid alignment, and, most importantly, the difference in local thermal-hydraulic conditions, including not only the local quality, local liquid, and vapor superficial velocity, but also the local heat flux as well as the gradient of local heat flux itself. Depending on the type of grid design, these local conditions might have significant impacts on mixing vane performance in terms of cross flow mixing effect (cross flow factor), local

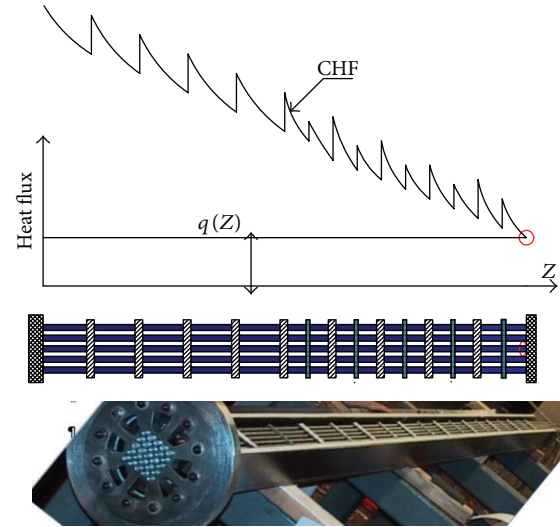


FIGURE 1: Rod bundle CHF with uniform axial power distribution. (CHF mostly occurs at the end of heated length.)

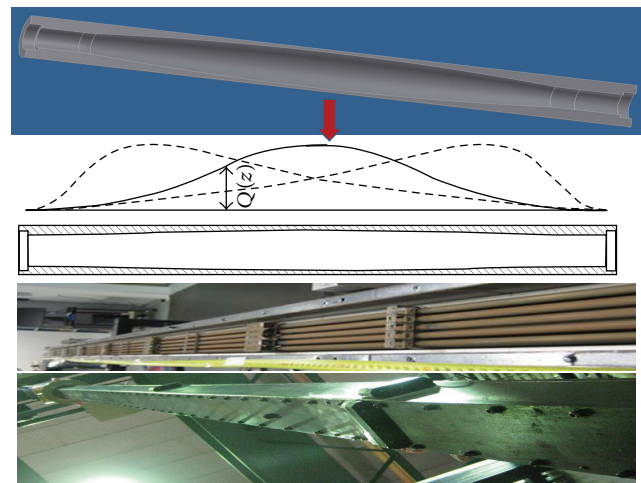


FIGURE 2: Rod bundle CHF with nonuniform axial power distribution.

turbulent intensity, angular moment, and presence of swirl flow (swirl ratio factor or swirl mixing ratio), as well as two-phase flow bubble and turbulent dynamics. The actual mixing effect will in turn not only impact the actual CHF power level and influence the CHF mechanism, but also affect the elevation and location where burnout (or CHF) occurs. In summary, the performance of mixing promoters is dependent on both the design of the mixing grids and the local thermal-hydraulic conditions. For example, as shown in Figure 4, when two different grids are applied in the same bundle assembly (in the most common cases of regular mixing vane grid (MVG) with intermediate flow mixing device) since the regular MVG and the intermediate flow mixing device do not always have exactly the same grid design (even though they might have the same vane shape, size, and pattern, the spring, dimple, and the height are often different from each other),

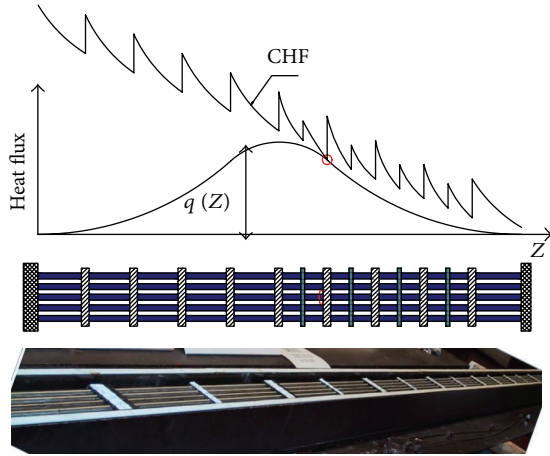


FIGURE 3: Rod bundle CHF with nonuniform APD. With the example of cosine axial power distribution, under normal operating condition and similar mixing vane grid and similar grid span at each elevation, the CHF mostly occurs near 2/3 elevation of the entire heated length.

the CHF burnout location can vary depending on the actual grid location, the grid spacing, the grid alignment, and local operating conditions (see Figure 5). The difference in mixing performance between regular MVG and the intermediate flow mixing device is often overlooked in the CHF tests using rod bundle with uniform APD.

As a matter of fact, with two or more different mixing vane grid designs (such as regular MVG and the intermediate flow mixing device) in the same test bundle, the location/elevation of CHF occurrence in the nonuniform APD bundle experiment could be a good indication of which type of grid has better CHF performance. For example, as mentioned above, if the MVG and intermediate flow mixing device are alternatively positioned along the heater length, based on conventional wisdom, most of CHF events would occur directly downstream of intermediate flow mixing device due to the fact that it is a relatively shorter grid with lower pressure drop. Therefore, the regular MVG should have better mixing performance than the much shorter and simpler intermediate flow mixing device. However, in the past, the opposite situation was also observed (CHF occurred directly downstream of regular MVG grid) for a certain type of intermediate flow mixing devices. This type of CHF events provide strong indication that intermediate flow mixing device, although shorter, might produce better mixing performance than the taller version of regular mixing vane grid. This type of CHF data from non-uniform rod bundle CHF experiments provide clear evidence that MVG and intermediate flow mixing devices are indeed different from each other, with different thermal-hydraulic performance, and should be considered as two separate grid types. They should have different mixing performances with different TDCs (thermal diffusion coefficient) and should be handled differently in the CHF correlation, prediction, and safety analysis processes. In the case of CHF testing with uniform APD, the CHF will most likely occur at the end of heated

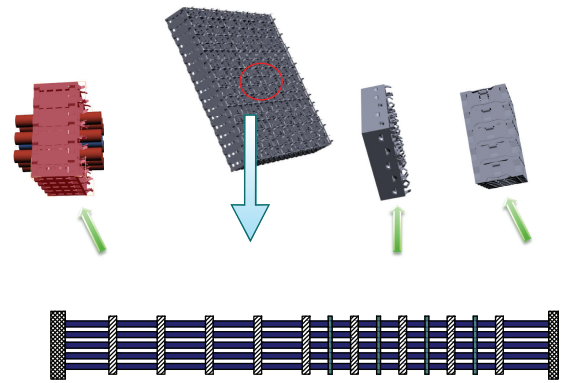


FIGURE 4: A rod bundle assembly with grids of different designs located at various elevations with different grid spans and different grid alignments.

length independent of the upstream alignment of mixing vane grid, either regular MVG or intermediate flow mixing device.

In the following illustration case of the rod bundle CHF experiment, the nonuniform CHF experiment has most (or all) of the CHF thermocouple indications located at level 4 (T/C#4), downstream of regular MVG (Mixing Vane Grid) instead of level 3 or level 5. This is an indication that, for these particular grids, although the intermediate flow mixing device (MSG or IFM, etc.) is a much shorter grid with lower pressure drop and similar vane pattern, it has better CHF performance than regular MVG.

In the above case, if a bundle assembly consists of two or more types of mixing vane grids, such as regular MVG and intermediate flow mixing device (mixer), and so forth, the alignment of the last two grids (assuming the grid directly upstream of the burnout location has the most direct impact on the CHF performance) becomes a major challenging decision for a CHF test using a rod bundle with uniform axial power distribution. In this case, the conventional arrangement of having intermediate flow mixing device (MSMG or IFM) at the middle of the last span of the bundle could be a nonconservative approach, because it will be mostly measuring the CHF performance of a higher performing grid (MSMG or IFM) rather than the lower CHF performance of a MVG grid. Detailed discussion on this can be seen in the following section.

As shown in Figure 6, considering the potential difference in thermal-hydraulic performance between the regular MVG and the intermediate flow mixing device, the last two grid alignments can be various in many ways, not only the grid spacing, but also the alignment between the regular MVG and the intermediate flow mixing device (IFM, MSMG, etc.) in order to truly represent or simulate the CHF events in a nonuniform axial power distribution (APD) system, such as the reactor core. In a most common cosine power shape case, with the most popular alignment of having intermediate flow mixing devices only used at the downstream half of the fuel assembly, since the CHF could happen upstream or

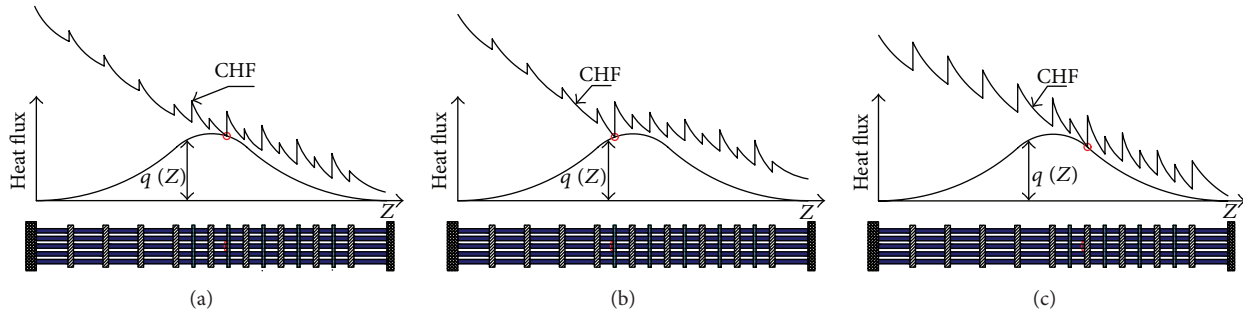


FIGURE 5: Actual burnout (CHF) location in a rod bundle with cosine APD can vary depending on the actual grid location, the grid span, and the grid alignment, as well as local operating conditions.

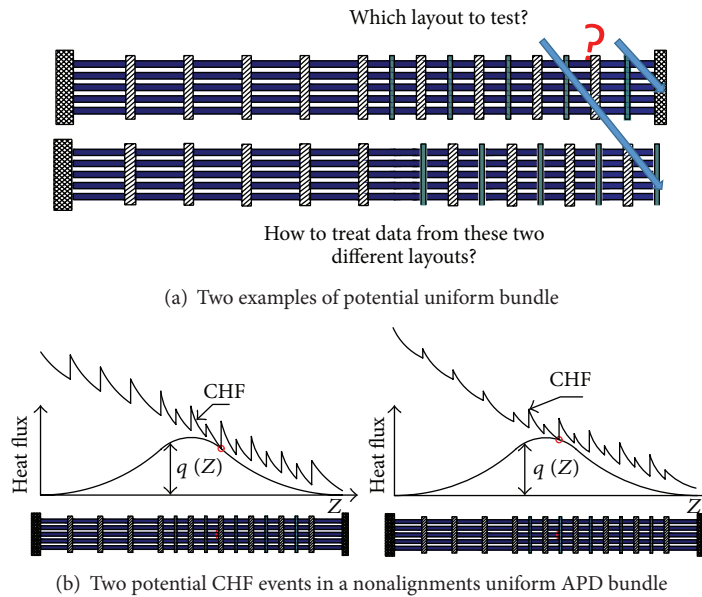


FIGURE 6: In uniform APD CHF experiment, the last two grid alignments can be various in many ways (only two examples are illustrated here (see Figure 6(a)) in order to simulate the occurring of CHF events in a nonuniform APD system (see Figure 6(b)).

downstream of the mid-span of the rod bundle, the last grid span could be a full span or a half span alignment. In order to account for the impact from the most affective grid, which is just at the upstream of the burnout location, various mixing vane grids, grid configurations, and grid spacing (half or full grid span) must be examined. Furthermore, considering the potential impact of (incoming) local thermal-hydraulic conditions on the mixing performance of a mixing vane grid at any given elevation, it is also important to take into account the accumulated mixing performance from the upstream mixing vane grids and their alignment. That is, for any rod bundle CHF testing with different grid spacing and involving different grid types (both regular MVG and intermediate flow mixing devices), if rod bundle CHF tests are performed using uniform axial power distribution bundle assembly to simulate CHF or thermal hydraulic event in a nonuniform axial power distribution system, all the potential combinations of grid type, grid spacing (full span and half span or any other span actually used in the reactor), and grid alignments should be

performed in order to include all possible events covering the basic underlining physical phenomena. It will be also a major challenge to handle, interpret, and analyze all the data obtained from the above listed potential combined configurations with proper Tong's  $F$ -factor (or  $F$ -factors) or other correction factor in order to apply this type of uniform rod bundle CHF data for nonuniform power shape system application.

*3.1. Summary of Challenges and Limitations in Applying Uniform APD Rod Bundle CHF Data for Nonuniform APD Rod Bundle Applications.* As described above, some potential constraints and challenging issues involved in the use of CHF data from uniform rod bundle CHF testing for nonuniform axial power shape heating application are summarized as follows.

(1) It is extremely difficult or impossible to use a rod bundle with uniform APD to simulate the CHF event that occurs

in a nonuniform APD system. This dissimilarity presents the fundamental difference or deficiency in simulating a nonuniform rod bundle CHF using uniform rod bundle CHF data.

(2) Effect of heated length it is well known that as long as the total length of the heater rod is longer than the mixing length of the mixing grid, CHF testing with uniform APD will most likely reveal no heater length effect on measuring CHF. On the other hand, effect of heated length on CHF is often observed in case of nonuniform APD, especially under nonlocal CHF event.

(3) There is a lack of prototypical combined local heat flux and local quality driven mechanism leading to the CHF limit or to the incipient of heat transfer deterioration. That is, in case of uniform APD, CHF always occurs at  $X_{max}$ . It is a maximum quality driven and dominating event with very limited local heat flux effect. With the axial uniform heat flux profile, it is rather difficult to simulate high subcooled DNB behavior. This is quite different from a nonuniform APD case, where CHF or DNB seldom or never occurs at the point of maximum quality. Just like axial nonuniform power profile in the reactor core, the CHF limit in a nonuniform axial heat flux experiment often reaches a combined effect of local quality and local heat flux (sometimes even local heat flux gradient). In a channel with axial non-uniform power input, the potential CHF mechanism covers wide range of thermal-hydraulic phenomena from high quality dryout, to relatively subcooled DNB event, to potentially homogeneous nucleation behavior (to be discussed in a separate paper)—a mainly local heat flux driven event which might occur off the heater wall at or before the NVG (Net Vapor Generation) point. In the non-uniform case, since the CHF never occurs at the end of heater rods, in some cases, integral effect has major impact on the thermal hydraulic behavior, especially in the low flow, low pressure flow instability case. This type of integral effect will not happen in the uniform heater rod cases where CHF mostly occurs with the maximum quality at the end of heater rod.

(4) In a uniform heated test section, it is very difficult or impossible to reach high subcooled/high flux and relatively low local quality condition DNB event as often seen in high axial peaking nonuniform power shape axial heating systems.

(5) It is rather impossible to derive the needed  $F$ -factor using uniform rod bundle CHF test data alone. In fact, it would require several sets of nonuniform CHF data with different APD including axial uniform APD to correlate and obtain a reliable  $F$ -factor value. Usually, for the three coefficients to be optimized in the Tong's  $F$ -factor, for any given geometry (one particular heater length, or grid span, or test configuration, etc.), at least three sets of nonuniform rod bundle CHF test data should be obtained. More sets of CHF data with different power shapes or test configurations should be required if more than one particular set of test geometries are needed for the CHF correlation to cover. That is, the  $F$ -factor requires several sets (usually 6 sets or more CHF tests are needed to cover a minimum of two configurations—typical cell and thimble cell configurations) of nonuniform CHF data with different APD including axial uniform APD, to correlate and obtain a correcting factor in order to cover various power shape or axial distribution profiles that might

occur in the reactor throughout the life cycle of the particular fuel.

(6) No information related to burnout location in a nonuniform APD heating system can be obtained from uniform APD rod bundle CHF experiments.

In the nonuniform heat flux (APD) case, the location of CHF (DNB or DO) usually depends on the power shape (cosine, top peak, bottom peak, etc.), grid design and alignment, and heater length, as well as other global and local test conditions which are designed to simulate the actual thermal-hydraulic system. Therefore, it is critical for a CHF correlation derived from the rod bundle CHF data to include information relating the actual burnout location to its dependent variables. A CHF correlation developed based on sufficient sets of CHF test data (normally 6 sets or more) with at least four or more different power shapes is needed to achieve reasonable burnout location prediction accuracy.

On the other hand, since all or most of the CHF occur at the end of the heater rod, there is no burnout location information relating to local heat flux revealing in the CHF data using rod bundles with uniform heat flux (APD). Subsequently, the CHF correlation developed based on uniform rod bundle CHF data will not be able to predict actual burnout location for a nonuniform heat flux (APD) heating system. One good example of the issue involving burnout location predictability is one of the latest released PWR CHF correlations for 14 feet bundle application. This correlation was developed based on mostly uniform rod bundle CHF data plus some 12 feet cosine bundle data points. Unfortunately, without proper information (only one set of 14 feet cosine bundle CHF data), this correlation can only predict the burnout locations for the 14 feet cosine case with lower than 50% success rate. Although an additional set of exit peak skew bundle CHF data was added to raise the “so-called” nonuniform power shape burnout location predictability, this high prediction accuracy should not be credited for its general burnout location prediction accuracy because, in the exit peak case, most of the CHF events as expected should occur near the exit peak location. High prediction accuracy in the case of exit peak skew power shape has no guaranty or relevance to the prediction accuracy of other nonuniform APD cases.

Based on the above illustration, it is very clear that there is lack of information from uniform rod bundle CHF data related to burnout location in a nonuniform APD heating system. This deficiency presents a major difficulty for using uniform rod bundle CHF data to predict burnout location in a nonuniform rod bundle assembly. Unfortunately, this inability of predicting other burnout locations of the nonuniform rod bundle CHF testing results is often misleadingly reported by the vendor as a SPECIAL capability of their CHF code in predicting CHF location precisely and repeatedly for their test cases of another uniform rod bundle CHF tests (always at the end of heated length).

(7) With a uniform axial flux shape heater, it is impossible to obtain data with upstream burnout as observed in a nonuniform axial flux shape system with high performance mixing vane grids.

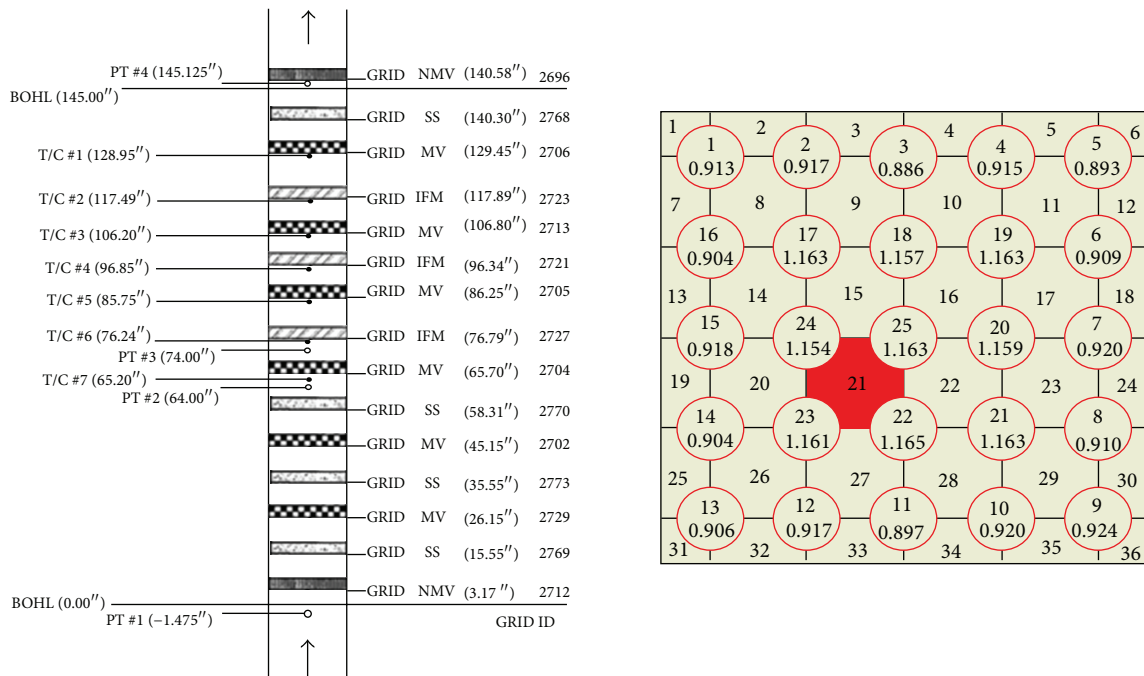


FIGURE 7: A case example of a  $5 \times 5$  bundle configuration.

As shown in Figure 5, for more and more nowadays high performance mixing vane grids, there is an increasing frequency that burnout occurs upstream of a midspan, referred to as an upstream burnout. In a heated channel with axial cosine power profile, the upstream burnout usually occurs upstream before the midspan (50% elevation), with the same local heat flux but lower local quality than the correspondent position downstream of the midspan. In this case, CHF occurs upstream of midspan most likely due to effective heterogeneous mixing downstream or possible homogenous nucleation mechanism (to be discussed further in a separate paper) at upstream location. This type of upstream burnout occurs more often for the fuel assembly with high mixing performance grids under relatively high flow rate, high local subcooled, and high local heat flux conditions. This type of upstream burnout phenomena will never occur in CHF experiments with uniform APD rod bundles. This is another example that CHF data obtained from uniform axial power distribution rod bundles cannot closely resemble thermal hydraulic condition in the reactor and should not be used for the safety analysis of nuclear power plant. The upstream burnout phenomena also demonstrate accumulated quality (or energy) type of correction factor, such as the  $F$ -factor, incapable of accurately reflecting such unique thermal-hydraulic phenomena associated with local heat flux effect in an axial high peaking nonuniform heat flux (nonuniform APD).

One of the rod bundle CHF experiments with upstream burnout data is illustrated in the following case example. As shown in the test geometry (Figure 7) for a series of rod bundle CHF tests performed in a  $5 \times 5$  test geometry, there are at least 7 upstream CHF data points (out of 52 CHF points)

occurring at thermocouples level number 7 (below midspan elevation), where, with similar local heat flux and axial cosine power distribution, the local quality is lower at level 7 as compared to its correspondent downstream location. One example is Run number 49, with  $G = 3.52 \text{ Mg/m}^2\text{s}$ ,  $P_{\text{exit}} = 1800 \text{ psi}$ ,  $T_{\text{inlet}} = 576.8 \text{ F}$ , and CHF occurred at TC number 7 at rod number 21 (T/C21.7) with CHF power of  $2.31 \text{ MW/m}^2$ . Figure 8 gives the local equilibrium qualities and local mass fluxes in subchannels at different axial locations. This type of upstream burnout will not happen in an experiment with axially uniformly heated rod bundle.

(8) Effect of different grid spacing term ( $dg$  and  $gsp$  or  $Cgsp$ ) is very difficult or complicated to derive from CHF data obtained from heater rods with uniform axial power profile.

This is especially true when intermediate flow mixers are used; they lead to not only potentially different  $gsp$  or  $dg$  term with potential upstream burnout but also possibly different upstream grid design (either MVG or intermediate flow mixing device/grid).

In the past, in case of fuel assembly with only one type of mixing vane grid (MVG) and one fixed grid span, the uniform rod bundle CHF test was conducted using only one type of simple configuration. However, with the frequent use of intermediate flow mixer and different grid spacing, the uniform rod bundle CHF simulation should take into account both vane type and grid spacing effect. The difference between these two types of mixing grids (MVG and intermediate flow mixing device) was not only verified by the CFD modeling, but also clearly indicated in the actual nonuniform rod bundle CHF experiments as discussed in the previous section. As shown in Figures 5 and 6 and the discussion above, in order to simulate different fuel

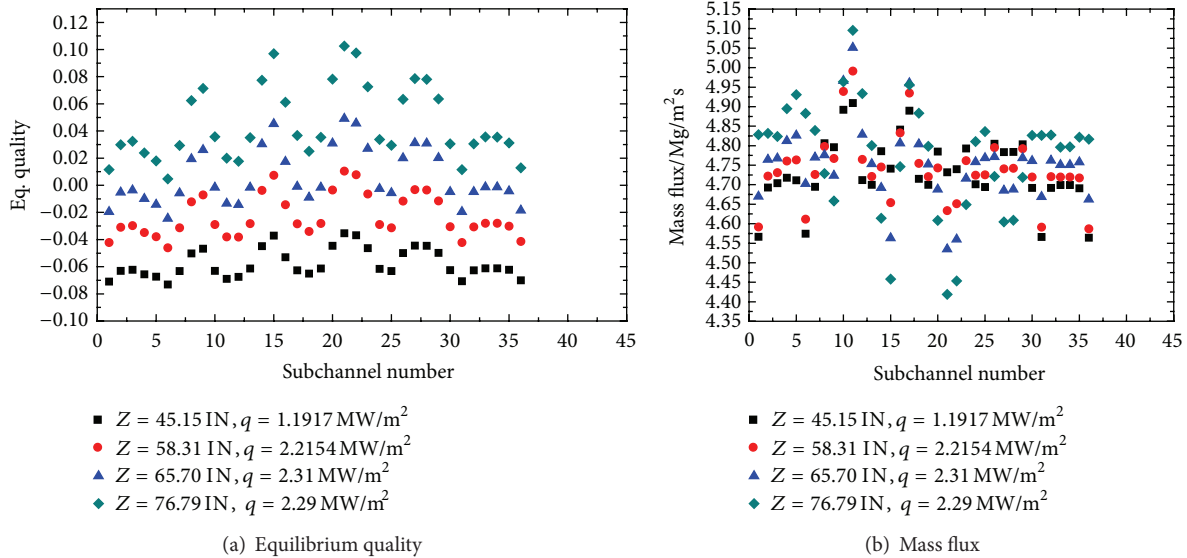


FIGURE 8: Subchannel equilibrium quality and mass flux at different grid levels.

alignments for the last span and the effect of grid type for the grid upstream of the burnout location, there are many potential combinations of grid alignments, grid spacing, and overall power shape in order to simulate the local thermal-hydraulic conditions leading to the true CHF events of interest. The interpretation and analysis of such uniform rod bundle CHF data as well as the prediction capability (both CHF power and CHF location) derived from this type of data should be a subject of major challenge.

#### 4. Conclusion and Recommendation

Both uniform and nonuniform axial power distributions (APDs) have been tested for rod bundle CHF experiments. Although adjustment factor, such as Tong's  $F$ -factor, is usually developed through correlation and applied as a correction factor to account for the total accumulated energy input when compared to data obtained from nonuniform heater, this local adjustment does not represent the true local condition, especially the condition that might have an impact on the occurring of DNB, such as local heat flux as well as local heat flux gradient. Considering the above described limitation or deviation of using uniform rod bundle CHF data and the fact that this type of deviation cannot be amended or compensated through the use of correcting factor such as Tong's  $F$ -factor, it is obvious that the current use of uniform rod bundle CHF data for nonuniform power core safety analysis can be nonprototypical and nonconservative (especially the potential of missing extremely high subcooled DNB type data) and should be investigated or explored further. With nowadays advanced statistical analysis approach and aggressive utilization of CHF power margin, the use of uniform rod bundle CHF data for safety analysis of axially nonuniformly heated reactor core definitely calls for further critical reexamination.

#### Conflict of Interests

The authors declare that there is no conflict of interests regarding the publication of this paper.

#### References

- [1] W. Liu and H. Nariai, "Viewpoint of subcooled flow boiling critical heat flux mechanism," *Chemical Engineering & Technology*, vol. 25, no. 9, pp. 447–453, 2002.
- [2] D. K. Chandraker, P. K. Vijayan, D. Saha et al., "A comprehensive review of the CHF prediction methodologies for the fuel rod bundle," in *Proceedings of the 13th International Meeting on Nuclear Reactor Thermal Hydraulics (NURETH-13 '09)*, Paper: N13P1029, Kanazawa, Japan, September 2009.
- [3] CU-HTRF-2001-W1010, *Critical Heat Flux Tests on PWR Fuel Assemblies for Westinghouse Electric Company Test No. 101.0*, 2001.
- [4] C. Herer, "Questions relative to chf testing for new pressurized water reactor advanced fuel assemblies," in *Proceedings of the 18th International Conference on Nuclear Engineering (ICONE-18 '10)*, pp. 729–736, Xi'an, China, May 2010.
- [5] L. D. Smith, A. Hallehn et al., "Benchmark testing the oden CHF loop to Columbia University HTRF," in *Proceedings of the 14th International Meeting on Nuclear Reactor Thermal Hydraulics (NURETH-14 '11)*, NURETH-14-368, Ontario, Canada, September 2011.
- [6] C. Herer, A. Beisiegel, P. Imbert et al., "Comparison of PWR fuel assembly CHF tests obtained at three different test facilities," in *Proceedings of the 11th International Meeting on Nuclear Reactor Thermal Hydraulics (NURETH-11 '05)*, Paper: 117, Avignon, France, October 2005.
- [7] L. S. Tong and Y. S. Tang, *Boiling Heat Transfer and Two-Phase Flow*, Taylor and Francis, Washington, DC, USA, 1997.

## Research Article

# Effect of Flow Blockage on the Coolability during Reflood in a $2 \times 2$ Rod Bundle

**Kihwan Kim, Byung-Jae Kim, Young-Jung Youn, Hae-Seob Choi, Sang-Ki Moon, and Chul-Hwa Song**

*Korea Atomic Energy Research Institute, Daedeok-daero 989-111, Yuseong-Gu, Daejeon 305-353, Republic of Korea*

Correspondence should be addressed to Kihwan Kim; [kihwankim@kaeri.re.kr](mailto:kihwankim@kaeri.re.kr)

Received 28 October 2013; Accepted 5 March 2014; Published 1 April 2014

Academic Editor: Junli Gou

Copyright © 2014 Kihwan Kim et al. This is an open access article distributed under the Creative Commons Attribution License, which permits unrestricted use, distribution, and reproduction in any medium, provided the original work is properly cited.

During the reflood phase of a large-break loss-of-coolant accident (LBLOCA) in a pressurized-water reactor (PWR), the fuel rods can be ballooned or rearranged owing to an increase in the temperature and internal pressure of the fuel rods. In this study, an experimental study was performed to understand the thermal behavior and effect of the ballooned region on the coolability using a  $2 \times 2$  rod bundle test facility. The electrically heated rod bundle was used and the ballooning shape of the rods was simulated by superimposing hollow sleeves, which have a 90% blockage ratio. Forced reflood tests were performed to examine the transient two-phase heat transfer behavior for different reflood rates and rod powers. The droplet behaviors were also investigated by measuring the velocity and size of droplets near the blockage region. The results showed that the heat transfer was enhanced in the downstream of the blockage region, owing to the reduced flow area of the subchannel, intensification of turbulence, and deposition of the droplet.

## 1. Introduction

The effect of the ballooned fuel rods on the coolability has been an important issue since the 1980s. The ballooned fuel rods cause a flow blockage of subchannel and flow redistribution near the blockage region. As a result, the transient heat transfer behavior of the ballooned fuel rods is entirely different from the normal ones. Therefore, many experimental studies have been conducted over the past several decades. The main experimental programs can be summarized as the FEBA [1], SEFLEX [2], THETIS [3, 4], ACHILLES [5], CEGB [6], and FLECHT-SEASET programs [7]. More detailed reviews of the programs were given by Grandjean [8]. In addition, JAERI conducted forced reflood tests with a 60% blockage ratio using the Slab Core Test Facility (SCTF) for modeling and verification of safety code [9]. The previous studies conducted forced or gravity reflood tests for various test conditions to examine the thermal behavior of the blockage region and to determine an upper limit of the blockage coolability with respect to the blockage geometry and configurations. They concluded that the coolability at the blockage region greatly depends on the blockage characteristics (blockage ratio, maximum blockage

length, blockage shape, and blockage configuration) and the coolant conditions (flow rate, system pressure, and inlet temperature). However, the effect of fuel relocation in the process of the ballooning of the fuel rods was not considered in their study.

Recently, an experimental program was launched by the Korea Atomic Energy Research Institute (KAERI) in 2011 to understand the related physical phenomena and evaluate the coolability of the ballooned fuel rods considering the fuel relocation. The experimental program consists of two large group tests. The first group test is intended to understand the heat transfer phenomena and to examine the effect of the blockage characteristics on the coolability in a modeled  $2 \times 2$  subchannel. The second experiment, after the first group test, will be performed in a more elaborate  $5 \times 5$  facility considering the blockage and fuel relocation.

As mentioned earlier, more specifically, the main objective of the first group tests is to identify the effect of the blockage ratio and length on the heat transfer behavior. Therefore, four different types of blockage simulators (blockage ratio: 62% or 90%, maximum blockage length: 80 mm or 160 mm) are designed to simulate the ballooned shape of the fuel rods. Single-phase steam flow and forced reflood tests were

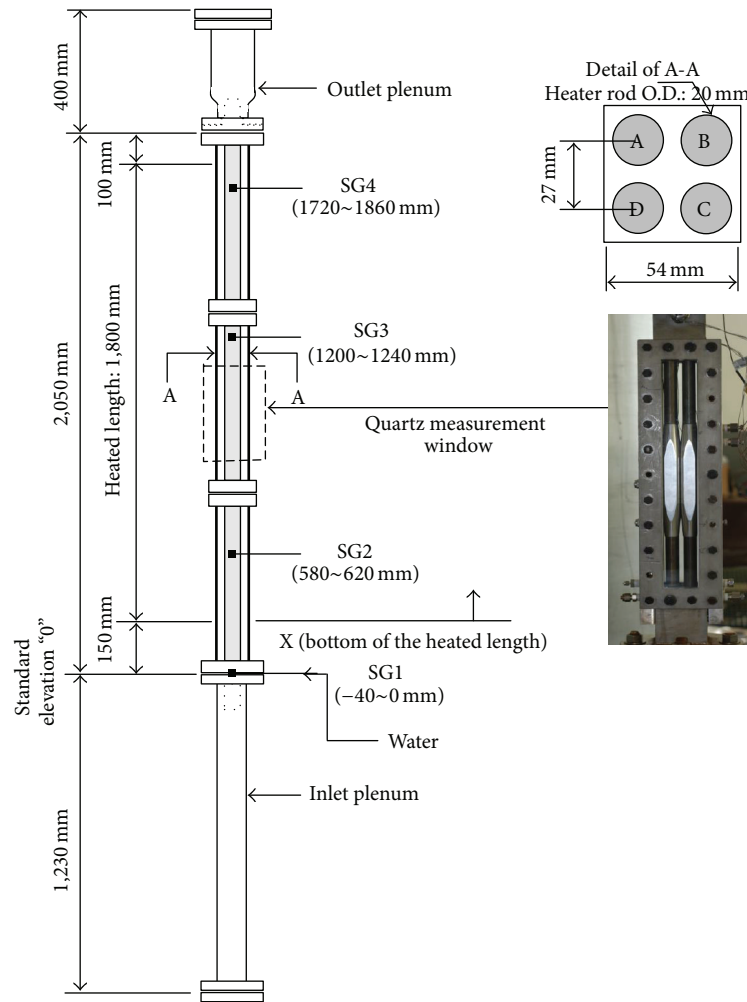


FIGURE 1: Schematic diagram of the test section in the  $2 \times 2$  test facility.

performed and the results were compared with the reference test (nonblockage) results. However, in the present study, forced reflood test results for the blockage simulator with a 90% blockage ratio and short maximum blockage length will be presented. The remaining tests for other blockage simulators will be conducted later. A single-phase steam flow test, which was intended to investigate the influence of the blockage on the convective heat transfer, was already conducted by the authors of [10]. The reflood rate was chosen as the main parameter for the forced reflood tests since it can significantly affect the coolability, especially for low reflood rates. Therefore, the forced reflood tests were performed at different reflood rates, between 1.0 and 3.5 cm/s. In addition, the tests were also carried out for two different rod powers, 1.0 kW/m and 1.5 kW/m. The axial temperature profiles of the heater rods were measured, and the local heat transfer coefficients were calculated. Moreover, the velocity and size of the droplets at the upstream and downstream regions of the blockage simulator were measured to investigate quantitatively the droplet behavior which plays a significant role in the coolability. The results were carefully discussed based on the temperature profiles of the heater rods and the droplet behavior.

## 2. Experimental Test Facility

The experiments were performed in a  $2 \times 2$  rod bundle test facility in which the fuel rods were simulated by electrical heaters made of Nichrome. The heaters are embedded in BN + MgO insulators and enclosed in a 1.65 mm Inconel 600 cladding layer. The total heated length of the heater rods is 1800 mm, and uniform electrical power in both the axial and radial directions is supplied to the heater rods. The heater rods are 20 mm in diameter and arranged in a square array with a 27 mm pitch, as shown in Figure 1. This geometry is about twice as large as the subchannel of a conventional PWR reactor. Four spacer grids without mixing vanes are assembled to the test section with a 580 mm interval to support the heater rods. A quartz measurement window is installed at the center region of the test section to measure the droplets using a high-speed camera. The droplet images were analyzed with commercial software (VisiSize) from Oxford Laser Ltd. to extract the droplet size and velocity [11]. The VisiSize software has 3.2% uncertainty for 0.1 mm droplet diameter and 0.03% uncertainty for 2 mm [12]. The subcooled water from the coolant storage tank is injected into the bottom of the test section.

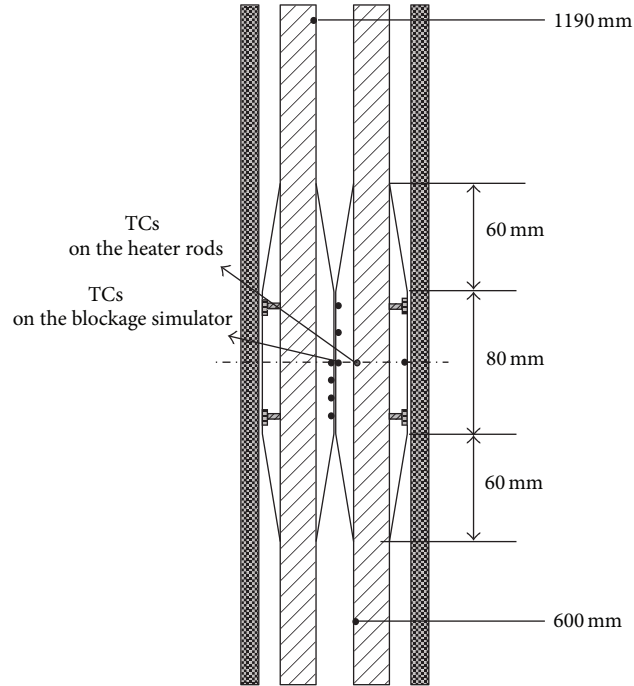


FIGURE 2: Schematic diagram and instrumentation of the 90% blockage simulator.

The ballooning of the fuel rods was simulated by superimposing the blockage simulators onto the heater rods. The blockage simulators were made of Inconel 600, which is the same material as the heater rod cladding. A schematic diagram is shown in Figure 2. The tapered hollow sleeves were used to simulate the shape of the ballooning. The total length of the blockage simulator is 200 mm, among which 80 mm is the maximum blockage length and 60 mm is the inlet/outlet taper lengths. The maximum blockage ratio in the center region is 90%. The inner diameter of the blockage simulator is the same as the outer diameter of the heater rod. The blockage simulators were fixed on the heater rods using grub screws. It should be noted that the blockage simulators have no bypass flow region, owing to the inherent geometrical restriction of the  $2 \times 2$  test facility. The blockage simulators were placed between 735 mm and 935 mm from the bottom of the heated length. In this region, it is thought that the effect of the second and third spacer grids (SG2 and SG3) is diminished.

To measure the temperature on the heater rods, each rod was instrumented with 10 thermocouples (TCs), which were mounted directly on the outer surface of the Inconel cladding. Previous experimental programs [7] have not provided any temperature profiles along the elevation in the blockage region. However, in this study, eight additional TCs were embedded on the outer surface of the blockage simulator along the axial direction to monitor the transient temperature profiles directly, as shown in Figures 2 and 4. The axial locations and radial locations of all TCs are shown in Figures 3 and 4. The steam flow rate, steam inlet temperature, and steam inlet pressure were measured by a vortex flow meter, a K-type thermocouple, and a pressure transmitter, respectively. The uncertainties of the measurement instruments are 1.00% of span,  $\pm 1.1^\circ\text{C}$ , and 0.065%, respectively.

TABLE 1: Main test conditions of the non-blockage tests.

$V_r$ (cm/s)/Test conditions	$V_r$ (cm/s)	$P_{\text{sys}}$ (kPa)	$\Delta T_{\text{sub}}$ ( $^\circ\text{C}$ )	$Q$ (kW/m)
1.0	1.03	101.5	61.0	1.00
	1.03	101.5	47.8	1.50
1.5	1.55	101.4	50.3	1.00
	1.53	101.4	49.2	1.49
2.0	2.06	101.4	48.4	0.99
	2.03	101.4	46.1	1.50
2.5	2.55	101.4	47.5	1.01
	2.49	101.5	47.4	1.51
3.5	3.43	101.4	46.7	0.97
	3.47	101.5	49.8	1.50

### 3. Test Results

For a parametric study, forced reflood tests were performed for various reflood velocities between 1.0 and 3.5 cm/s. In addition, two different rod powers were also considered: 1.0 kW/m and 1.5 kW/m. The main test parameters for the nonblockage and blockage tests are summarized in Tables 1 and 2, respectively. The temperature profiles of the heater rods and blockage simulator were measured simultaneously along the elevation, and the droplet measurements were also performed for three blockage tests as shown in Table 3.

The transient temperature profiles for different reflood rates and rod powers are compared with the nonblockage test results in Figures 5 and 6. The hollow and solid symbols represent the temperatures of the nonblocked and blocked test results, respectively. Figure 5 shows the temperature

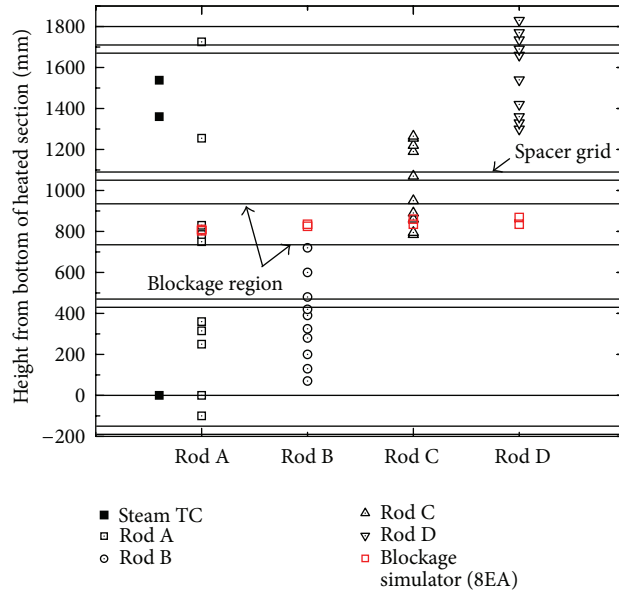


FIGURE 3: Axial TC locations of the test section.

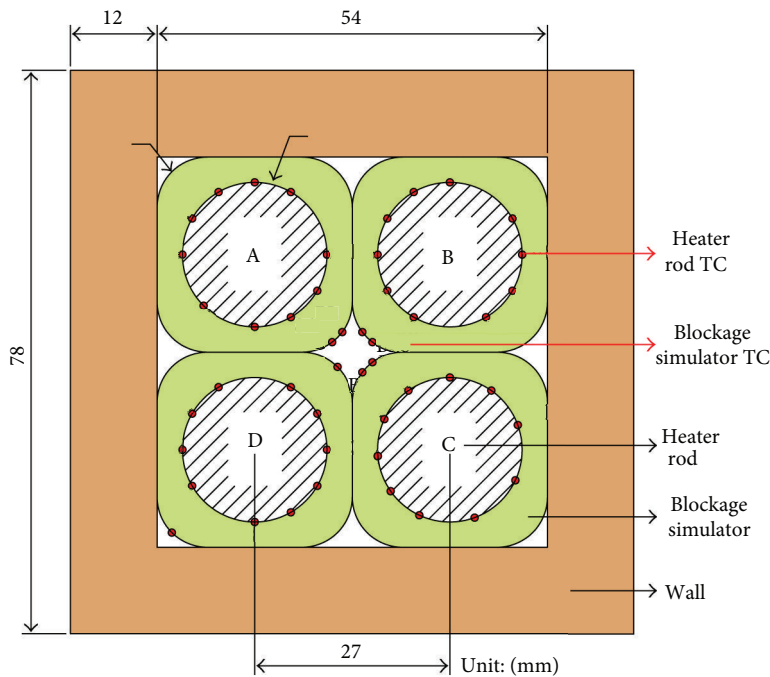


FIGURE 4: Radial TC locations of the test section.

profiles at the upstream region. When the rod power is low, there are almost no differences for all reflood rates. This may be attributed to the small amount of steam and droplets generated in the low rod power. However, when the rod power is high and the reflood rates are lower than 2.5 cm/s, the coolability of the blockage test is reduced in proportion to the reflood rate. Thus, the coolability is important at the low reflood rate, and this tendency is consistent with the previous experiments [8]. To the contrary, the coolability of the blockage tests is significantly enhanced in the downstream region, as shown in Figure 6. The tendency of the

temperature profiles at the upstream and downstream regions can be explained with the results of the droplet measurement. For three reflood rates ( $V_r = 1.0, 2.5, \text{ and } 3.5 \text{ cm/s}$ ), the droplet size and velocity were measured at the upstream and downstream regions in the early stage of the reflood phase. The correlations between the droplet velocity and number of droplets are shown in Figure 7. In addition, Table 3 shows the averaged values of the velocity and Sauter mean diameter of the droplets. Compared to the upstream, the downstream shows a narrow distribution of the droplet size, though not shown here, but the droplet velocities are in a wide range, as

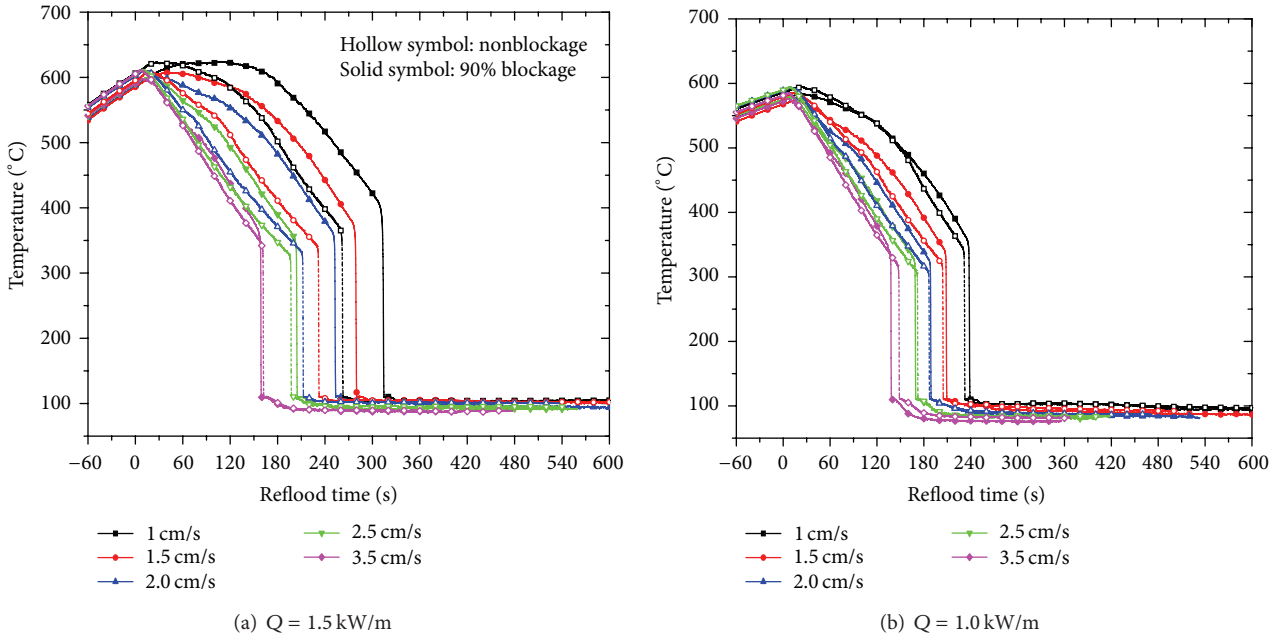


FIGURE 5: Comparison of the temperature profiles at the upstream region (600 mm).

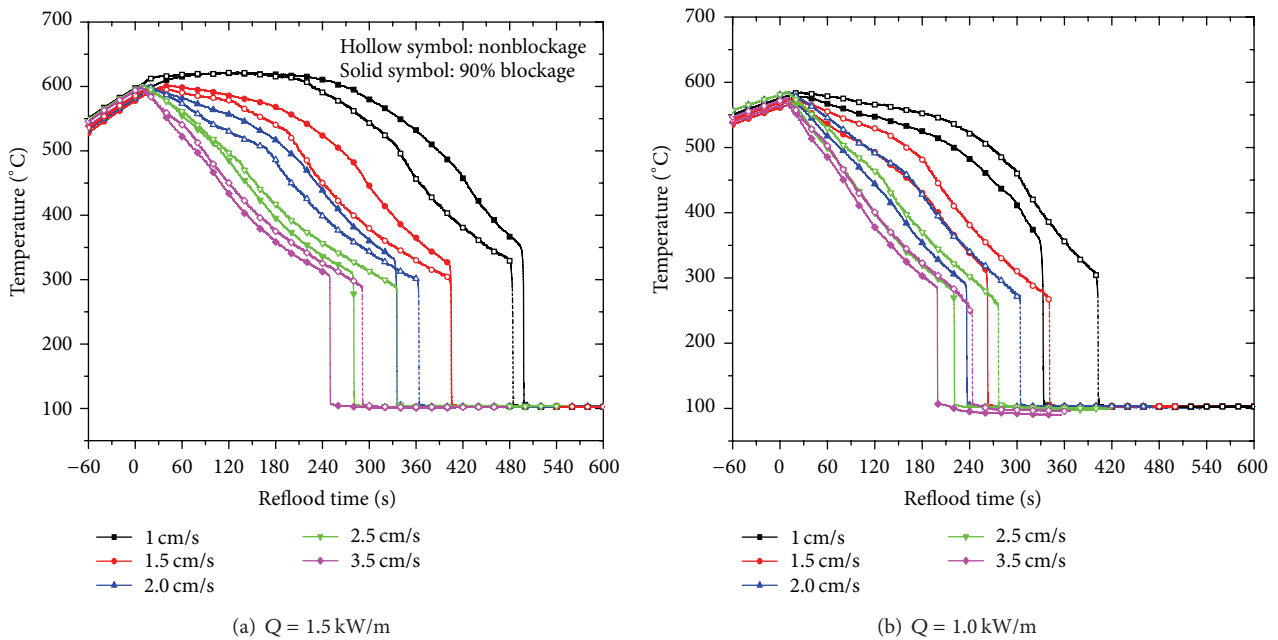


FIGURE 6: Comparison of the temperature profiles at the downstream region (1190 mm).

shown in Figure 7. This means that the turbulence intensities of the steam flow are highly increased in the downstream. It was also noted that the droplet velocity at the downstream is faster than that of the upstream region, as shown in Table 3, since the inertia of the droplet is high enough that the droplets do not follow the reduced steam velocity faithfully in the downstream region. Figure 8 shows droplet images taken at nearly the same time in the early reflood phase when the reflow rate and rod power are 2.5 cm/s and 1.5 kW/m.

In the ballooned region, the steam flow is accelerated and becomes more turbulent, which results in droplet breakup due to hydrodynamic instability. We can see in Figure 7 that the droplet size is smaller in the downstream region. The secondary steam flows in the downstream cause the liquid droplets to collide strongly and frequently with the surfaces of the blockage or heater rods. As a result, the convective heat transfer and rewetting of the droplets on the heat rods in the downstream become more enhanced than the droplet impact

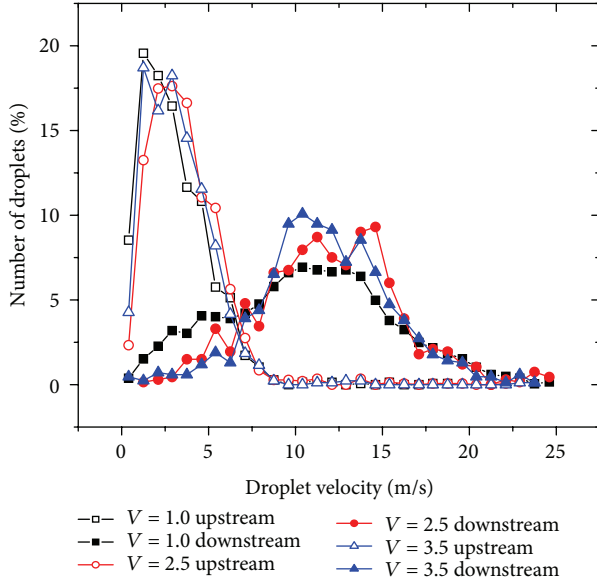


FIGURE 7: Velocity distributions of droplets for various reflow rates when  $Q = 1.5 \text{ kW/m}$ .

TABLE 2: Main test conditions of the blockage tests.

$V_r$ (cm/s)/Test conditions	$V_r$ (cm/s)	$P_{sys}$ (kPa)	$\Delta T_{sub}$ ( $^{\circ}\text{C}$ )	$Q$ (kW/m)
1.0	1.03	101.5	57.0	1.00
	1.04	101.3	52.0	1.50
1.5	1.55	101.3	52.1	1.01
	1.53	101.4	52.7	1.50
2.0	2.06	101.4	51.0	1.01
	2.04	101.3	53.1	1.51
2.5	2.56	101.4	50.2	1.00
	2.56	101.3	50.6	1.50
3.5	3.43	101.4	54.3	1.01
	3.43	101.3	51.0	1.51

TABLE 3: Averages of the droplet velocity and size near the blockage region.

$V_r$ (cm/s)	Upstream (720 mm)		Downstream (950 mm)	
	Velocity (m/s)	Sauter mean ( $\mu\text{m}$ )	Velocity (m/s)	Sauter mean ( $\mu\text{m}$ )
1.0	3.0	1204.5	10.7	538.4
2.5	3.6	1006.9	12.0	427.4
3.5	3.3	1120.8	11.7	636.8

heat transfer in the upstream. This means that the droplets behind the blockage simulator play a significant role in the coolability enhancement.

To understand the quenching phenomena in the internal region of the blockage, the transient temperature profiles on the outer surface of the blockage simulator were measured along the elevation. The main finding is the rewetting phenomena in the internal region for various reflow rates. As

shown in Figure 9, it is obvious that the cooling occurred earlier in the downstream region for all reflow rates. However, it is interesting to note that the temperature profiles of the center region show large fluctuations when the reflow rates are higher than 2.5 cm/s. When increasing the reflow rates, the droplet velocity is more accelerated and the size of the droplets at the downstream region becomes small as shown in Table 3. This means that most of the droplets fragment into smaller ones by passing through the blockage region. Therefore, the drastically decreased temperature at 830 mm may be explained by the droplet breakup and rewetting phenomena in the blockage region.

Figure 10 shows the heat transfer coefficients calculated at the outer surface of the heater rods. The heat transfer coefficients in the downstream are always higher than those in the upstream. For each experimental case, the quenching time, at which  $\partial T^2 / \partial t^2$  is the most negative value, is given in Table 4. The quenching time in the downstream is generally earlier than that in the upstream. It should be noted that the subchannel size of the present facility is twice as large as that of a typical PWR, and thus the applied power may not be sufficient for a large quantity of droplets. The number of droplets is not enormous, and thus in the case of 1.0 kW/m a strong turbulent stream flow would be a dominant cooling factor because the blockage ratio is 90%. The number of droplets increases with the power. Therefore, for 1.5 kW/m, although the number of droplets may not be enormous, most droplets affect the upstream cooling. Steam flow speed tends to increase with the reflow rate. For the 1.5 kW/m power and low reflow rate, the droplets evaporate, if any, while they pass through the blockage. As a result, not many droplets could appear in the downstream. However, as the reflow rate increases further, a large quantity of droplets is generated and the steam velocity increases, thus many droplets can appear in the downstream. In this case, the downstream is cooled, not only by the turbulent flow but also by the droplets, leading to the early quenching of the downstream.

#### 4. Conclusions

In this study, forced reflow tests were carried out for different reflow rates and rod power to understand the heat transfer behavior. The nonblockage and blockage tests were performed to investigate the effect of the ballooned fuel rod on the coolability in a  $2 \times 2$  rod bundle test facility. The ballooned shape of the fuel rods was simulated using the blockage simulator with a 90% blockage ratio. Thermocouples were directly mounted on the outer surface of the blockage simulator along the elevation to understand the local quenching phenomena in the blockage region. All transient temperature profiles of the heater rod and blockage simulator were simultaneously measured, and the heat transfer coefficients and quench time were calculated to evaluate the overall coolability of the blockage region. In addition, the velocities and sizes of the droplets near the blockage region were also measured to scrutinize the droplet effect on the quench phenomena. The results show that the coolability in the blockage region highly depends on the combined

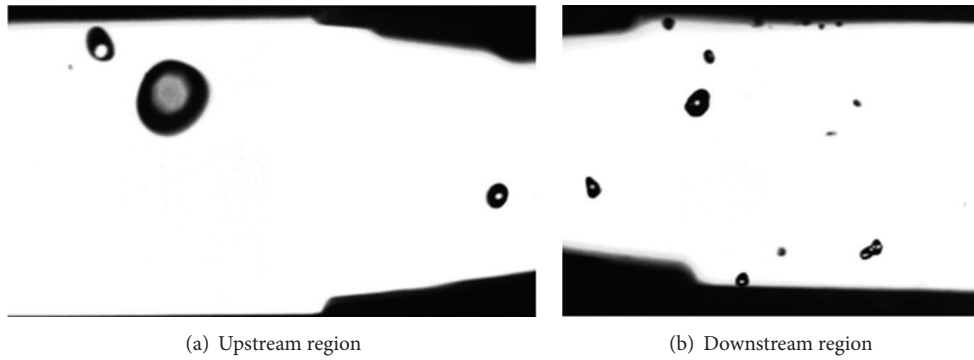


FIGURE 8: Droplet images near the blockage region.

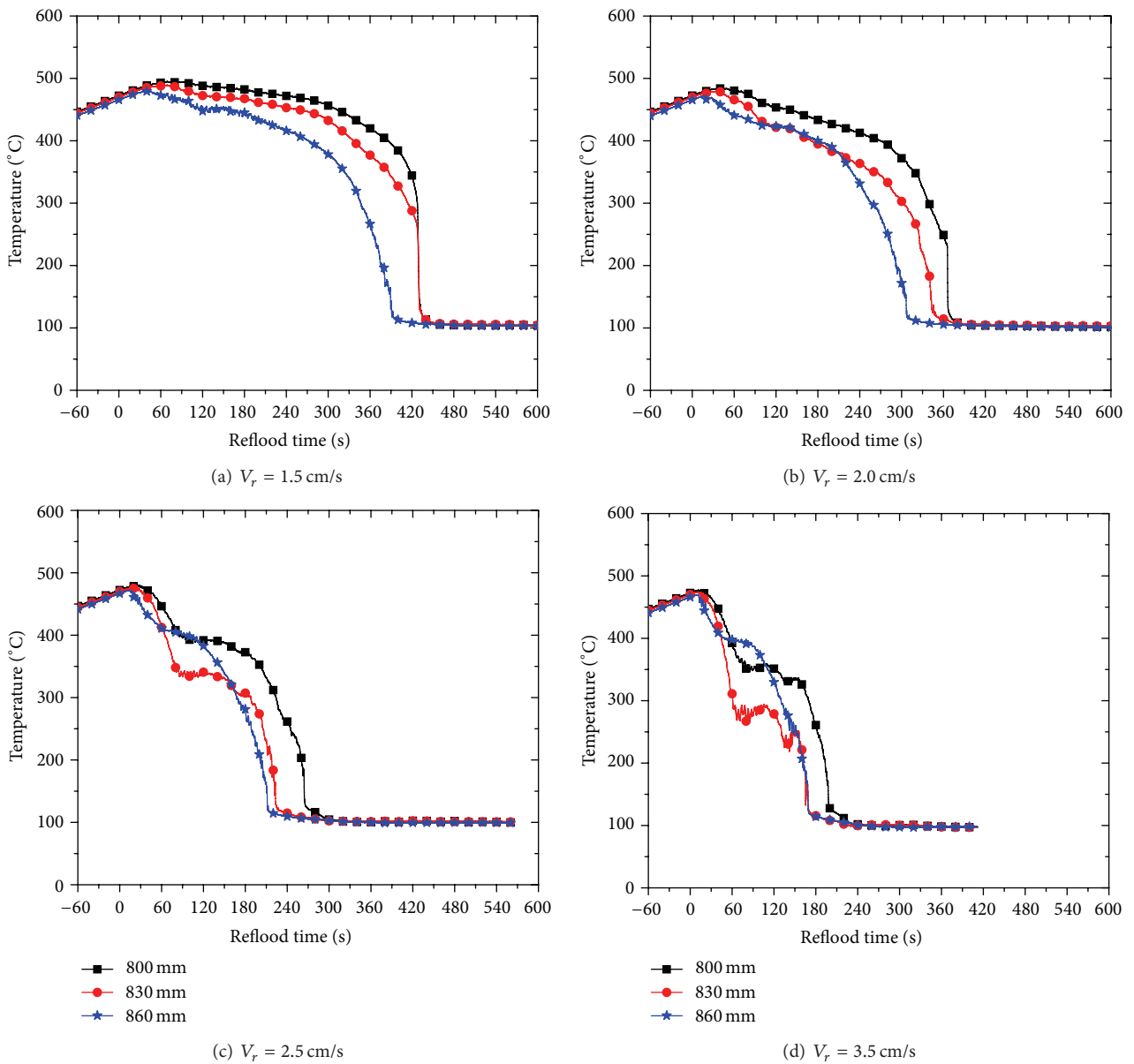


FIGURE 9: Temperature profiles in the blockage internal region for  $Q = 1.5$  kW/m.

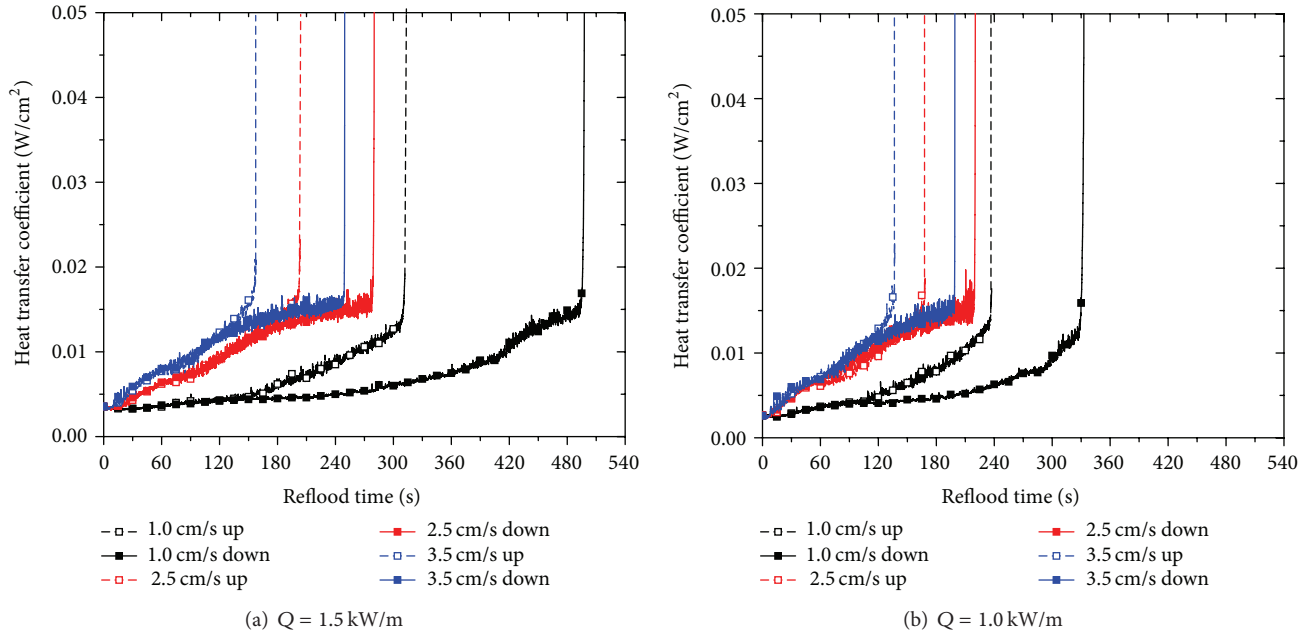


FIGURE 10: Comparison of the heat transfer coefficients distributions.

TABLE 4: Quench time at the upstream and downstream region of blockage.

$V_r$ (cm/s)	Test	Upstream (600 mm)		Downstream (1190 mm)	
		1.0 kW/m	1.5 kW/m	1.0 kW/m	1.5 kW/m
1.0	Non-blockage	231.6	261.5	401.9	483.4
	90% blockage	237.7	313.4	332.7	497.0
1.5	Non-blockage	203.9	231.4	340.5	404.4
	90% blockage	208.3	278.7	262.2	404.6
2.0	Non-blockage	186.3	211.6	303.5	363.1
	90% blockage	188.3	252.2	235.7	334.7
2.5	Non-blockage	171.5	196.5	276.2	335.4
	90% blockage	168.6	203.7	219.9	279.5
3.5	Non-blockage	147.7	161.3	243.0	290.7
	90% blockage	137.5	158.3	198.8	249.2

effect of the fluid flow distribution and droplet behavior. The coolability in the downstream of the blockage region is significantly enhanced since the turbulence intensities are increased owing to the sudden change of the flow passage area and the rewetting of the droplet on the heater rod in the downstream region. In the internal region of the blockage, the droplets were accelerated owing to the reduction of the flow area and fragmented into smaller ones while passing through the blockage region. As a conclusion, the convective heat transfer enhancement owing to the turbulent flow and the cooling effect by liquid droplets are the main factors for the coolability improvement in the downstream of the blockage region. The main findings that have been obtained in this study are valid for the blockage configurations without a coolant bypass. For this reason, additional tests are scheduled to be performed in a  $5 \times 5$  rod bundle test facility with a coolant bypass.

## Conflict of Interests

The authors declare that there is no conflict of interests regarding the publication of this paper.

## Acknowledgment

This work was supported by the National Research Foundation of Korea (NRF) Grant funded by the Korean Government (MSIP) (no. 2012M2A8A4026028).

## References

- [1] P. Ihle and K. Rust, "FEBA-flooding experiments with blocked arrays-influence of blockage shape," in *Proceedings of the ANS-Transactions European Nuclear Conference*, vol. 31, p. 398, 400, May 1979.

- [2] P. Ihle and K. Rust, "SEFLEX-fuel rod simulator effects in flooding experiments. Part 1: evaluation report," KfK 4024, 1986.
- [3] K. G. Pearson, C. A. Cooper, D. Jowitt, and J. H. Kinneir, "Reflooding experiments on a 49-rod cluster containing a long 90% blockage," AEEW ER 1591, 1983.
- [4] K. G. Pearson, C. A. Cooper, and D. Jowitt, "The THETIS 80% blocked cluster experiment. Part 4: gravity reflood experiments," AEEW ER 1766, 1984.
- [5] M. K. Denham, D. Jowitt, and K. G. Pearson, "ACHILLES unballooned cluster experiments. Part 1: description of the ACHILLES Rig, test section and experimental procedures," AEEW R 2336, 1989.
- [6] S. A. Fairbairn and B. D. G. Piggott, "Flow and heat transfer in PWR rod bundles in the presence of flow blockage due to clad ballooning experimental data," Report. Part 2 CEGB-TPRD/B/0511/N84, 1984.
- [7] L. E. Hochreiter, "FLECHT-SEASET Program," Final Report NUREG/CR-4167, EPRI NP-4112, WCAP-10926, 1985.
- [8] C. Grandjean, "Coolability of blocked regions in a rod bundle after ballooning under LOCA conditions: main findings from a review of past experimental programmes," *Nuclear Engineering and Design*, vol. 237, no. 15–17, pp. 1872–1886, 2007.
- [9] Y. Sudo and M. Osakabe, "Effects of partial blockage on core heat transfer in forced-feed reflood tests," *Journal of Nuclear Science and Technology*, vol. 20, no. 4, pp. 322–332, 1983.
- [10] K. Kim, B. J. Kim, Y. J. Youn, H. S. Choi, and S. K. Moon, "Convective heat transfer of a blocked region in ballooned 2×2 rod bundle under a single-phase flow," in *Proceedings of the 6th Korea-China Workshop on Nuclear Reactor Thermal-Hydraulics (WORTH-6 '13)*, Busan, Republic of Korea, 2013.
- [11] *VisiSize Software Operation Manual for VisiSize 5*, Oxford Lasers Imaging Division, 2010.
- [12] D. R. Todd, *Characterization of the VisiSizer Particle/Droplet Sizing System [M.S. thesis]*, State University, 1999.

## Research Article

# Subchannel Analysis of Wire Wrapped SCWR Assembly

Jianqiang Shan, Henan Wang, Wei Liu, Linxing Song, Xuanxiang Chen, and Yang Jiang

*Xi'an Jiaotong University, Xi'an, Shanxi 710049, China*

Correspondence should be addressed to Jianqiang Shan; jqshan@mail.xjtu.edu.cn

Received 10 October 2013; Accepted 13 January 2014; Published 23 February 2014

Academic Editor: Liangzhi Cao

Copyright © 2014 Jianqiang Shan et al. This is an open access article distributed under the Creative Commons Attribution License, which permits unrestricted use, distribution, and reproduction in any medium, provided the original work is properly cited.

Application of wire wrap spacers in SCWR can reduce pressure drop and obtain better mixing capability. As a consequence, the required coolant pumping power is decreased and the coolant temperature profile inside the fuel bundle is flattened which will obviously decrease the peak cladding temperature. The distributed resistance model for wire wrap was developed and implemented in ATHAS subchannel analysis code. The HPLWR wire wrapped assembly was analyzed. The results show that: (1) the assembly with wire wrap can obtain a more uniform coolant temperature profile than the grid spaced assembly, which will result in a lower peak cladding temperature; (2) the pressure drop in a wire wrapped assembly is less than that in a grid spaced assembly, which can reduce the operating power of pump effectively; (3) the wire wrap pitch has significant effect on the flow in the assembly. Smaller  $H_{\text{wire}}/D_{\text{rod}}$  will result in stronger cross flow a more uniform coolant temperature profile, and also a higher pressure drop.

## 1. Introduction

The supercritical water-cooled reactor (SCWR) is essentially a water reactor operating above the thermodynamic critical point of water ( $P_c = 22.064$  MPa). It is considered as one of the most promising Generation IV reactors because of its simplicity, high thermal efficiency, and nearly fifty years of industrial experience from thermal-power stations with a SCW cycle [1]. Evolving from the existing designs, there are currently two types of SCWR concepts [2]: (a) a large reactor pressure vessel containing the reactor core (fuelled) heat source, analogous to conventional PWRs and BWRs, and (b) distributed pressure tubes or channels containing fuel bundles, analogous to conventional CANDU and RBMK nuclear reactors. The arrangement of separated moderator (moderator box in pressure vessel type and heavy water moderator in calandria in pressure tube type) is applied in each design, due to the sharp change in the thermal properties of coolant near the pseudo-critical point.

To obtain a small water volume fraction in core, tight lattices are necessary. Wire wrap spacers, an alternative to grid spacers, have been used extensively in LMFBR [3] and tight-lattice high-conversion cores [4], mainly due to their advantageous pressure drop and better mixing capability. As a consequence, the required coolant pumping power is

decreased and the coolant temperature profile inside the fuel bundle is flattened which will obviously decrease the peak cladding temperature. The other potential advantage of wire wrap spacer is that it can improve the heat transfer at the rod gap where heat transfer deterioration occurs in SCWR assembly. For SCWR design, wire wrapped assembly has been selected in both three-pass HPLWR [5] and US SCWR [6].

The influence of wire wrap under supercritical pressure conditions should be well studied. Himmel et al. [7] studied the mixing coefficients for a subchannel flow through a HPLWR fuel assembly with 40 wire wrapped fuel pins in a square arrangement, and their analyses were concentrated on a section of 3 subchannels between the assembly box and the inner moderator box walls. Laurien et al. [8] carried out the heat transfer experiments with a 10 mm rod inside a square vertical channel with a wire wrapped helically around it. The results showed that, based on the comparison with an identical channel without the helical wrapped wire, the wire spacer did not enhance the heat transfer significantly under normal heat transfer conditions but helped improve the heat transfer in the pseudo-critical region and shift the onset of the deterioration to downstream. Chandra et al. [9] analyzed the wire wrap effect with CFD method. The results showed that the adiabatic helical wire wrap around the inner heated cylinder of the annulus prevented the heat transfer

deterioration from occurring in the considered test case, even at very high heat fluxes. This was related to the enhanced production of the turbulent kinetic energy by the presence of helical wire wrap, which increased the turbulent mixing effect and consequently the heat transfer and finally reduced the wall temperature.

To better understand the behavior of the coolant and cladding under the influence of wire wrap in the whole assembly, subchannel analysis is an effective and simpler method. The present paper developed a subchannel code for wire wrapped SCWR bundle based on the ATHAS code.

## 2. Model Description

*2.1. Basic Conservation Equations of ATHAS.* The basic equations of the mathematical model [10] are derived by applying the general equations of continuity, energy, and momentum to a subchannel  $i$  control volume  $j$ . The equations are as follows.

*Mass.* Consider

$$\bar{A} \frac{\partial}{\partial t} \langle \langle \rho \rangle \rangle_V + \frac{\partial}{\partial Z} (\langle \rho u \rangle_A A) + \sum_{k=1}^{n_k} (\langle \rho V_k \rangle_S S)_k = 0, \quad (1)$$

where the density, the axial mass flux, and the lateral mass flux are defined by

$$\begin{aligned} \langle \langle \rho \rangle \rangle_V &= \frac{1}{V} \int_V \rho dV, & \langle \rho u \rangle_A &= \frac{1}{A} \int_A \rho u dA, \\ \langle \rho v \rangle_A &= \frac{1}{A} \int_A \rho v dA. \end{aligned} \quad (2)$$

The first term is the time rate of change of mass per unit axial length and the second is spatial variation in axial mass flux per unit length. The last term is the sum on all gap connections of the lateral mass flux per unit length which is the cross flow associated with subchannel analysis.

*Energy.* Consider

$$\begin{aligned} &\bar{A} \frac{\partial}{\partial t} \langle \langle \rho h \rangle \rangle_V + \frac{\partial}{\partial Z} \langle \rho h u \rangle_A A + \sum_{k=1}^{n_k} [\langle \rho h V_k \rangle_S S]_k \\ &= \sum_{r=1}^{n_r} [P_r \Phi_j H_r (t_r - t_f)]_r + \sum_{W=1}^{n_W} [L_W H_W (t_W - t_f)]_W \\ &+ \frac{\partial}{\partial Z} A \left\langle k_f \frac{\partial t}{\partial Z} \right\rangle_A - \sum_{k=1}^{n_k} \left[ \frac{S \cdot C_g k_f}{L_c} (t_i - t_j) \right]_k \\ &- \sum_{k=1}^{n_k} [W' (h'_i - h'_j)]_k. \end{aligned} \quad (3)$$

The equation considers the heat transfer from the rod and wall-to-channel (if necessary) to the control volume, the axial fluid heat conduction, the lateral fluid heat conduction

through the gap between two channels, and turbulent energy input.

*Axial Momentum.* Consider

$$\begin{aligned} &\bar{A} \frac{\partial}{\partial t} \langle \langle \rho u \rangle \rangle_V + \frac{\partial}{\partial Z} \langle \rho u^2 \rangle_A A + \sum_{k=1}^{n_k} [\langle \rho V_k u \rangle_S S]_k \\ &= -\bar{A} \frac{\partial}{\partial Z} \langle p \rangle_A - \frac{1}{2} \left( \frac{f}{D_e} + \frac{C}{\Delta Z} \right) \langle \rho u^2 \rangle_A A \\ &- g \bar{A} \langle \langle \rho \rangle \rangle_V \cos \theta - C_T \sum_{k=1}^{n_k} [W' (u'_t - u'_f)]_k. \end{aligned} \quad (4)$$

The first term at the left side is the time rate of change of momentum per unit axial length and the second and third are the spatial variation in axial momentum per unit length. The four terms at right side are the total pressure force on the control volume, axial drag force, the gravity force, and the force due to turbulent mixing, respectively.

*Lateral Momentum.* Consider

$$\begin{aligned} &C_s \left\{ \sum_{k=1}^{n_k} \left[ \langle \rho V_k \rangle_S \frac{S}{l} \cos \Delta \beta \right]_{k,j} - \sum_{k=1}^{n_k} \left[ \langle \rho V_k \rangle_S \frac{S}{l} \cos \Delta \beta \right]_{k,i} \right\} \\ &+ \frac{\partial}{\partial t} \langle \langle \rho V_k \rangle \rangle_{V'} S + \frac{\partial}{\partial Z} \langle \rho u V_k \rangle_{A'} S \\ &= \frac{b}{l} (\langle p \rangle_{A,i} - \langle p \rangle_{A,j}) - \frac{1}{2} \frac{S}{l} k_G \langle \rho V_k^2 \rangle_S \\ &- g \langle \langle \rho \rangle \rangle_{V'} S \sin \theta \cos \beta. \end{aligned} \quad (5)$$

The first term at the left side is the net lateral momentum flux and the factor  $C_s$  is included to help account for the imperfect coupling between communicating gaps. The second and third terms at the left side are the time rate of change of lateral momentum per unit lateral length and spatial variation in lateral momentum per unit length. The three terms at the right side are the pressure difference between adjacent channels, the total drag force, and the gravity force, respectively.

The constitutive correlations selected in the analysis are shown as follows based on Shan et al.'s work [10].

Friction coefficient: Blasius correlation [11] for single phase turbulent flow:

$$f = 0.3164 \text{Re}^{-0.25}. \quad (6)$$

Heat transfer coefficient: Bishop correlation (1964) [12] for supercritical water:

$$Nu_x = 0.0069 \text{Re}_x^{0.9} \overline{\text{Pr}}_x^{-0.66} \left( \frac{\rho_w}{\rho_b} \right)_x^{0.43} \left( 1 + 2.4 \frac{D}{x} \right). \quad (7)$$

Turbulent mixing factor: Rowe and Angle correlation [13] in the bundle condition:

$$\beta = 0.021 \cdot \text{Re}^{-0.1}. \quad (8)$$

The selection of Blasius correlation, Bishop correlation (1964), and Rowe and Angle correlation in this paper can obtain relatively high maximum cladding surface temperature and present more conservative estimate.

The code has been validated under supercritical pressure condition [14] and successfully applied in the analysis of pressure vessel and pressure tube type SCWR bundle [10, 15, 16].

**2.2. Wire Wrap Model.** Hydraulic resistance model which was initially proposed by Ninokata et al. [17] is developed to account for the existence of the wire wrap spacer in rod bundle. These models are of “distributed resistance” type and add flow resistance term into the axial and transverse momentum equations as a function of subchannel geometry and flow velocity. The models are general enough to cover a wide range of geometrical parameters, wire position, and flow regime.

In the subchannel formulation, it is a common practice to assume three types of control volume for (1) mass and energy balance, (2) lateral momentum balance, and (3) axial momentum balance. Figure 1 illustrates the typical mass and energy balance control volume (ABCDEF-LMNJPQ) and lateral momentum control volume (SPTUKV-GYZWOX). Note that the control volume for the axial momentum balance is staggered in the axial direction with respect to the energy and mass balance control volume.

In this study, focus is mainly placed on the momentum balance conservation equation, that is, (4) and (5). The second terms at the right side of (4) and (5) represent the momentum exchange between the solid surface and the fluid. These terms, which are the forces exerted on the fluid by the wall, are replaced with the distributed resistance terms. These terms for the rod bundles with wire wraps can be divided into four components, as shown in Figure 2. These forces of  $F_R^L$  and  $F_W^N$  are estimated by correlations depending on the direction of the dominant flow. Each force can be written as

$$F_R^A = R(c) \left( \frac{A_R}{A_w''} \right) \cos \alpha, \quad (9)$$

$$F_W^T = R(c) \left( 1 - \frac{A_R}{A_w''} \right) \cos(\varphi - \alpha),$$

where

$$R(c) = \frac{A_w'' f_M(c)}{8} \rho c |c| \quad (10)$$

$$c^2 = u^2 + v^2.$$

For the predominantly axial flow,

$$F_R^L = \frac{A_w'' f_G}{8} \rho |v| v \left( \frac{D_V''}{S_T} \right)^{0.4} \left( \frac{S_L}{S_T} \right)^{0.6}, \quad (11)$$

$$F_W^N = \frac{A_{WP} f_n}{2} \rho |v_k| v_k,$$

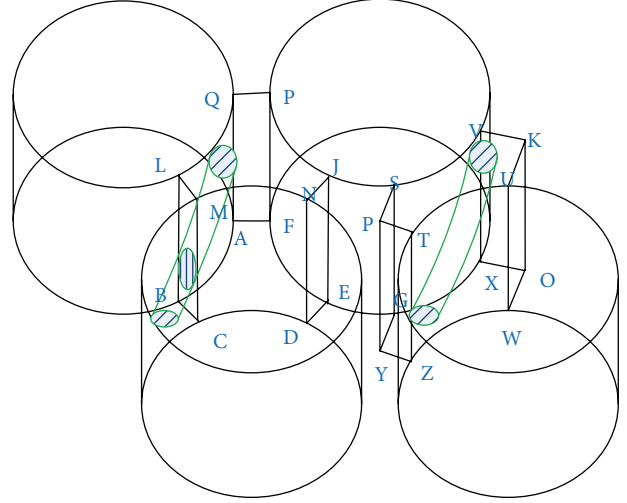


FIGURE 1: Three-dimensional view of a subchannel and a gap with wire wrap.

where  $f_G$  is a friction factor based on the cross flow Reynolds number,  $S_T$  is the rod pitch, and  $S_L$  is the distance between two rods in a transverse row (Figure 3).

The hydraulic resistance per unit volume for the solution of the axial and lateral momentum equations, respectively, can be represented as follows:

$$\frac{1}{2} \left( \frac{f}{D_e} + \frac{C}{\Delta Z} \right) \langle \rho u^2 \rangle_A A = F_R^A + F_W^T \cos \varphi + F_W^N \sin \varphi,$$

$$\frac{1}{2} \frac{S}{l} k_G \langle \rho V_k^2 \rangle_S = F_R^L + F_W^T \sin \varphi - F_W^N \cos \varphi. \quad (12)$$

### 3. Results and Analysis

**3.1. Description of HPLWR Assembly.** The high performance light water reactor (HPLWR) is funded by the European Commission. A specific core design proposed by Schulenberg et al. [18] assumes that the coolant is guided three times through the core during its heat-up from 280°C to 500°C at a system pressure of 25 MPa. Figure 4 illustrates the HPLWR assembly configuration. Fischer et al. [5] gave the detailed design as follows: the assembly cluster is built with nine assemblies and with a gap of 10 mm between the boxes; a total number of 40 fuel rods per assembly with 8 mm outer cladding diameter at a pitch of 9.44 mm are housed within a stainless steel box of 2.5 mm wall thickness and 72.5 mm outer size; a single wire of 1.34 mm diameter is wrapped around each fuel rod with an axial pitch of 200 mm, leaving a tolerance of 0.1 mm between the wire and the fuel rods or the box walls, respectively; the inner moderator box has an outer size of 26.9 mm and a wall thickness of 0.8 mm, which is made from stainless steel as well; the active core height is assumed to be 4.2 m and the total length of the fuel rods is considered as 4.71 m if the fission gas plenum is included. Figure 4 shows the subchannel and fuel identification in a HPLWR fuel bundle. Totally 60 subchannels, 40 rods,

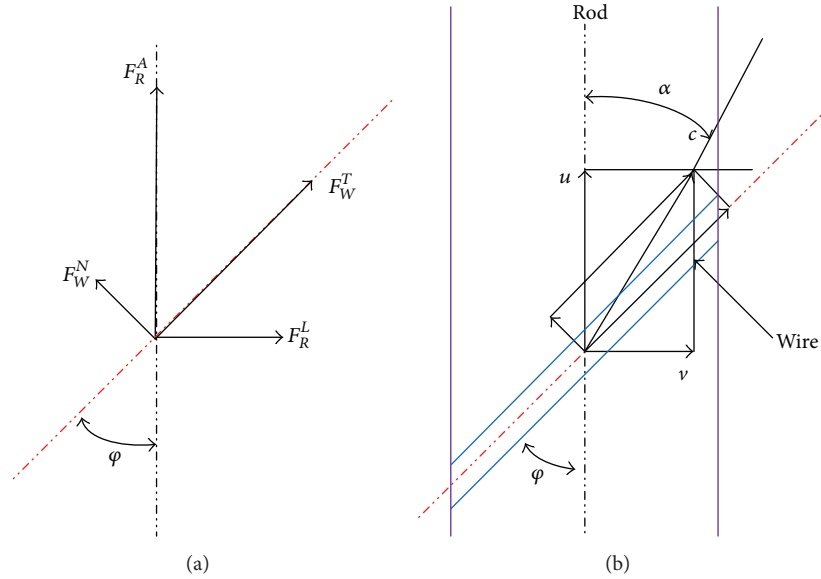


FIGURE 2: Component of the drag forces and velocities in a wire wrapped rod.

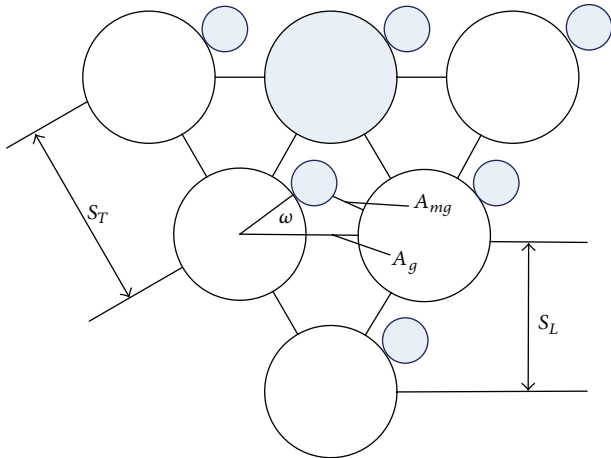


FIGURE 3: Average wire wrap position and gap definition.

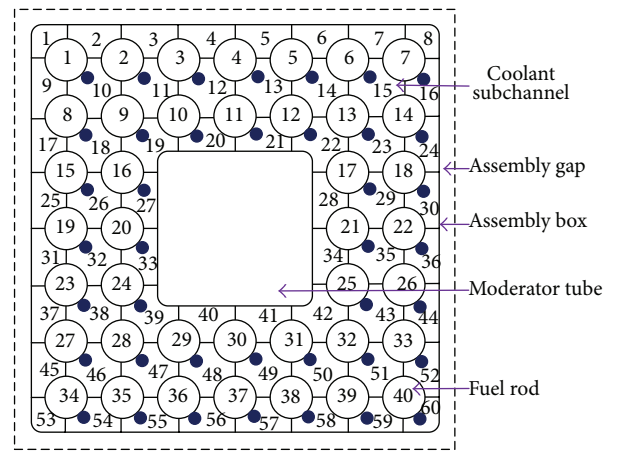


FIGURE 4: Fuel assembly design and subchannel identification.

and 2 conducting walls are defined here. The heat transfer between the subchannels and moderator box/assembly gap is also considered with conducting wall model in the ATHAS code.

Table 1 lists the geometry of the assembly and Table 2 gives the operating parameters. Figure 5 shows the relative axial power distribution, which is the result of neutronic/thermal-hydraulics coupling analysis [19]. The radial power distribution is assumed as uniform.

3.2. Subchannel Analysis Results with Wire Wrapped and Grid Spaced Assemblies. To compare with the behavior of wire wrap in the SCWR assembly, a subchannel analysis of assembly with grid space is also taken. The parameters of grid

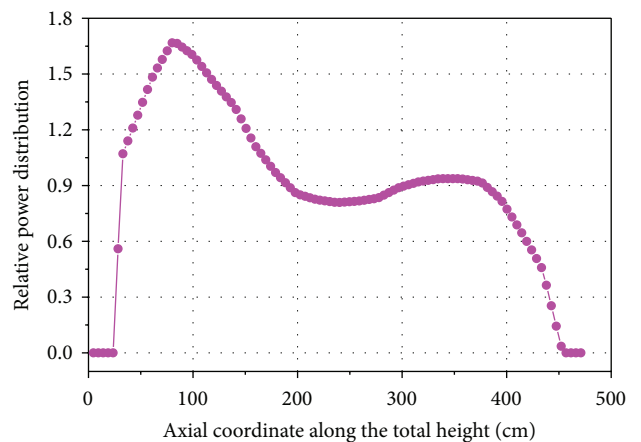


FIGURE 5: Relative power distribution.

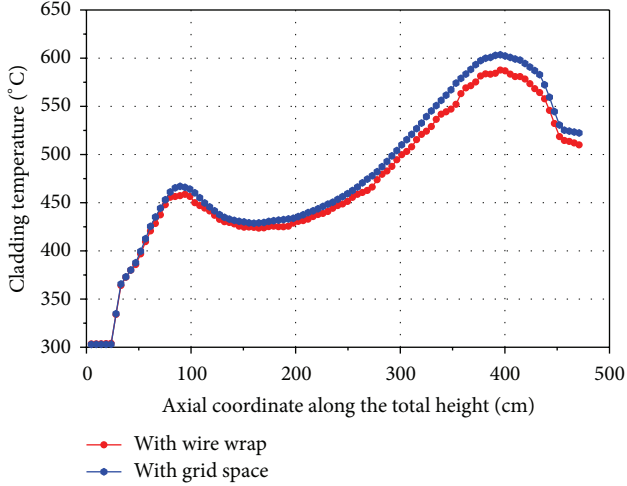


FIGURE 6: Axial cladding temperature profile in the hot channel.

TABLE 1: Fuel assembly geometry parameters.

Parameters	Values
Fuel rod outer diameter	8.00 mm
Fuel rod pitch	9.44 mm
Pitch/diameter ratio ( $P/D$ )	1.18
Active height	4200 cm
Total height	4710 cm
Wire diameter	1.34 mm
Wire pitch	200 mm
Moderator box length	26.9 mm
Moderator box wall thickness	0.8 mm
Outside box length	72.5 mm
Outside box wall thickness	2.5 mm
Gap between fuel rod and box wall	1.43 mm
0.5 gap around one fuel assembly	5.0 mm

spacers are given by Cheng et al. [20]. There are 15 grid spacers along the axial lengths.

The comparison of axial cladding temperature profiles in the hot channel between wire wrapped and grid spaced assemblies is shown in Figure 6. The peak cladding temperature is 587.6°C for wire wrapped assembly and 603.5°C for grid spaced assembly, respectively. The location of peak cladding temperature is at subchannel 43, rod 25, and 3.96 m at axial position. The reason for the temperature difference is that more forced cross flow between subchannels, result in a more uniform coolant temperature profile. Figure 7 shows the coolant temperature profile in the subchannels at the axial position where the peak cladding temperature occurs. The difference of coolant temperature between the hottest and coldest channels is 25.3°C for the wire wrap and 40.2°C for the grid spacer, respectively. Figure 8 shows the pressure drop in the two kinds of assembly; it can be observed that the pressure loss in the wire wrapped assembly is less than that in the grid spaced assembly, which consequently can reduce the required pump power.

TABLE 2: Reactor operation parameters and correlations options in current analysis.

Parameters	Values
Coolant inlet pressure	25 MPa
Coolant inlet temperature	280°C
Coolant exit temperature	500°C
Average heat flux	0.6142 MW·m <sup>-2</sup>
Mass flux	780 kg·m <sup>-2</sup> ·s <sup>-1</sup>

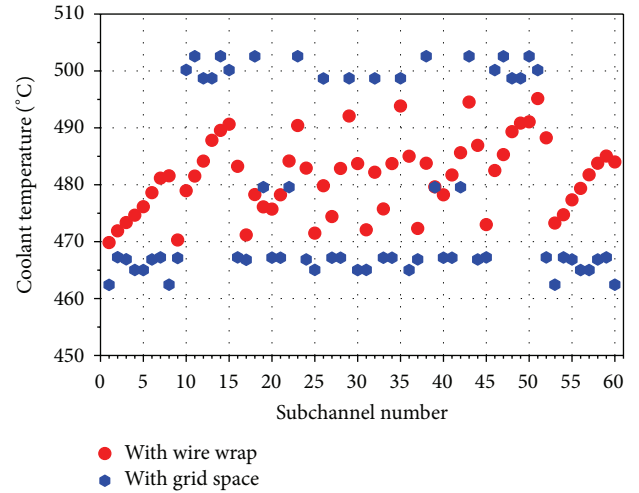


FIGURE 7: Coolant temperature profile at axial position where the peak cladding temperature occurs.

**3.3. Sensitivity Analysis of Wire Wrap Pitch.** Sensitivity analysis of wire wrap pitch was also studied. The pitch is selected according to the criteria determined by Diller [21],  $H_{\text{wire}}/D_{\text{rod}} < 50$ . So four  $H_{\text{wire}}/D_{\text{rod}}$  values have been selected for analysis, which are  $H_{\text{wire}}/D_{\text{rod}} = 20, 30, 40,$  and  $50,$  respectively.

Figure 9 shows the comparison of exit cooling temperature profiles with different  $H_{\text{wire}}/D_{\text{rod}}$  values. It is found that lower  $H_{\text{wire}}/D_{\text{rod}}$  will result in a more uniform profile, since the temperature difference between the hottest and coldest channels is 60.9°C for  $H_{\text{wire}}/D_{\text{rod}} = 50$  and 21.9°C for  $H_{\text{wire}}/D_{\text{rod}} = 20$ . This is understandable because lower  $H_{\text{wire}}/D_{\text{rod}}$  causes more cross flow. However, lower  $H_{\text{wire}}/D_{\text{rod}}$  also leads to a higher pressure drop, as shown in Figure 10. The pressure drop is increased from 51.8 kPa for  $H_{\text{wire}}/D_{\text{rod}} = 50$  to 56.1 kPa for  $H_{\text{wire}}/D_{\text{rod}} = 20$ .

Figure 11 shows the peak cladding temperature comparison with different  $H_{\text{wire}}/D_{\text{rod}}$  values. As we have discussed before, the peak cladding temperature mainly depends on whether the coolant temperature profile in subchannels is uniform or not. Higher  $H_{\text{wire}}/D_{\text{rod}}$  will result in a higher cladding temperature. As for  $H_{\text{wire}}/D_{\text{rod}} = 50$ , the calculated peak cladding temperature is 603.3°C, nearly the same as grid spaced assembly.

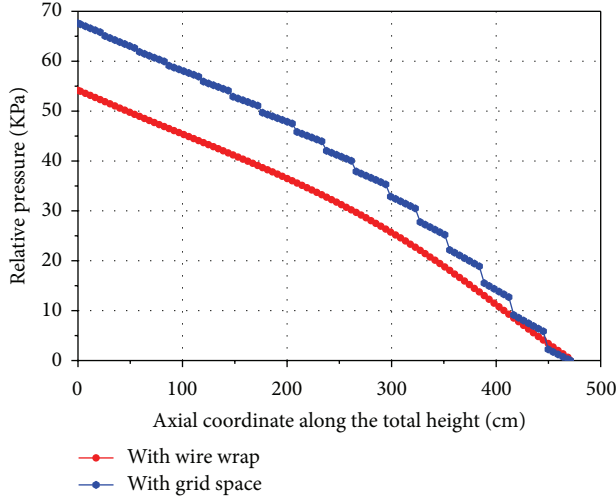
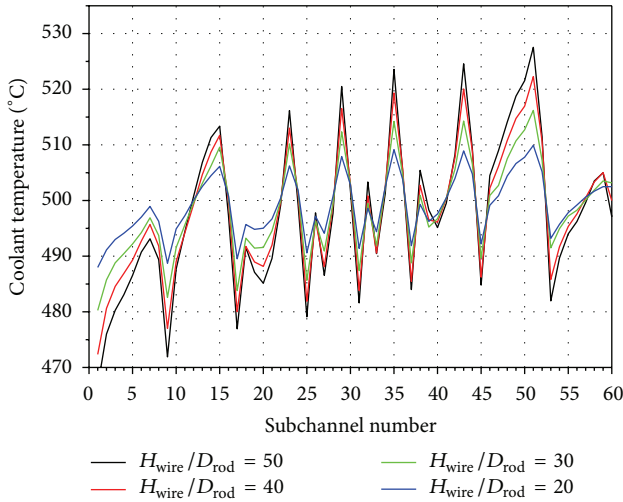


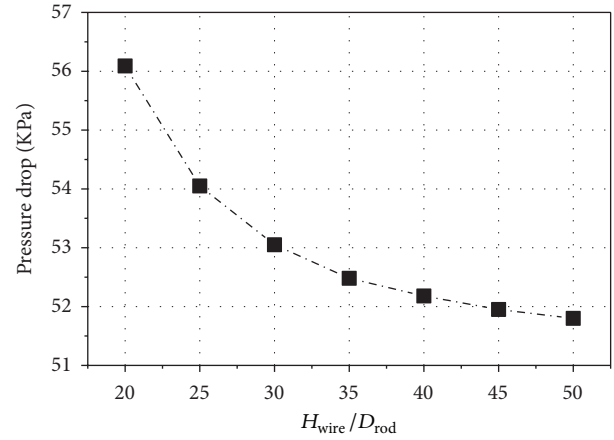
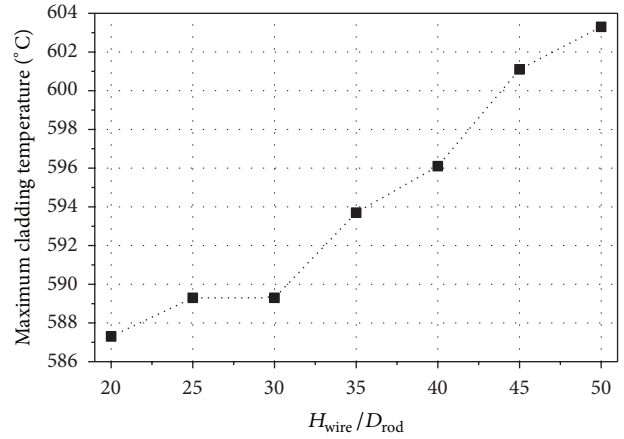
FIGURE 8: Pressure drop of two kinds of assembly.

FIGURE 9: Exit cooling temperature profile with different  $H_{\text{wire}}/D_{\text{rod}}$  values.

#### 4. Conclusion and Discussion

The subchannel code ATHAS is modified with distributed resistance model to meet the demand of wire wrapped SCWR assembly. Conclusions can be concluded as follows.

- (1) The assembly with wire wrap can obtain a more uniform coolant temperature profile than the grid spaced assembly, which will result in a lower peak cladding temperature.
- (2) The pressure drop in a wire wrapped assembly is less than that in a grid spaced assembly, which can reduce the operating power of pump effectively.
- (3) The wire wrap pitch has significant effect on the flow in the assembly. Smaller  $H_{\text{wire}}/D_{\text{rod}}$  will result in stronger cross flow, a more uniform coolant temperature profile, and also a higher pressure drop.

FIGURE 10: Pressure drop value with different  $H_{\text{wire}}/D_{\text{rod}}$ .FIGURE 11: The peak cladding temperature comparison with different  $H_{\text{wire}}/D_{\text{rod}}$  values.

Although the feasibility of wire wrapped assembly from the thermal-hydraulic point of view is approved in this work, the flow-induced vibration induced by wire wrap still needs further study.

#### Nomenclature

$A$ :	Area ( $\text{m}^2$ )
$C_g, C_s, C_T$ :	Empirical correction factor
$D_e$ :	Hydraulic diameter (m)
$f$ :	Frictional coefficient
$g$ :	Gravity acceleration ( $\text{m/s}^2$ )
$h$ :	Enthalpy (J/kg)
$h'$ :	Turbulent transport enthalpy (J/kg)
$H$ :	Heat transfer coefficient ( $\text{W}/(\text{m}^2 \cdot \text{K})$ )
$l$ :	Lateral pseudo length (m)
$L$ :	Channel centroid distance (m)
$K$ :	Frictional coefficient of spacer grid
$p$ :	Pressure (Pa)
$P$ :	Perimeter (m)
$Pr$ :	Prandtl number

Re:	Reynolds number
S:	Gap width between rods (m)
$t$ :	Temperature ( $^{\circ}$ C)
$u$ :	Velocity (m/s)
$u'$ :	Turbulent velocity (m/s)
$V$ :	Lateral velocity (m/s)
$W$ :	Lateral flow rate (kg/s)
$W'$ :	Turbulent mixing rate (kg/s)
$\Delta z$ :	Axial length (m)
$c$ :	Mixture velocity (m/s)
$u$ :	Mixture axial velocity (m/s)
$v$ :	Mixture lateral velocity (m/s)
$A_R$ :	Rod surface area (m <sup>2</sup> )
$A_{W'}$ :	Wire surface area within a control volume (m <sup>2</sup> )
$A''_{W'}$ :	Total wetted surface area including wire spacer (m <sup>2</sup> )
$D_{V'}$ :	Equivalent hydraulic diameter (m)
$F_R^A$ :	Axial component of the force exerted by the rod surface (N)
$F_R^L$ :	Lateral component of the force exerted by the rod surface (N)
$F_W^T$ :	Tangential component of the force exerted by the wire wrap surface (N)
$F_W^N$ :	Normal component of the force exerted by the wire wrap surface (N)
$S_T$ :	The rod pitch (m)
$S_L$ :	The distance between two rods in a transverse row (m)
$H_{\text{wire}}$ :	Wire wrap lead length (m)
$D_{\text{rod}}$ :	Fuel rod diameter (m).

### Greek Symbols

$\beta$ :	Direction angle, turbulent mixing coefficient
$\phi$ :	Fraction of perimeter
$\theta$ :	Angle between the channel axis and vertical
$\rho$ :	Density (kg/m <sup>3</sup> )
$\alpha$ :	The velocity makes an angle from the vertical
$\varphi$ :	Wire wrap angle.

### Subscripts

$b$ :	Bulk fluid
$c$ :	Channel
$i, j$ :	Subchannel number
$f$ :	Fluid
$k$ :	Gap number
$r$ :	Rod
$w$ :	Conduction wall.

### Acronyms

ATHAS:	Advanced thermal-hydraulics analysis subchannel
SCWR:	Super critical water-cooled reactor
CANDU:	Canada deuterium uranium
RBMK:	Reactor of large capacity channel type (in Russian abbreviations)
HPLWR:	High performance light water reactor.

## Conflict of Interests

The authors declare that there is no conflict of interests regarding the publication of this paper.

## Acknowledgments

The authors would like to express their appreciation to Atomic Energy of Canada Limited and Xi'an Jiaotong University for their financial support.

## References

- [1] J. Buongiorno, W. Corwin, P. Mac Donald et al., "Supercritical water reactor (SCWR) survey of materials experience and R&D needs to assess viability," Tech. Rep. INEEL/EXT-03-00693 (Revision 1), Idaho National Engineering Laboratory, Idaho Falls, Idaho, USA, 2003.
- [2] R. Duffey, I. Pioro, and H. Khartabil, "Supercritical water-cooled pressure channel nuclear reactors: review and status," in *Proceedings of the GLOBAL*, Tsukuba, Japan, October 2005.
- [3] A. Otsubo, T. Okada, N. Takahashi, K. Sato, and N. Hattori, "Occurrence of wear marks on fast reactor fuel pin cladding," *Journal of Nuclear Science and Technology*, vol. 36, no. 6, pp. 522–534, 1999.
- [4] X. Cheng and U. Müller, "Critical heat flux and turbulent mixing in hexagonal tight rod bundles," *International Journal of Multiphase Flow*, vol. 24, no. 8, pp. 1245–1263, 1998.
- [5] K. Fischer, T. Schulenberg, and E. Laurien, "Design of a supercritical water-cooled reactor with a three-pass core arrangement," *Nuclear Engineering and Design*, vol. 239, no. 4, pp. 800–812, 2009.
- [6] J. Buongiorno and P. MacDonald, "Supercritical water reactor (SCWR). Progress Report for the FY-03 Generation IV R&D activities for the development of the SCWR in the U.S.," Tech. Rep. INEEL/EXT-03-01210, Idaho National Engineering and Environmental Laboratory, 2003.
- [7] S. Himmel, A. G. Class, E. Laurien, and T. Schulenberg, "Determination of mixing coefficients in a wire-wrapped HPLWR fuel assembly using CFD," in *Proceedings of the International Conference on Advances in Nuclear Power Plants (ICAPP '08)*, pp. 670–679, Anaheim, Calif, USA, June 2008, P.8053.
- [8] E. Laurien, H. J. Wang, Y. Zhu, and H. Z. Li, "Flow and heat transfer of a heated rod with a wrapped wire inside a channel," in *Proceedings of the 4th International Symposium on Supercritical Water-Cooled Reactors*, Heidelberg, Germany, March 2009, paper no. 29.
- [9] L. Chandra, J. L. Nijeholt, D. C. Visser, and F. Roelofs, "CFD analyses on the influence of wire wrap spacers on heat transfer at supercritical conditions," in *Proceedings of the 4th International Symposium on Supercritical Water-Cooled Reactors*, Heidelberg, Germany, March 2009, paper no. 30.
- [10] J. Q. Shan, B. Zhang, C. Y. Li, and L. K. H. Leung, "SCWR subchannel code ATHAS development and CANDU-SCWR analysis," *Nuclear Engineering and Design*, vol. 239, no. 10, pp. 1979–1987, 2009.
- [11] I. L. Pioro, R. B. Duffey, and T. J. Dumouchel, "Hydraulic resistance of fluids flowing in channels at supercritical pressures (survey)," *Nuclear Engineering and Design*, vol. 231, no. 2, pp. 187–197, 2004.

- [12] I. L. Pioro, H. F. Khartabil, and R. B. Duffey, "Heat transfer to supercritical fluids flowing in channels—empirical correlations (survey)," *Nuclear Engineering and Design*, vol. 230, no. 1–3, pp. 69–91, 2004.
- [13] H.-Y. Jeong, K.-S. Ha, Y.-M. Kwon, Y.-B. Lee, and D. Hahn, "A dominant geometrical parameter affecting the turbulent mixing rate in rod bundles," *International Journal of Heat and Mass Transfer*, vol. 50, no. 5-6, pp. 908–918, 2007.
- [14] J. Q. Shan, L. Leung, J. Yang et al., "Subchannel code development for supercritical water-cooled reactor," in *Proceedings of the 4th International Symposium on Supercritical Water-Cooled Reactors*, Heidelberg, Germany, March 2009.
- [15] C. Y. Li, *Subchannel analysis of supercritical water reactor [M.S. thesis]*, Xi'an Jiaotong University, 2008.
- [16] C. Y. Li, J. Q. Shan, and L. K. H. Leung, "Subchannel analysis of CANDU-SCWR fuel," *Progress in Nuclear Energy*, vol. 51, no. 8, pp. 799–804, 2009.
- [17] H. Ninokata, A. Efthimiadis, and N. E. Todreas, "Distributed resistance modeling of wire-wrapped rod bundles," *Nuclear Engineering and Design*, vol. 104, no. 1, pp. 93–102, 1987.
- [18] T. Schulenberg, J. Starflinger, and J. Heinecke, "Three pass core design proposal for a high performance light water reactor," in *Proceedings of the 2nd International Conference on Innovative Nuclear Energy Systems (COE-INES '06)*, Yokohama, Japan, November 2006.
- [19] C. L. Waata, *Coupled Neutronics/Thermal-Hydraulics Analysis of a High-Performance Light-Water Reactor Fuel Assembly*, vol. 7233 of FZKA, Forschungszentrums Karlsruhe, Karlsruhe, Germany, 2005.
- [20] X. Cheng, T. Schulenberg, D. Bittermann, and P. Rau, "Design analysis of core assemblies for supercritical pressure conditions," *Nuclear Engineering and Design*, vol. 223, no. 3, pp. 279–294, 2003.
- [21] P. R. Diller, *Wire wrapped fuel pin hexagonal arrays for PWR service [Ph.D. thesis]*, Massachusetts Institute of Technology, 2005.

## Research Article

# Direct Numerical Simulation and Visualization of Subcooled Pool Boiling

**Tomoaki Kunugi<sup>1</sup> and Yasuo Ose<sup>2</sup>**

<sup>1</sup> *Kyoto University, Katsura, Nishikyo, Kyoto 615-8540, Japan*

<sup>2</sup> *Yamato System Engineer Co., Ltd., Wakaba, Hitachi, Ibaraki 317-0063, Japan*

Correspondence should be addressed to Tomoaki Kunugi; [kunugi@nucleng.kyoto-u.ac.jp](mailto:kunugi@nucleng.kyoto-u.ac.jp)

Received 5 September 2013; Revised 8 December 2013; Accepted 23 December 2013; Published 19 February 2014

Academic Editor: Yassin Hassan

Copyright © 2014 T. Kunugi and Y. Ose. This is an open access article distributed under the Creative Commons Attribution License, which permits unrestricted use, distribution, and reproduction in any medium, provided the original work is properly cited.

A direct numerical simulation of the boiling phenomena is one of the promising approaches in order to clarify their heat transfer characteristics and discuss the mechanism. During these decades, many DNS procedures have been developed according to the recent high performance computers and computational technologies. In this paper, the state of the art of direct numerical simulation of the pool boiling phenomena during mostly two decades is briefly summarized at first, and then the nonempirical boiling and condensation model proposed by the authors is introduced into the MARS (MultiInterface Advection and Reconstruction Solver developed by the authors). On the other hand, in order to clarify the boiling bubble behaviors under the subcooled conditions, the subcooled pool boiling experiments are also performed by using a high speed and high spatial resolution camera with a highly magnified telescope. Resulting from the numerical simulations of the subcooled pool boiling phenomena, the numerical results obtained by the MARS are validated by being compared to the experimental ones and the existing analytical solutions. The numerical results regarding the time evolution of the boiling bubble departure process under the subcooled conditions show a very good agreement with the experimental results. In conclusion, it can be said that the proposed nonempirical boiling and condensation model combined with the MARS has been validated.

## 1. Introduction

Despite extensive research efforts regarding the boiling heat transfer, the mechanism of the nucleate boiling phenomena is still unclear, and therefore its mechanistic model without any empirical correlation has not been developed. Since the temporal scales of boiling phenomena vary from the molecular scale motion in the heat conduction to the convective motion governed by the macroscopic scale in the bulk fluid, the scales of the phenomena of interest should be clear when a mechanistic boiling model is developed. Especially, the molecular motion is very fast in the nucleation process, thus, the nonthermal equilibrium state must play a very important role in this time scale.

On the other hand, a direct numerical simulation (DNS) of the boiling phenomena is one of the promising approaches in order to clarify the heat transfer characteristics of boiling phenomena and discuss their mechanism. With the advances

in recent years of high performance computational technology, several DNS procedures to solve the conservation equations of mass, momentum, and energy for liquid and vapor phases simultaneously when an interface is continuously evolving at and near a heated surface have been developed: to see the recent review [1] by one of the authors.

This study focuses mostly on the thermal equilibrium processes of boiling phenomena, which means that the nucleation theory can be applied to determine the size of vapor embryo, and then its growth, departure, and condensation processes will be considered later. In this paper, a brief review of the recent DNS on the boiling phenomena is firstly summarized, and then in order to validate the DNS data, the results [2–6] obtained by the DNS based on the MARS which is the interface volume tracking method [7] are compared to the visualization data obtained by using a very high speed video camera and a Cassegrain telescope [8].

## 2. Direct Numerical Simulation of Nucleate Bubble Growth, Departure, and Condensation

With the advances in recent years of high performance computational technology, several DNS procedures to solve the conservation equations of mass, momentum, and energy for liquid and vapor phases simultaneously when an interface is continuously evolving at and near a heated surface have been developed [1]. The solutions provide not only the detailed physics associated with thermal and hydrodynamic processes, but also the evolution of the interface shape. Most of the numerical investigations focus on either the nucleate boiling at moderate heat flux (isolated bubbles) or the stable film boiling. One of the key problems is the numerical description of two-phase flow. Typically, there are several methods which are used for the simulation of boiling heat transfer as follows.

*Marker and Cell (MAC) Method* [9]. The interface is marked by many massless particles that are convectively transported with the Eulerian velocity field and can be used to reconstruct the interface position on a fixed mesh. As far as the author knows, the first boiling simulation based on MAC method was done by Madhavan and Mesler in 1970 [10].

*Front Tracking (FT) Method* [11, 12]. This method seems to be an advanced version of MAC method and is thus based on massless particles that follow the motion of the interface driven by the Eulerian velocity fields. The interfaces are tracked by a Lagrangian frame, and the interface position can be tracked precisely, but it is necessary to introduce some artificial rules to treat the break-up interface and also coalescence of interfaces during computation. Esmaeeli and Tryggvason used the model mainly for the simulation of film boiling [13].

*Arbitrary Lagrangian-Eulerian (ALE) Method* [14–17]. This is based on a dynamic mesh that follows the motion of the interface. Thus, the interface coincides with a boundary of the computational domain at all times. According to this feature, the center of the control volume may not coincide often with the center of mass, and eventually the introduction of large artificial viscosity will be inevitable. An important advantage of the ALE method and boundary-fitted meshes in general is the possibility of treating the liquid-vapor interface as a boundary of the computational domain. This facilitates the calculation of the heat flux at the interface and therefore of the evaporation rate.

*Level-Set (LS) Method* [18, 19]. This method uses a field that contains information about the distance of a numerical cell to the interface and which is convectively transported with the Eulerian velocity fields. The interface is represented by the zero-contour line of the level-set field. The criticism regarding LS method is a transport feature of the distance function because the distance is not a measure of physical property. Recent works were reviewed in [1].

*Volume of Fluid (VOF) Method* [4, 20–29]. The most popular volume capturing procedure is based on the transport equation of VOF (volume of fluid). This uses a field that contains information about the volume fraction of one of the phases in a numerical cell and which is convectively transported with the Eulerian velocity fields. The volume fraction field has a piece-wise value at the position of the interface. There are some problems with VOF method, such as the interface reconstruction between neighborhood cells and the precise calculation of interface curvature. Some recent works on boiling simulation based on VOF methods were listed in [1]. However, none of the aforementioned models based on VOF method include any submodel for evaporation at the 3-phase contact line.

*2.1. Governing Equations Based on MARS.* The governing equations of the MARS consisted of the continuity equation for multiphase flows, the momentum equation based on a one-fluid model, and the energy equation with an external work done by a phase change phenomenon as follows:

$$\frac{\partial F_m}{\partial t} + \nabla \cdot (F_m \mathbf{u}) - F_m \nabla \cdot \mathbf{u} = 0, \quad (1)$$

$$\frac{\partial \mathbf{u}}{\partial t} + \nabla \cdot (\mathbf{u}\mathbf{u}) = \mathbf{G} - \frac{1}{\langle \rho \rangle} \nabla P - \nabla \cdot \boldsymbol{\tau} + \frac{1}{\rho} \mathbf{F}_v, \quad (2)$$

$$\frac{\partial}{\partial t} \langle \rho C_v \rangle T + \nabla \cdot (\langle \rho C_v \rangle T \mathbf{u}) = \nabla \cdot (\langle \lambda \rangle \nabla T) - P (\nabla \cdot \mathbf{u}) + Q, \quad (3)$$

where  $F$  is VOF fraction, the suffix  $m$  denotes the  $m$ th fluid or phase,  $t$  is time,  $P$  is pressure,  $T$  is temperature,  $\mathbf{G}$  is gravity,  $\boldsymbol{\tau}$  is viscous shear stress,  $\mathbf{F}_v$  is body force due to a surface tension based on the continuum surface force (CSF) model [30],  $\rho$  is density,  $C_v$  is specific heat at constant volume,  $\lambda$  is thermal conductivity,  $Q$  is heat source, and a bracket  $\langle \rangle$  denotes an average of thermal properties. In order to satisfy the conservation of  $F$ , the third term of the continuity equation (1) must be included. The second term of the right hand side of the energy equation (3), that is, the Clausius-Clapeyron relation, was considered as the external work done by the phase change, for example, a bubble oscillation caused by the expansion and contraction with the bubble growth and condensation processes. The interface volume tracking technique [7] was applied to the continuity equation in the MARS. The projection method [31] was applied to solve the momentum equation and the pressure Poisson equation was solved by the Bi-CGSTAB [32].

*2.2. Nonempirical Boiling and Condensation Model.* The boiling and condensation model in the MARS for the subcooled nucleate boiling phenomena consisted of both a nucleation model and a bubble growth-condensation model based on the temperature-recovery method [2, 3]. This model was applied only to the interfacial cells which have the VOF fraction between 0 and 1. A density-change between water

and vapour was considered as a volume-change by a phase change ratio  $\Delta g_v$ , expressed as

$$\Delta g_v = \frac{(\rho_l C_{pl} \Delta T)}{(\rho_g h_{lv})}, \quad (4)$$

where  $C_p$  is specific heat at constant pressure,  $\Delta T$  is degree of superheat or subcooling ( $T_{\text{sat}} - T$ ),  $h_{lv}$  is latent heat, and the suffixes of  $g$  and  $l$  denote gas and liquid phases, respectively. Equation (4) represents the ratio of the sensible heat to the latent heat at the interfacial cell. To conserve the total volume, the following constraint condition must be satisfied:

$$(F_l - |\Delta g_v|) + (F_g + |\Delta g_v|) = 1: \text{ for evaporation process,}$$

$$(F_l + |\Delta g_v|) + (F_g - |\Delta g_v|) = 1: \text{ for condensation process.} \quad (5)$$

The improved enthalpy method consists of (4)-(5) based on the assumptions of a zero-thickness interface and means a “rapid” phase change from “State 1 (Water)” to “State 2 (Vapour)” or *vice versa* due to the local quasi-thermal equilibrium hypothesis. This hypothesis requests another contradictory assumption that is a “very slow” phase change from “State 1” to “State 2.” In order to satisfy this requirement, a finite thickness of interface must be considered and both from/to “very slow” to/from “rapid” changes will occur simultaneously in the phase change process. This process can be described by a relaxation or waiting time for consuming the latent heat at the interface region, that is, the unsteady heat conduction in the finite interface region as the “very slow” change process: the relaxation time  $\Delta\tau$  can be defined as a time when the phase change front is passing through a fictitious interface thickness  $\Delta$ , so that  $\Delta\tau$  can be expressed by using the thermal diffusivity of the water  $\alpha$  as follows:

$$\Delta\tau = \frac{\Delta^2}{\alpha}. \quad (6)$$

On the other hand, a well-known thermal penetration length  $\delta$  for the unsteady heat conduction in a semiinfinite slab with a constant boundary temperature was approximated by the following expression:

$$\delta = \sqrt{12\alpha t}. \quad (7)$$

If the thermal penetration depth can be assumed the same as the fictitious interface thickness,  $\Delta\tau$  can substitute into (7):  $\delta = \sqrt{12}\Delta$ . As a result, an invariant relation between the thermal penetration length and the fictitious interface thickness can be obtained as follows:

$$\frac{\Delta}{\delta} = (\sqrt{12})^{-1} \approx 0.3. \quad (8)$$

According to this relationship, the fictitious interface thickness in around 30% of the thermal penetration depth corresponds to the “very slow” phase change process. In other words, the rapid phase changed volume during  $\Delta\tau$  is 70% of the thermal penetration depth, not 100%. In

this study, the relaxation time can be considered to control the VOF function as a phase change limiter. For example, the relaxation time for both phase-fronts is assumed to be 15% at either edge of the interface such as evaporation or condensation front as follows:

$$\text{VOF limiter: } 0.15 \leq F \leq 0.85. \quad (9)$$

This proposed model has been named the “nonempirical boiling and condensation model” by the authors [5].

### 3. Visualization Experiments

**3.1. Experimental Setup.** In order to verify the boiling and condensation model, the visualization experiments of subcooled pool boiling by using ultrahigh speed video camera with a highly magnified telescope system have been conducted [8]. Figure 1 shows the schematic of experimental apparatus. Test section was a rectangular section of which wall was made of polycarbonate. The size of the test chamber was 150 mm (Length)  $\times$  150 mm (Width)  $\times$  250 mm (Height). Test section was filled with the purified water. Water in a pool was open to the air, so the system pressure was an atmospheric pressure. The distilled water was used as a working fluid and the degassing was done by using the subheater. The water temperature, that is, the degree of subcooling, was controlled by the subheater located at the bottom of the pool. Test heater was a platinum wire of 0.1 mm in diameter located on the flat polycarbonate plate to prevent the natural convection. Direct electric current was supplied to the platinum, and boiling bubbles were generated somewhere on the wire. The degree of subcooling  $\Delta T_{\text{sub}}$  was set from 0 to 21.5°C, and heat flux was also set to 0.25 W/mm<sup>2</sup>.

The bubble behavior was visualized by using an ultrahigh speed video camera (Phantom 7.1, Vision Research Co.) with the Cassegrain optical system (Seika Co.) which works as the highly magnified telescope. The frame rate of recording was 10,000–60,000 frames per ms.

**3.2. Experimental Results.** Figure 2 shows the time variation of bubble volume in subcooled pool boiling at various degrees of subcooling by using simple image analyses [6, 8]. The bubble volume was estimated based on an assumption that the bubble was a spheroid. The thickness of the bubble edgeline was 30  $\mu\text{m}$ , that is, 6–10  $\mu\text{m}$  per pixel, so the error of the bubble volume based on the above spatial resolution was  $\pm 2$ –13%. Every generated bubble showed almost the same behavior: the bubble size, the deformation history, the interval of bubble generation, and so forth were almost the same and were periodically observed. The open symbols depict the experimental data before the bubble departure, and the solid symbols depict the data after the bubble departure. In the case of  $\Delta T_{\text{sub}} = 0.1^\circ\text{C}$ , that is, almost the saturated boiling, the bubble volume is monotonically increasing, and then the bubble departs from the heating surface. With increase of the degree of subcooling, especially,  $\Delta T_{\text{sub}} \geq 10.3^\circ\text{C}$ , the bubble growth rate is decreased and the departure time of bubble is also reduced. It seems that the bubble departure is accelerated.

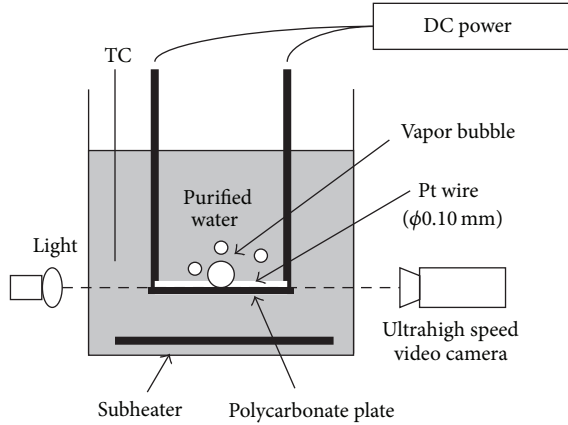


FIGURE 1: Schematic of visualization experimental apparatus.

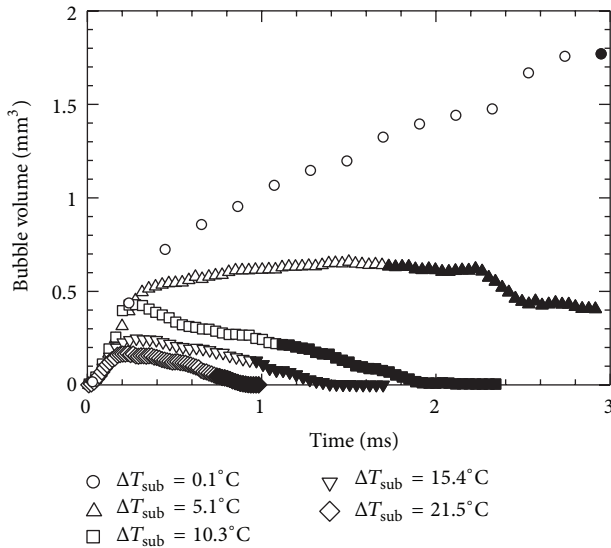


FIGURE 2: Time variation of bubble volume in subcooled pool boiling at various degrees of subcooling [6].

In order to estimate the time variation of bubble shape, Figures 3(a), 3(b), and 3(c) show the bubble height  $H$ , width  $W$ , and the aspect ratio  $H/W$  at various degrees of subcooling, respectively. The open and solid symbols were defined the same as in Figure 2. In Figure 3(a), the height of the bubble is monotonically increasing and the growth rate of the bubble height is almost independent on the degree of subcooling until the bubble departure from the heating surface. In contrast, the width of the bubble decreases with the increase of the degree of subcooling as shown in Figure 3(b). In Figure 3(c), the aspect ratio of the bubble increases with the increase of the degree of subcooling; that is, the bubble shape becomes more vertically elongated just before the bubble departure from the heating surface. A part of this phenomenon might be related to the condensation because the subcooled water entrains to the root of growing bubble due to the inertia force caused by the surface tension.

From the results of the visualization experiments, it is found that the processes of bubble departure from the heating surface in subcooled pool consisted of the following processes:

- (1) the bubble is generated and is growing with the horizontally elongated shape in subcooled pool, then,
- (2) the bubble becomes of vertically elongated shape because of the recoil force due to the surface tension, and finally,
- (3) the bubble is departed from the heating surface due to both the inertia force and the condensation due to the entrainment of subcooled water.

## 4. Comparison of Numerical Results to Visualization Results

**4.1. Computational Domain.** In order to validate the numerical simulation, the bubble departing behaviors obtained in Section 3 were compared to the 3D numerical simulations based on the MARS coupled with the nonempirical boiling and condensation model described in Section 2.2. Figure 4 shows the computational domain. The computational domain size was  $2.7 \text{ mm} \times 2.0 \text{ mm} \times 2.7 \text{ mm}$ . The computational cell size was  $20\text{--}100 \mu\text{m}$  in  $x$  and  $z$  directions, respectively, and  $20 \mu\text{m}$  in  $y$  direction. The number of computational cells was  $103 \times 83 \times 103$ , and the time increment in the computation was set to  $1 \mu\text{s}$ . The periodic boundary conditions were imposed at the  $x$  and  $z$  directions, respectively. The nonslip velocity boundary conditions were applied to all the walls, and the upper boundary condition in  $y$  direction was set to a constant hydraulic pressure condition. The computational conditions were basically the same as the experiments. The initial pressure was set to an atmospheric pressure and the degrees of subcooling in the water pool were set to  $5.1, 10.3, 15.4,$  and  $21.5^\circ\text{C}$ , the same as the experimental conditions. The heating platinum wire of  $0.1 \text{ mm}$  in diameter used in the experiment was located at the bottom of computational domain, and the volumetric heat source at the center of the wire was set to  $0.2 \text{ W}$  which was corresponding to the heat flux on the heating surface in the experiment:  $0.25 \text{ MW/m}^2$ . The initial temperature of heating wire was set to  $110^\circ\text{C}$  which was estimated by using a waiting time obtained from both the experimental results and the analytical solution of unsteady heat conduction equation for the thermal boundary layer on the heating wall. The solid heat conduction from the center of the heating wire to its surface was numerically considered. In order to evaluate the effect of the wettability on the heated wire surface, the static equilibrium contact angle  $\theta_{\text{eq}}$  between the wire surface and the liquid was set to  $20, 45, 60,$  and  $90^\circ$ .

Since this study focuses on the bubble departing behavior from the heated wire surface, the initial bubble shape was assumed at the maximum bubble size in a horizontal direction obtained from the experimental data. The initial bubble diameter was thus set to the values as shown in Table 1, and the initial bubble as a hemispherical shape was put at the center of the heating surface as shown in Figure 1. The initial

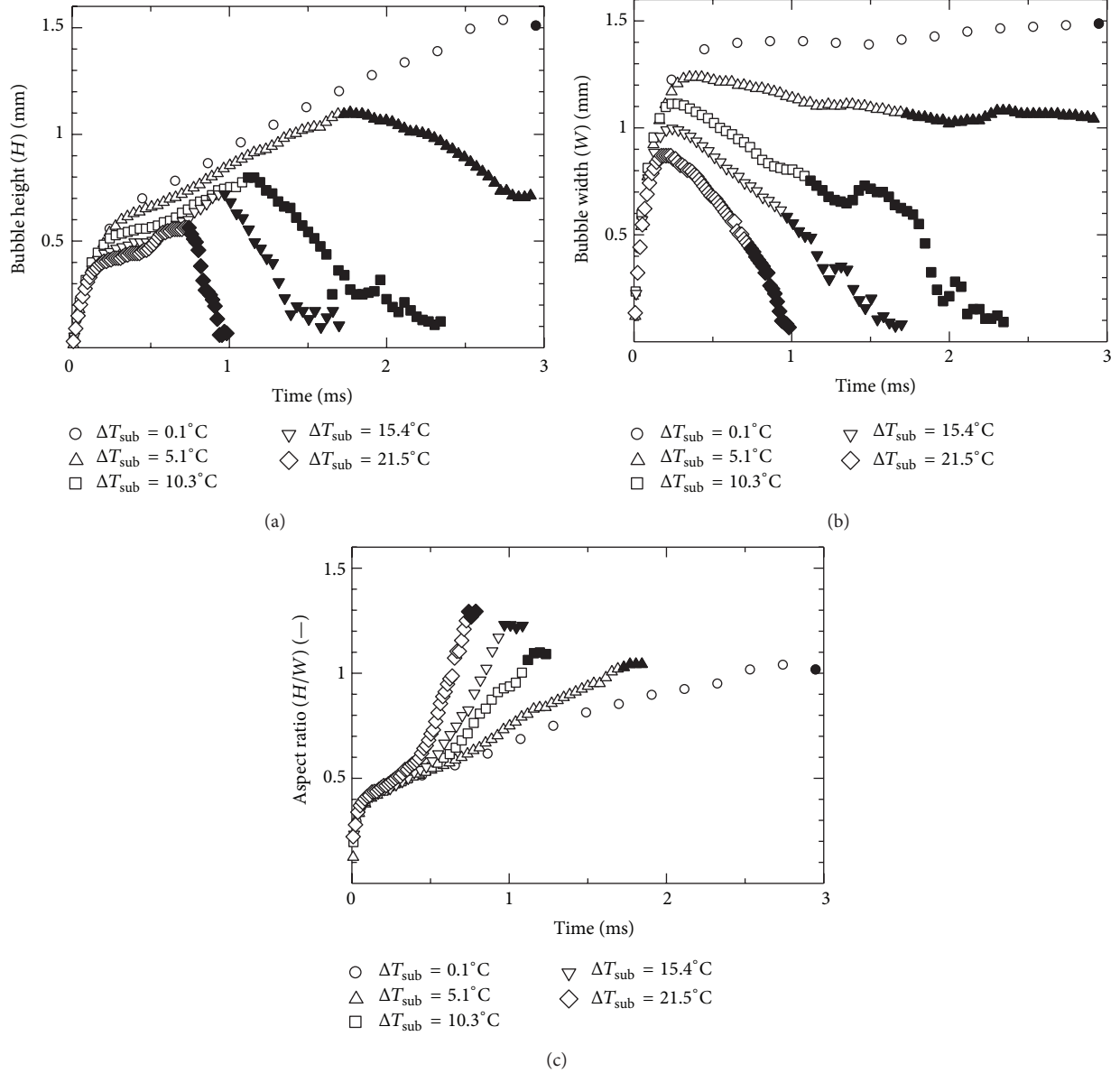


FIGURE 3: Time variation of bubble shape in subcooled pool boiling at various degrees of subcooling [6].

bubble temperature was also set to the saturated temperature under the atmospheric pressure. Although the velocity and temperature fields around the growing bubble were existed in the experiments, these initial fields in this numerical simulation were assumed to be both stationary and homogenous temperature fields with the degree of subcooling, respectively, because the experimental data corresponding to these fields could not be obtained.

The grid dependency of the computation is very important to calculate the curvature of the bubble which strongly depends on the number of grids. In general, a sphere can be approximated by 24 subdivisions, so the calculation of bubble curvature must be needed more than 24 grids. Since the minimum initial bubble diameter as shown in Table 1 was  $(2r_a, 2r_b) = (0.88 \text{ mm}, 0.70 \text{ mm})$  in case of  $\Delta T_{\text{sub}} = 21.5^\circ\text{C}$ , the

TABLE 1: Initial bubble conditions.

$\Delta T_{\text{sub}}$ (K)	$r_a$ (mm)	$r_b$ (mm)
5.1	0.62	0.47
10.3	0.56	0.48
15.4	0.49	0.38
21.5	0.44	0.35

ratio of the bubble diameter to the grid size corresponded to  $(2r_a/\Delta, 2r_b/\Delta) = (44, 35)$ . All the ratios of the other cases were more than 24. This means that the number of grids for the bubble in this study could be sufficient for the bubble growth process, because the bubble size increased with the increase of time. However, the condensation process was different,

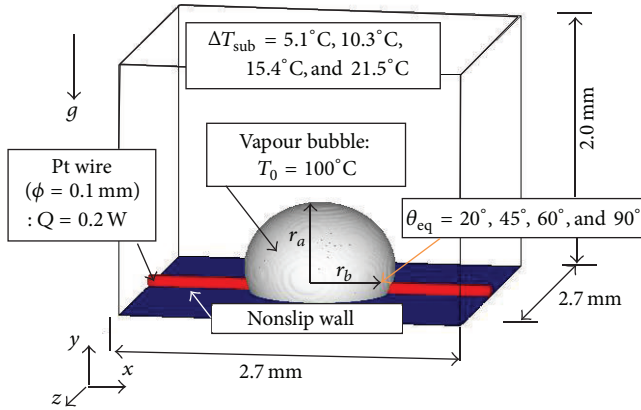


FIGURE 4: Computational domain.

because the bubble size decreased with the increase of time. The grid dependency in the condensation process will be discussed in Section 4.4.

**4.2. Bubble Departure Behavior.** Figures 5(a) and 5(b) show the time variation of bubble departing behavior observed in the experiments (upper) and the numerical simulation (lower) at  $\Delta T_{\text{sub}} = 10.3$  and  $21.5^\circ\text{C}$ , respectively.

The results of numerical simulation show the bubble shapes as an isosurface of  $\text{VOF} = 0.5$ , the temperature contours, and the velocity vectors. At  $\Delta T_{\text{sub}} = 10.3^\circ\text{C}$  (Figure 5(a)), the numerical results retrieved the experimental ones that the bubble changed from the flattened shape in the superheated layer to the vertically elongated one in the saturated or subcooled liquid layer before the bubble departure from the heated wire surface. At  $\Delta T_{\text{sub}} = 21.5^\circ\text{C}$  (Figure 5(b)), the bubble shape became more vertically elongated with the increase of the degree of subcooling. From the results of numerical simulation at  $\Delta T_{\text{sub}} = 21.5^\circ\text{C}$ , it is found that a large upward velocity like a jet from the bottom of bubble to the top appears when the bubble becomes the vertically elongated shape.

In order to validate the time variation of bubble shape changes obtained from the numerical results, Figure 6 shows a quantitative comparison of the time variation of the bubble aspect ratio ( $H/W = \text{bubble height}/\text{bubble width}$ ) between the experimental data and the numerical simulation results at various degrees of subcooling. The open symbols depict the experimental data before the bubble departure, and the solid symbols depict the data after the bubble departure. The solid lines depict the numerical results before the bubble departure. As the results show, the time variations of the bubble aspect ratio obtained from the numerical results were in good agreement with the experimental data: with the increase of the degree of subcooling, (1) the bubble became more vertically elongated shape, and (2) the time interval from the bubble nucleation to its departure from the heated surface is decreasing.

However, it can be seen that the numerical results over predicted the time interval from the bubble nucleation to its departure from the heated surface, compared with the

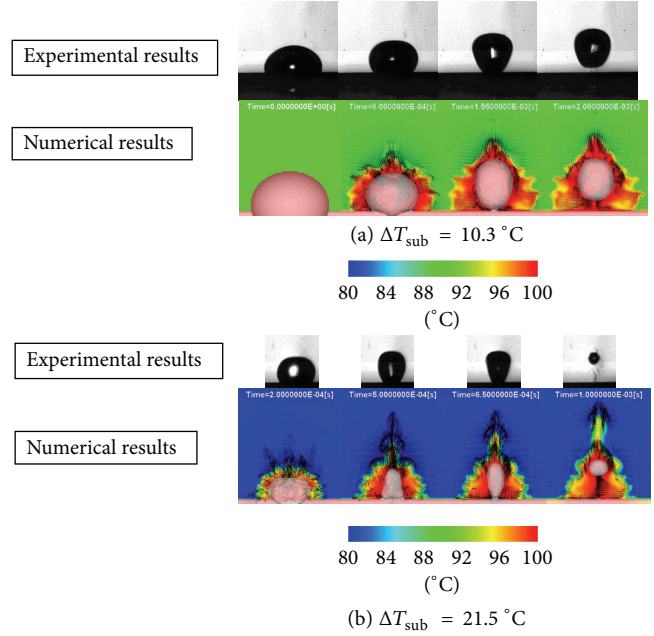


FIGURE 5: The comparison of the time variation of bubble departing behavior between experimental and numerical results.

experimental data. This reason might be considered so that the initial condition of numerical simulations could not be completely consistent with the experimental conditions. Especially, it seems that the boiling bubble behavior is sensitive to its initial temperature field. Therefore, the effect of initial temperature field for the bubble departure behavior was investigated. In this study, the temperature field after one bubble departure was used as initial condition in the simulation; that is, the initial temperature field with the bubble departure history, was considered.

Figures 7 and 8 show the comparison of the bubble shapes just before the bubble departure from the heated surface and the bubble aspect ratio between experiments and numerical results using the initial temperature field with or without bubble departure history at various degrees of subcooling, respectively. As the results show, both the bubble shape and bubble aspect ratio predicted by numerical simulations with bubble departure history rather than without bubble departure history are shown to be in good agreement with the experiments. Consequently, we can say that the present numerical simulation based on the MARS with the nonempirical boiling and condensation model can predict the bubble departure from the heated surface in subcooled pool boiling behaviors as experimentally observed.

**4.3. Effects of Wettability on Departure Behavior.** According to the previous study [33], the critical heat flux is increasing with the improvement of surface wettability. It means that the departure of bubble from the heating surface could be accelerated by the better surface wettability. Figure 9 shows the bubble departing behavior with the various static equilibrium contact angles  $\theta_{\text{eq}}$  of  $20$ ,  $45$ ,  $60$ , and  $90^\circ$  at

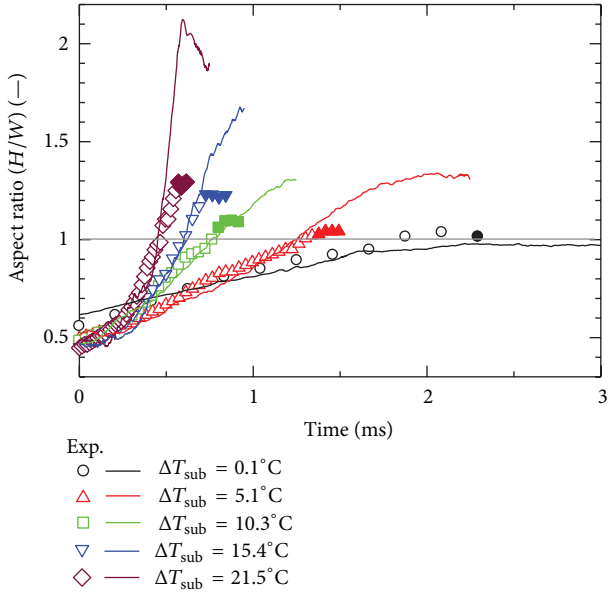


FIGURE 6: The comparison of time variation of bubble aspect ratio between experimental data and numerical results.

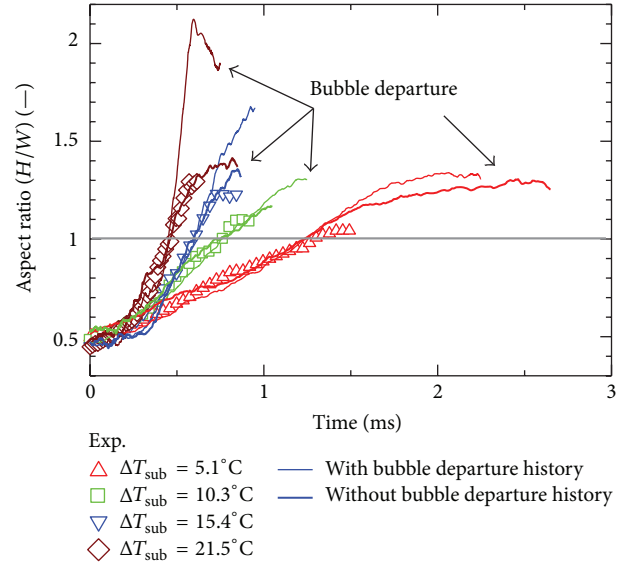


FIGURE 8: Effect of initial temperature field at various degrees of subcooling for bubble aspect ratio.

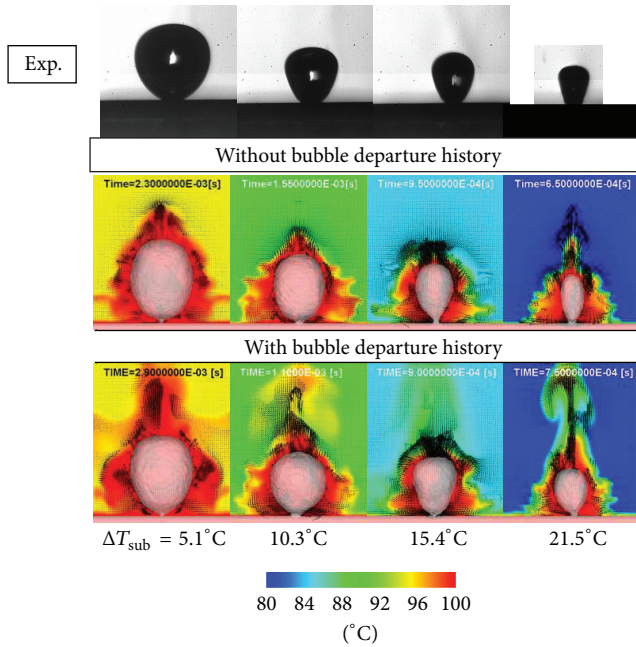


FIGURE 7: Effect of initial temperature field at various degrees of subcooling for bubble shape just before bubble departure from heated surface.

$\Delta T_{sub} = 21.5^\circ\text{C}$  [5]. As a result, it is found that the bubble departure from the heating surface becomes difficult with the deterioration of surface wettability. Therefore, it can be said that the present numerical results agree with the previous study [33].

Figure 10 shows a quantitative comparison of the time variation of the bubble aspect ratio ( $H/W = \text{bubble height/bubble width}$ ) between the experimental data [8] at

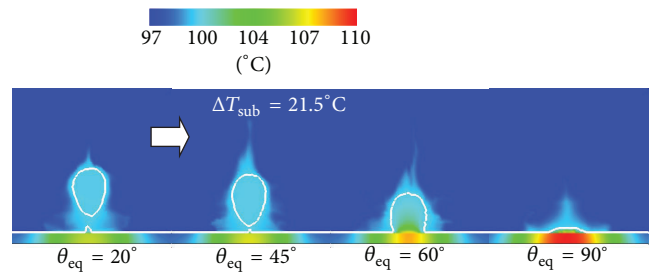


FIGURE 9: Numerical results of bubble shape and temperature distribution for  $\theta_{eq} = 20^\circ, 45^\circ, 60^\circ,$  and  $90^\circ$  at  $\Delta T_{sub} = 21.5^\circ\text{C}$  [5].

$\Delta T_{sub} = 5.1, 15.4,$  and  $21.5^\circ\text{C}$ , respectively [5]. The open symbols depict the experimental data before the bubble departure, and the solid symbols depict the data after the bubble departure. The solid lines depict the numerical results before the bubble departure. According to the results, it is found that the bubble aspect ratio of  $\theta_{eq} = 90^\circ$  did not show the vertically elongated shape regardless of the degrees of subcooling and that of  $\theta_{eq} = 20^\circ$  was shown to be in good agreement with the experimental data except in the case of  $\Delta T_{sub} = 21.5^\circ\text{C}$ . According to these results, it can be seen that the time variation of aspect ratio at  $\Delta T_{sub} = 21.5^\circ\text{C}$  was overpredicted, compared to the experimental data. This reason might be considered so that the initial condition of numerical simulations was not completely consistent with the experimental conditions: temperature and velocity fields. Especially, it seems that the boiling bubble behaviour of high subcooling condition is sensitive to its initial temperature field. Therefore, the temperature field experiencing one bubble departing history was used as the initial condition for  $\Delta T_{sub} = 21.5\text{K}$ . The dotted line in Figure 10 denotes the bubble aspect ratio of  $\theta_{eq} = 20^\circ$  using the initial temperature field with one bubble departing history at  $\Delta T_{sub} = 21.5^\circ\text{C}$ .

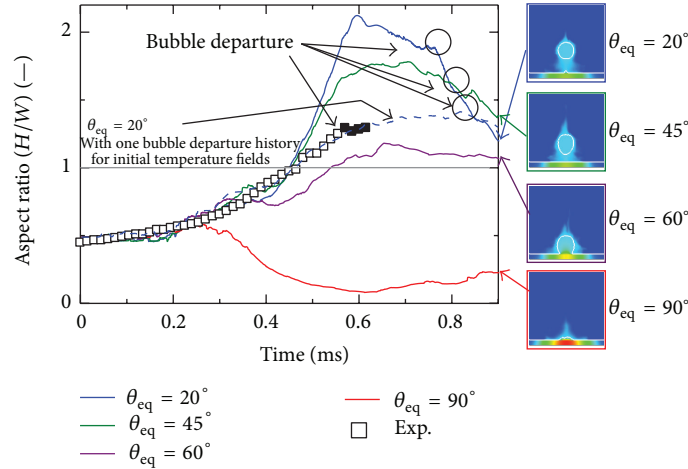


FIGURE 10: Time variation of bubble aspect ratio for  $\theta_{eq} = 20^\circ, 45^\circ, 60^\circ,$  and  $90^\circ$  at  $\Delta T_{sub} = 21.5^\circ\text{C}$  [5].

As a result, the time variations of bubble aspect ratio with one bubble departing history rather than without bubble departing history were shown to be in good agreement with the experiments.

**4.4. Bubble Condensation Behaviors.** Figure 11 shows the computational domain and the boundary conditions for the condensation process. The domain size was  $2.5\text{ mm} \times 2.5\text{ mm} \times 2.5\text{ mm}$ , and the uniform computational grids of  $50\ \mu\text{m}$  in  $x$ ,  $y$ , and  $z$  directions were used. The radius of bubble departure at various degrees of subcooling obtained from the experiment as shown in Table 2 was used as an initial vapor bubble, and then it was put as a sphere bubble in the grid nearest the wall. The ratios of the bubble diameter to the grid size were 22 for  $\Delta T_{sub} = 5.1^\circ\text{C}$ , 14 for  $\Delta T_{sub} = 10.3^\circ\text{C}$ , 12 for  $\Delta T_{sub} = 15.4^\circ\text{C}$ , and 8 for  $\Delta T_{sub} = 21.5^\circ\text{C}$ . The initial temperature field calculated until the temperature at the heated surface became larger than  $110^\circ\text{C}$ . The time increment in the computation was set to  $1\ \mu\text{s}$ . Other conditions were the same as the bubble growth process simulation.

Figure 12 shows the comparison between experimental and computational results at  $\Delta T_{sub} = 15.4^\circ\text{C}$ . Despite the usage of rather small number of grids compared to the growth process, the computational results showed good agreement with the experimental data. On the other hand, in case of  $\Delta T_{sub} = 21.5^\circ\text{C}$ , the computational results by using  $50\ \mu\text{m}$  grids showed a slower condensation compared to the experimental results as shown in Figure 13. The  $50\ \mu\text{m}$  grid did not show enough spatial resolution. Thus, the smaller grid sizes as the grid refinement test by using  $25\ \mu\text{m}$  and  $10\ \mu\text{m}$  applied to the same condition were examined. As a result, the results by using  $10\ \mu\text{m}$  grid showed fairly good agreement in the early stage of the condensation process with high subcooling  $\Delta T_{sub} = 21.5^\circ\text{C}$ . The  $10\ \mu\text{m}$  grid size corresponds to the ratio of 40, so the grid ratio could be sufficient.

## 5. Conclusions

The numerical simulations based on the MARS with the nonempirical boiling and condensation model considering

TABLE 2: Radius of bubble departure obtained from experiments for bubble condensation process.

$\Delta T_{sub}$ ( $^\circ\text{C}$ )	Radius of bubble departure (mm)
5.1	0.55
10.3	0.35
15.4	0.3
21.5	0.2

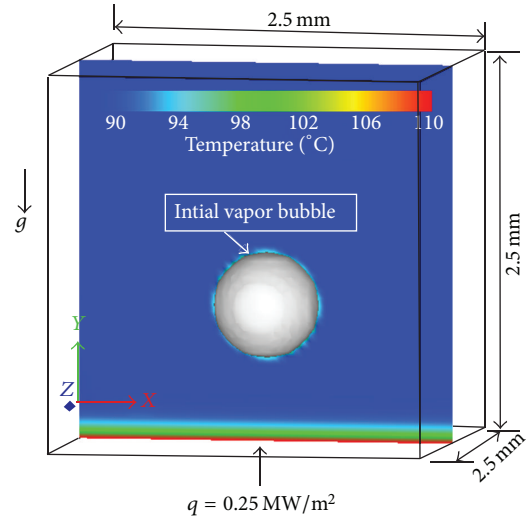


FIGURE 11: Computational domain for condensation process.

the relaxation time based on the local quasi-thermal equilibrium hypothesis were conducted for the bubble departing behavior from the heated wire surface in the subcooled pool boiling. The results of numerical simulations were compared with the experimental results, especially for the bubble shapes and the aspect ratios. As the results show, the numerical results for the bubble departing behavior were shown to be in very good agreement with the experimental results as follows.

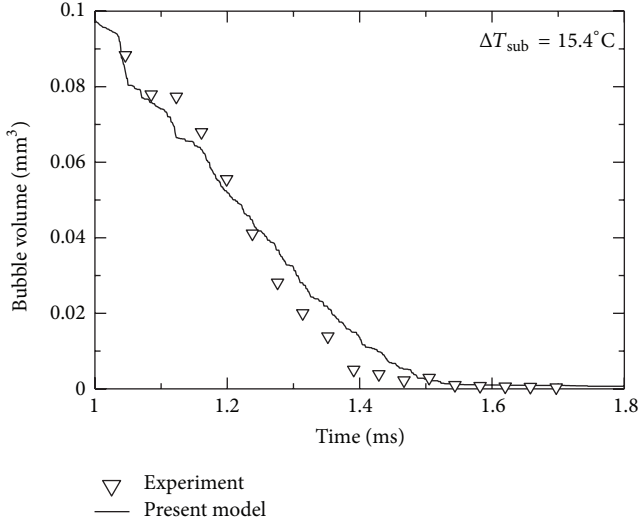


FIGURE 12: Comparison between experimental and computational results at  $\Delta T_{\text{sub}} = 15.4^\circ\text{C}$ .

- (1) The time interval from the bubble nucleation to its departing from the heated surface decreased with the increase of the degree of subcooling.
- (2) The aspect ratio of the bubble shape increased with the increase of the degree of subcooling; that is, the bubble shape became more vertically elongated before the bubble departure from the heated surface.
- (3) The initial temperature field with the bubble departure history has a profound effect on bubble departure behavior.
- (4) The departure of bubble from the heating surface is accelerated by the better surface wettability. In the case of  $\theta_{\text{eq}} = 90^\circ$ , that is, the poor surface wettability, the bubble could not depart from the heating surface. On the other hand, the time variations of bubble aspect ratio in case of  $\theta_{\text{eq}} = 20^\circ$  predicted by numerical simulation were shown to be in good agreement with experimental data.
- (5) The initial temperature field experiencing one bubble departing history has a profound effect on the bubble departing behaviour.

Resulting from the numerical simulations on the subcooled pool boiling phenomena, the numerical results obtained by the MARS are validated by comparing to the experimental ones and the analytical solutions. The numerical results regarding the time evolution of the boiling bubble growth/departure processes under the subcooled conditions were shown to be in a very good agreement with the experimental results. In conclusion, it can be said that the proposed nonempirical boiling and condensation model combined with the MARS has been almost validated. The remaining issue needs to consider a microlayer model [34] underneath the nucleate bubble close to the saturated condition. However, according to the present DNS results, the influence of the

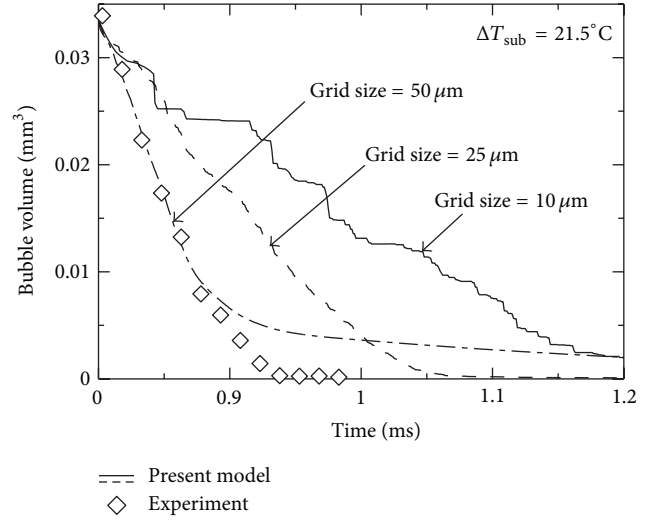


FIGURE 13: Comparison between experimental and computational results at  $\Delta T_{\text{sub}} = 21.5^\circ\text{C}$ .

microlayer on the heat transfer might be limited in the highly subcooled conditions.

## Nomenclature

$C_p$ :	Specific heat at pressure (J/(kg·K))
$C_v$ :	Specific heat at constant volume (J/(kg·K))
$\mathbf{G}$ :	Gravity ( $\text{m/s}^2$ )
$F$ :	Volume of fluid (VOF) fraction (-)
$F_v$ :	Body force due to an interface tension ( $\text{N/m}^3$ )
$H$ :	Bubble height (m)
$h_{lv}$ :	Latent heat (J/kg)
$P$ :	Pressure (Pa)
$Q$ :	Heat source ( $\text{W/m}^3$ )
$q_w$ :	Wall heat flux ( $\text{W/m}^2$ )
$r_a$ :	Bubble semimajor axis (m)
$r_b$ :	Bubble semiminor axis (m)
$t$ :	Time (s)
$T$ :	Temperature ( $^\circ\text{C}$ )
$T_s$ :	Heating surface temperature ( $^\circ\text{C}$ )
$u$ :	Velocity (m/s)
$W$ :	Bubble width (m)
$x, y, z$ :	$x, y$ , and $z$ direction.

## Greek Letters

$\alpha$ :	Thermal diffusivity ( $\text{m}^2/\text{s}$ )
$\delta$ :	Thermal penetration length (m)
$\Delta$ :	Fictitious interface thickness (m)
$\Delta g_v$ :	Phase change ratio (-)
$\Delta T_{\text{sub}}$ :	Degree of subcooling ( $^\circ\text{C}$ )
$\Delta\tau$ :	Relaxation time (s)
$\Delta x_s$ :	Distance to the heating surface (m)
$\lambda$ :	Thermal conductivity ( $\text{W}/(\text{m}\cdot\text{K})$ )

- $\theta_{eq}$ : Static equilibrium contact angle ( $^{\circ}$ )  
 $\rho$ : Density ( $\text{kg/m}^3$ )  
 $\sigma$ : Interface tension coefficient ( $\text{N/m}$ )  
 $\tau$ : Viscous share stress ( $\text{N/m}^2$ ).

### Subscripts

- $g$ : Gas phase  
 $l$ : Liquid phase.

### Conflict of Interests

The authors declare that there is no conflict of interests regarding the publication of this paper.

### References

- [1] T. Kunugi, "Brief review of latest direct numerical simulation on pool and film boiling," *Nuclear Engineering and Technology*, vol. 44, no. 8, pp. 847–854, 2012.
- [2] T. Kunugi, N. Saito, T. Fujita, and A. Serizawa, "Direct numerical simulation of pool and forced convective flow boiling phenomena," in *Proceedings of 12th International Heat Transfer Conference*, vol. 3, pp. 497–502, Grenoble, France, 2002.
- [3] Y. Ose and T. Kunugi, "Development of a boiling and condensation model on subcooled boiling phenomena," *Energy Procedia*, vol. 9, pp. 605–618, 2011.
- [4] Y. Ose and T. Kunugi, "Numerical study on subcooled pool boiling," *Progress in Nuclear Science and Technology*, vol. 2, pp. 125–129, 2011.
- [5] Y. Ose and T. Kunugi, "Numerical simulation on subcooled pool boiling phenomena based on non-empirical boiling and condensation model," in *Proceedings of the 15th International Topical Meeting on Nuclear Reactor Thermal Hydraulics (NURETH '15)*, NURETH15-290, Pisa, Italy, May 2013.
- [6] Y. Ose, Z. Kawara, and T. Kunugi, "Numerical simulation of subcooled pool boiling compared with experimental data and analytical equations," in *Proceedings of The 13th International Topical Meeting on Nuclear Reactor Thermal Hydraulics (NURETH '09)*, N13PI202, Kanazawa City, Japan, October 2009.
- [7] T. Kunugi, "MARS for multiphase calculation," *International Journal of Computational Fluid Dynamics*, vol. 9, no. 1, pp. 563–571, 2001.
- [8] Z. Kawara, T. Okoba, and T. Kunugi, "Visualization of behavior of subcooled boiling bubble with high time and space resolutions," in *Proceedings of the 6th Pacific Symposium on Flow Visualization and Image Processing (PSFVIP '06)*, pp. 424–428, Honolulu, Hawaii, USA, 2007.
- [9] F. H. Harlow and J. E. Welch, "Numerical calculation of time-dependent viscous incompressible flow of fluid with free surface," *Physics of Fluids*, vol. 8, no. 12, pp. 2182–2189, 1965.
- [10] S. Madhavan and R. Mesler, "A study of vapour bubble growth on surfaces," *Heat Transfer*, vol. 5, p. B2.6, 1970.
- [11] G. Tryggvason, B. Bunner, A. Esmaeeli et al., "A front-tracking method for the computations of multiphase flow," *Journal of Computational Physics*, vol. 169, no. 2, pp. 708–759, 2001.
- [12] S. O. Unverdi, "A front-tracking method for viscous, incompressible, multifluid flows," *Journal of Computational Physics*, vol. 100, no. 1, pp. 25–37, 1992.
- [13] A. Esmaeeli and G. Tryggvason, "Computations of film boiling. Part I: numerical method," *International Journal of Heat and Mass Transfer*, vol. 47, no. 25, pp. 5451–5461, 2004.
- [14] C. W. Hirt, A. A. Amsden, and J. L. Cook, "An arbitrary Lagrangian-Eulerian computing method for all flow speeds," *Journal of Computational Physics*, vol. 14, no. 3, pp. 227–253, 1974.
- [15] T. Fuchs, J. Kern, and P. Stephan, "A transient nucleate boiling model including microscale effects and wall heat transfer," *Journal of Heat Transfer*, vol. 128, no. 12, pp. 1257–1265, 2006.
- [16] J. Kern and P. Stephan, "Theoretical model for nucleate boiling heat and mass transfer of binary mixtures," *Journal of Heat Transfer*, vol. 125, no. 6, pp. 1106–1115, 2003.
- [17] S. W. J. Welch, "Direct simulation of vapor bubble growth," *International Journal of Heat and Mass Transfer*, vol. 41, no. 12, pp. 1655–1666, 1998.
- [18] S. Osher and J. A. Sethian, "Fronts propagating with curvature-dependent speed: algorithms based on Hamilton-Jacobi formulations," *Journal of Computational Physics*, vol. 79, no. 1, pp. 12–49, 1988.
- [19] V. K. Dhir, "Numerical simulations of pool-boiling heat transfer," *AIChE Journal*, vol. 47, no. 4, pp. 813–834, 2001.
- [20] C. W. Hirt and B. D. Nichols, "Volume of fluid (VOF) method for the dynamics of free boundaries," *Journal of Computational Physics*, vol. 39, no. 1, pp. 201–225, 1981.
- [21] M. Rudman, "Volume-tracking methods for interfacial flow calculations," *International Journal for Numerical Methods in Fluids*, vol. 24, no. 7, pp. 671–691, 1997.
- [22] O. Ubbink and R. I. Issa, "A method for capturing sharp fluid interfaces on arbitrary meshes," *Journal of Computational Physics*, vol. 153, no. 1, pp. 26–50, 1999.
- [23] W. F. Noh and P. Woodward, *SLIC (Simple Line Interface Calculation)*, Lecture Notes in Physics, Springer, 1976, Edited by K. W. Morton and M. J. Baines.
- [24] D. L. Youngs, "Time-dependent multi-material flow with large fluid distortion," in *Numerical Methods for Fluid Dynamics*, K. W. Morton and M. J. Baines, Eds., pp. 273–285, Academic Press, New York, NY, USA, 1982.
- [25] W. J. Rider and D. B. Kothe, "Reconstructing volume tracking," *Journal of Computational Physics*, vol. 141, no. 2, pp. 112–152, 1998.
- [26] S. W. J. Welch and T. Rachidi, "Numerical computation of film boiling including conjugate heat transfer," *Numerical Heat Transfer B*, vol. 42, no. 1, pp. 35–53, 2002.
- [27] S. Aus der Wiesche, "Bubble growth and departure during nucleate boiling: the occurrence of heat flux reversal," in *Proceedings of the 4th International Conference on Computational Heat and Mass Transfer*, 2005.
- [28] S. Hardt and F. Wondra, "Evaporation model for interfacial flows based on a continuum-field representation of the source terms," *Journal of Computational Physics*, vol. 227, no. 11, pp. 5871–5895, 2008.
- [29] C. Kunkelmann, K. Ibrahim, N. Schweizer, S. Herbert, P. Stephan, and T. Gambaryan-Roisman, "The effect of three-phase contact line speed on local evaporative heat transfer: experimental and numerical investigations," *International Journal of Heat and Mass Transfer*, vol. 55, no. 7-8, pp. 1896–1904, 2012.
- [30] J. U. D. Brackbill, "A continuum method for modeling surface tension," *Journal of Computational Physics*, vol. 100, no. 2, pp. 335–354, 1992.

- [31] A. Chorin, "Numerical solution of the navier-stokes equations," *Mathematics of Computation*, vol. 104, no. 22, pp. 745–762, 1968.
- [32] H. A. Van Der Vorst, "BI-CGSTAB: a fast and smoothly converging variant of BI-CG for the solution of nonsymmetric linear system," *SIAM Journal on Scientific and Statistical Computing*, vol. 13, no. 2, pp. 631–644, 1992.
- [33] S. G. Kandlikar, M. Shoji, and V. K. Dhir, *Handbook of Phase Change: Boiling and Condensation*, vol. 75, Taylor & Francis, 1999.
- [34] M. G. Cooper and A. J. P. Lloyd, "The microlayer in nucleate pool boiling," *International Journal of Heat and Mass Transfer*, vol. 12, no. 8, pp. 895–913, 1969.

## Research Article

# Influence of Spacer Grid Outer Strap on Fuel Assembly Thermal Hydraulic Performance

Jingwen Yan, Yuxiang Zhang, Baowen Yang, Weicai Li, and Yuemin Zhou

*Nuclear Fuel Research and Development Center, China Nuclear Power Technology Research Institute, Shenzhen 518026, China*

Correspondence should be addressed to Jingwen Yan; [yanjingwen@cgnpc.com.cn](mailto:yanjingwen@cgnpc.com.cn)

Received 10 October 2013; Accepted 24 December 2013; Published 11 February 2014

Academic Editor: Jianqiang Shan

Copyright © 2014 Jingwen Yan et al. This is an open access article distributed under the Creative Commons Attribution License, which permits unrestricted use, distribution, and reproduction in any medium, provided the original work is properly cited.

The outer strap as a typical structure of a spacer grid enhances the mechanical strength, decreases hang-up susceptibility, and also influences thermal hydraulic performance, for example, pressure loss, mixing performance, and flow distribution. In the present study, a typical grid spacer with different outer strap designs is adopted to investigate the influence of outer strap design on fuel assembly thermal hydraulic performance by using a commercial computational fluid dynamics (CFD) code, ANSYS CFX, and a subchannel analysis code, FLICA. To simulate the outer straps' influence between fuel assemblies downstream, four quarter-bundles from neighboring fuel assemblies are constructed to form the computational domain. The results show that the outer strap design has a major impact on cross-flow between fuel assemblies and temperature distribution within the fuel assembly.

## 1. Introduction

Most of PWRs consist of  $17 \times 17$  nuclear fuel assemblies that are supported by structural grids over the length of each particular assembly. Spacer grids are used to hold fuel rod bundles in position, maintain appropriate rod-to-rod clearance, and enhance critical heat flux. The outer strap as a typical structure of a spacer grid plays a very important role in enhancing the mechanical strength, decreasing hang-up susceptibility, and also influencing thermal hydraulic performance, for example, pressure loss, mixing performance, and flow distribution. However, it is difficult to carry out the related experiments to investigate these thermal hydraulic characteristics within rod-bundle-grids. Despite the great improvement of experimental technique, the experimental investigations are still expensive and require a relative long time to perform. Computational fluid dynamics (CFD) methodology then attracts more attention from the academic and industry society to simulate these complicated phenomena, including the cross-flow between bundle, mixing, and flow distributions.

Several studies have been carried out on flow mixing and heat transfer enhancement caused by spacer grid in rod-bundle geometry. Gandhir and Hassan used Reynolds-averaged Navier-Stokes (RANS) based turbulence model

for single-phase CFD analysis of flow in pressurized water reactor (PWR) assemblies [1]. Liu et al. implemented several readily available turbulence models in order to determine the model most suitable for the flow [2, 3]. Navarro and Santos used the  $k-\varepsilon$  model to perform flow simulations with the CFD code in a PWR  $5 \times 5$  rod bundle segment with a split-vane spacer grid [4]. Conner et al. conducted experiments to validate the CFD methodology for the single-phase flow conditions in pressurized water reactor (PWR) fuel assemblies [5]. Holloway et al. showed that there was a great variation of heat transfer distribution along a fuel rod due to the spacer grid type [6, 7]. A series of four-subchannel CFD simulations to analyze the heat transfer enhancement in a fully heated rod bundle with vane spacers were performed by In et al. [8]. By adjusting model coefficients adopted in a quadratic  $k-\varepsilon$  model, Baglietto and Ninokatahad previously have shown the promising capability of the RSM turbulence model in sufficiently accurate anisotropy modeling of the wall shear stress distribution and the velocity field in tight lattice fuel bundles [9]. Házi had demonstrated that the RSM could be accurately applied in simulating the rod bundle geometry [10].

To the best of the authors' knowledge, most of the CFD works are focusing on the hydraulic characteristics in the rod

TABLE 1: Projected areas of a mixing vane and a guide tap.

	Mixing vane (mm <sup>2</sup> )	Guide tap (mm <sup>2</sup> )
Grid Design 1	6.745	12.544
Grid Design 2	6.745	16.908

bundles with inner straps spacer grids but less attention had been paid to the hydraulic characteristics in the rod bundles with outer strap grids. In this study, four quarter-bundles from neighboring fuel assemblies are used to analyse the influence of spacer grid outer strap on fuel assembly thermal hydraulic performance. To be a reference, subchannel analysis is conducted by using FLICA, a subchannel analysis code.

## 2. CFD Modeling

**2.1. Grids Description.** In present study, two kinds of outer straps with the same inner straps were assembled and were used to investigate the influences of outer straps on the thermal hydraulic performance. As shown in Figure 1, grids of Design 1 and Design 2 have different outer strap designs. Design 2 has a guide tap on each of intersecting joints of outer strap and inner strap, but Design 1 has a guide tap on every other intersecting joint. The guide tap of Design 2 is much wider and lower than that of Design 1. Moreover, Design 2 has holes on the center of outer strap. The projected areas of mixing vane and guide tap are listed in Table 1, since the Design 2 has much more guide taps and the guide tap has larger projected area and the projected area of Design 2 is larger than that of Design 1.

**2.2. Computational Domain and Mesh.** To simulate the outer straps' influence between fuel assemblies downstream, four quarter-bundles from neighboring fuel assemblies are constructed to form the computational domain as shown in Figure 2(a). The diameter of rod is 9.5 mm, and the pitch is 12.6 mm. The inlet length before entering the grid is 50 mm, and the outlet length after leaving the grid is 522 mm (take the bottom face of the grid as reference plane). Consequently the total length of the flow domain as shown in Figure 2(b) is 572 mm.

Nonstructure tetrahedral mesh element is utilized in the grid region due to the complex geometry that consisted of springs and dimples of spacer grid. The application of extruded prism type mesh in the flow passage region may reduce the number of mesh elements and offer a better mesh quality. The mesh element size was elaborate setup for a good response of the detailed structure inside the grid. The total number of mesh element is up to 30 million.

**2.3. Simulation.** The simulation is based on a single-phase model and steady state condition. The physical parameters of water are calculated from IAPWS-IF97 code under 15.5 MPa, 310°C condition as constant and the flow is considered to be incompressible.

The mesh number of each simulation is more than 30 million. The boundary conditions in this calculation are listed

TABLE 2: Boundary conditions.

Boundary	Option	Value
Inlet	Uniform normal velocity	4.737 m/s
	Uniform temperature	310°C
Outlet	Relative static pressure	0 Pa
Periphery interface	Translational periodicity	
Grid	Nonslip wall, adiabatic	
Rod	Nonslip wall, wall heat flux*	

\*The power distributions of rod bundle are showed in Figure 3.

in Table 2. The Reynolds number in the fuel bundle could reach up to 500,000 under the above condition. The RNG  $k-\epsilon$  model which is less sensitive to the mesh and boundary condition was utilized in this simulation. The simulation is performed on a IBM high performance computation blade server with 128 cores for half an hour to get a steady converged solution, and the total 500 iterations were required to get this solution.

## 3. Results and Discussion

**3.1. Pressure Drop.** Pressure drop of a grid is a very important parameter. If the pressure drop increases, the lift force will need to be adapted. As shown in Figure 4, the pressure drop of Design 2 is about 6.9% larger than that of Design 1. This is due to the large projected area of Design 2, which causes more coolant to be blocked.

**3.2. Lateral Flow.** Lateral flow intensity is evaluated by the cross-sectional averaged lateral flow and is defined as

$$V_{\text{lateral}} = \sqrt{V_u^2 + V_v^2}, \quad (1)$$

where  $V_u, V_v$  are the cross-sectional averaged lateral velocity in directions X and Y. It is seen, in Figure 5, that the lateral flows of both Design 1 and Design 2 gradually increase before flowing into the grids and reach the maximum when coolant just leaves the grids, and then the cross-flow decreases gradually. Comparing the differences of lateral flow between the two grids, Design 1 has relatively smaller lateral flow upstream of the grid but a relatively larger lateral flow downstream of the grid.

The upstream and downstream lateral flows have different flow mechanisms. The lateral flow upstream is driven by flow redistribution induced by different subchannel pressure loss coefficient. As pointed out in the geometric illustration of Designs 1 and 2, the only difference is the outer strap structure, major in the guide tap geometrical characteristics, leading to different subchannel pressure loss coefficient distribution within the grids. In addition, according to Section 3.1, the side subchannel pressure loss coefficient of Design 2 is larger than that of Design 1, leading to more uneven flow distribution and stronger lateral flow.

While in the downstream, the lateral flow is mainly driven by mixing vane at the location very near to the grids downstream edge and that is the reason why Design 1

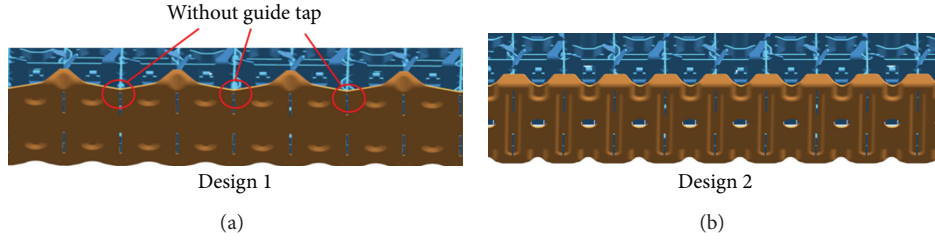


FIGURE 1: Schematic illustration of outer strap.

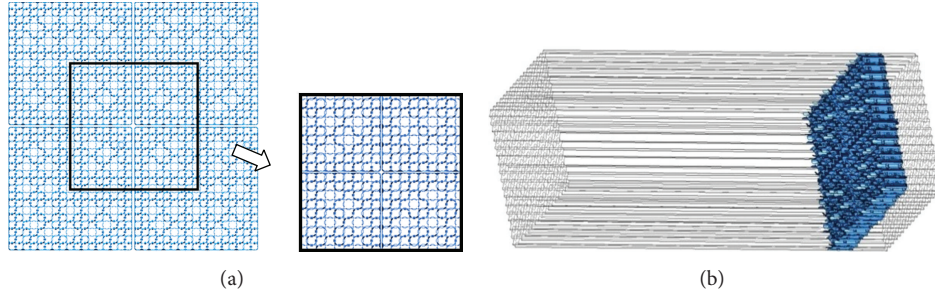


FIGURE 2: Computational domain and mesh.

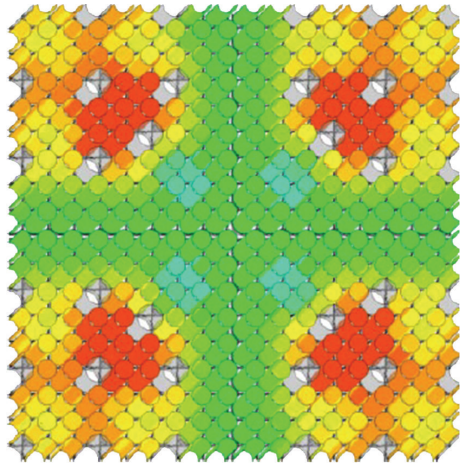


FIGURE 3: Power distributions.

and Design 2 have the same lateral flow intensity at this location. As shown in Figure 5, lateral flow induced by Design 2 is smaller than that induced by Design 1 in the downstream, showing the effect of reduced lateral flow of Design 2 compared to Design 1. Figure 6 shows the lateral flow velocity profile on each cross-sectional downstream grid. As presented in Figures 6(a)–6(c), lateral flow induced by Design 1 is much stronger than that induced by Design 2 in the region of the outer strap, which indicates that more lateral flow is blocked by Design 2 compared to Design 1.

**3.3. Cross Bundle Flow.** According to lateral flow analysis in Section 2.2, the two designs have obviously different flow

patterns near side channels. To further analyze the influence of outer straps on lateral flow, streamlines are created to obtain information about the coolant lateral spreading over the downstream of the grid. Figures 7(a)–7(e) shows streamline development, from grid upstream to outlet, of the coolant flow in near outer strap region and the red color is the top-down view of the subchannel investigated. The distance of the coolant spread on the lateral is showed on the top-down view of the streamline. Figures 7(a)–7(b) show that the coolant downstream the Design 1 has a stronger mixing because the intensity and extent of cross bundle flow induced by Design 1 are stronger than those induced by Design 2. Moreover, it is also noted that the geometrical effect of grid on lateral flow is usually limited within a 3 subchannel lateral distance downstream in axial flow travel of one span distance. Inside grids, the two grids have the similar flow pattern downstream.

Figure 8(a) shows that clip planes, numbered from 1 to 9, are created to quantitatively analyze the cross bundle flow at different axial location. Each clip plane is 50 mm high. The mass flow pass through each clip plane is calculated to analyze the cross bundle flow variation, shown in Figure 8(b). It is seen that the cross bundle mass flow gradually decreases as the flow develops downstream the grids. It can also be seen that the cross bundle mass flow of the Design 1 is much more than that of Design 2.

**3.4. Temperature Distribution.** Temperature distribution at the outlet is studied by CFX but also by a subchannel analysis code, FLICA, in present study. Figure 9 presents the subchannel-averaged temperature distribution at the outlet of one-quarter grid by using CFX. According to the structure characteristic, the grid is divided into 4 types of subchannels,

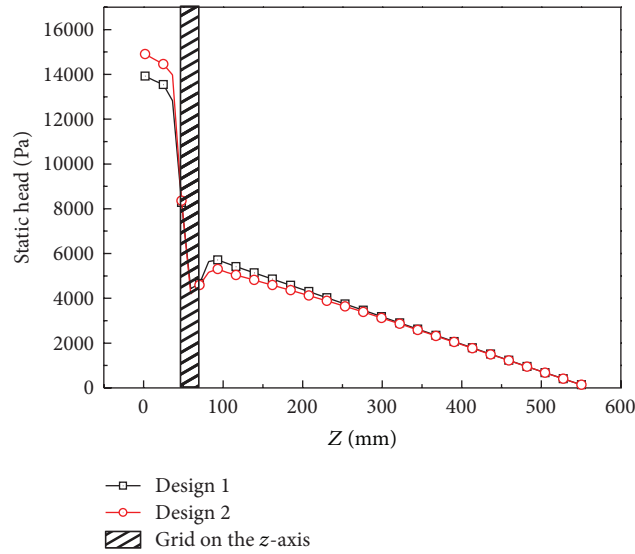


FIGURE 4: Pressure drop.

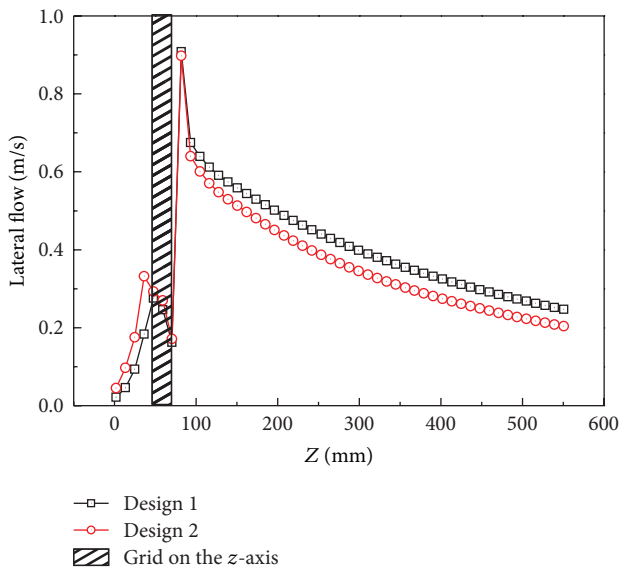


FIGURE 5: Lateral flow intensity.

side subchannels (green), guide thimble subchannels (yellow), typical subchannels (white), and Conner subchannel (blue). As shown in Figure 9, the hottest channel of the two grid appears at the side subchannels.

The CFX calculation result shows that the outlet temperature standard deviation is  $0.477^{\circ}\text{C}$  and  $0.419^{\circ}\text{C}$  for Design 2 and Design 1, respectively. Design 1 has a slightly smaller value compared to Design 2, meaning that the mixing effect of Design 1 is better than that of Design 2. The FLICA calculation result shows that the outlet temperature distribution is proceeding to more uniform as the mixing coefficient increases for either Design 1 or Design 2, shown in Figure 10. It is interesting to note that FLICA result shows that Design 2

always has smaller outlet temperature standard deviation than Design 1 does, meaning that the mixing effect of Design 2 is better. This conflict of FLICA and CFX results leads us to do further investigation of the subchannel outlet temperature distribution. As the illustration of Design 1 and 2 geometry, the only difference is the outer strap structure, major in the guide tap geometrical characteristics, leading to different subchannel pressure loss coefficient distribution within the grids and the local flow field in the vicinity of side channels. In typical subchannel analysis code like FLICA, the influence of outer strap structure is taken into account in terms of pressure loss coefficient only, which means that the resultant effect of flow redirection caused by guide tabs cannot be calculated. In contrast, CFX calculation takes every detailed geometrical influence on the resulted flow into account, reflected by the temperature variation in Figure 11. Since the cross-section averaged temperatures calculated by FLICA and CFX are the same (within  $0.15^{\circ}\text{C}$ ), it is reasonable to treat FLICA and CFX calculation as the right results in general, but CFX gives more detailed and reasonable temperature and flow distribution.

When we explore the outlet temperature distribution obtained by FLICA and CFX, it is interesting to note that the hottest channel presented by FLICA maintains the same for Design 1 and Design 2 at the same mixing coefficient, subchannel 26 when mixing coefficient equals to 0 and subchannel 16 for other mixing coefficients. Either subchannel 26 or subchannel 16 is a typical subchannel bounded by four fuel rods. However, the CFX calculation gives quite different results as expected. In CFX calculation, subchannel 37 is the hottest channel for Design 1 and subchannel 41 for Design 2, as shown in Figures 9(c)-9(d) and Figure 12. Subchannels 37 and 41 are side channels next to Design 1 outer strap and Design 2 outer strap, respectively. The CFX result clearly shows that the outer strap has a significantly impact on temperature distribution. It is also found that the temperature difference between FLICA and CFX for

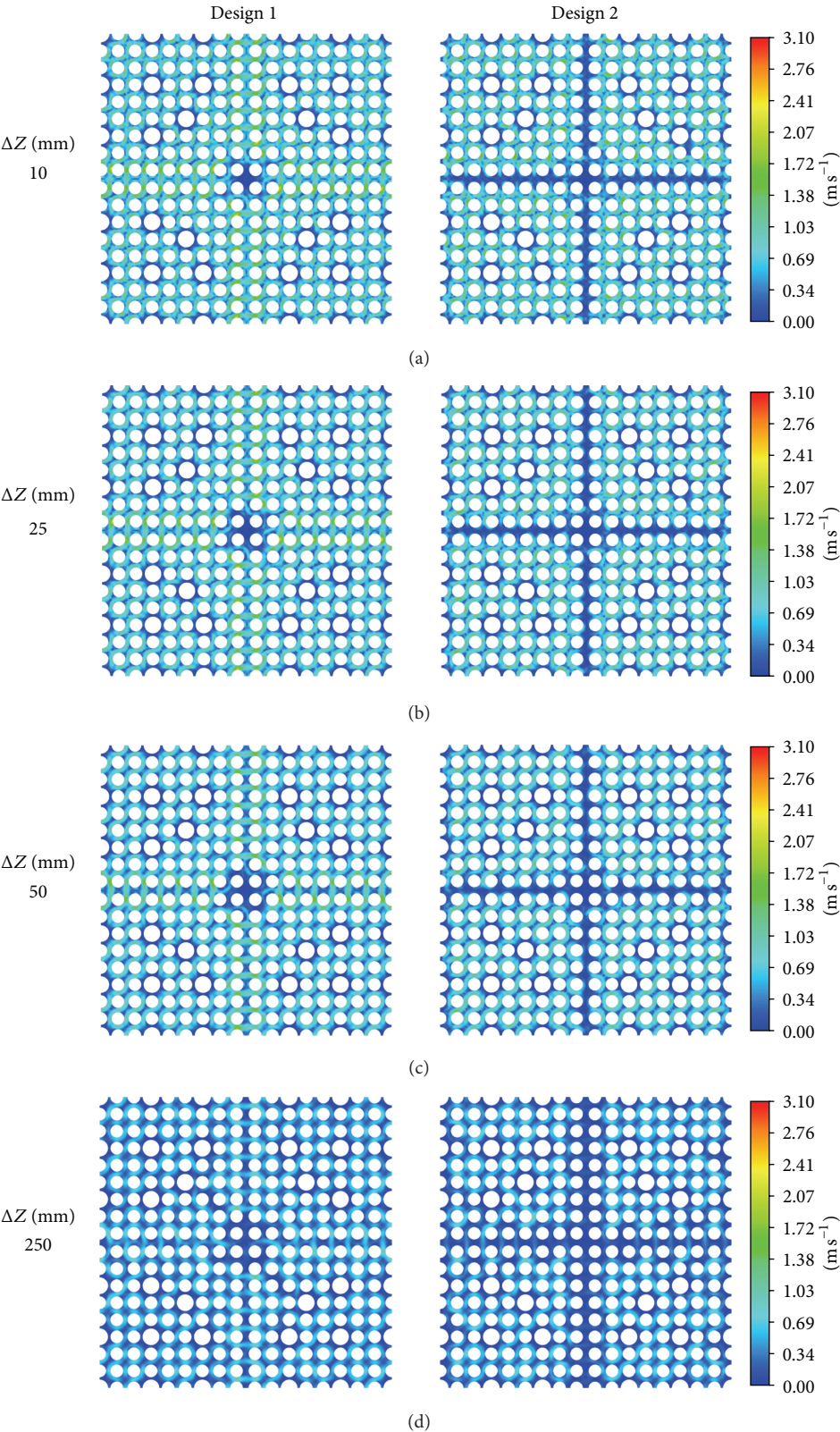


FIGURE 6: Lateral flow velocity profile ( $\Delta Z$  is the distance from grid to the cross-section).

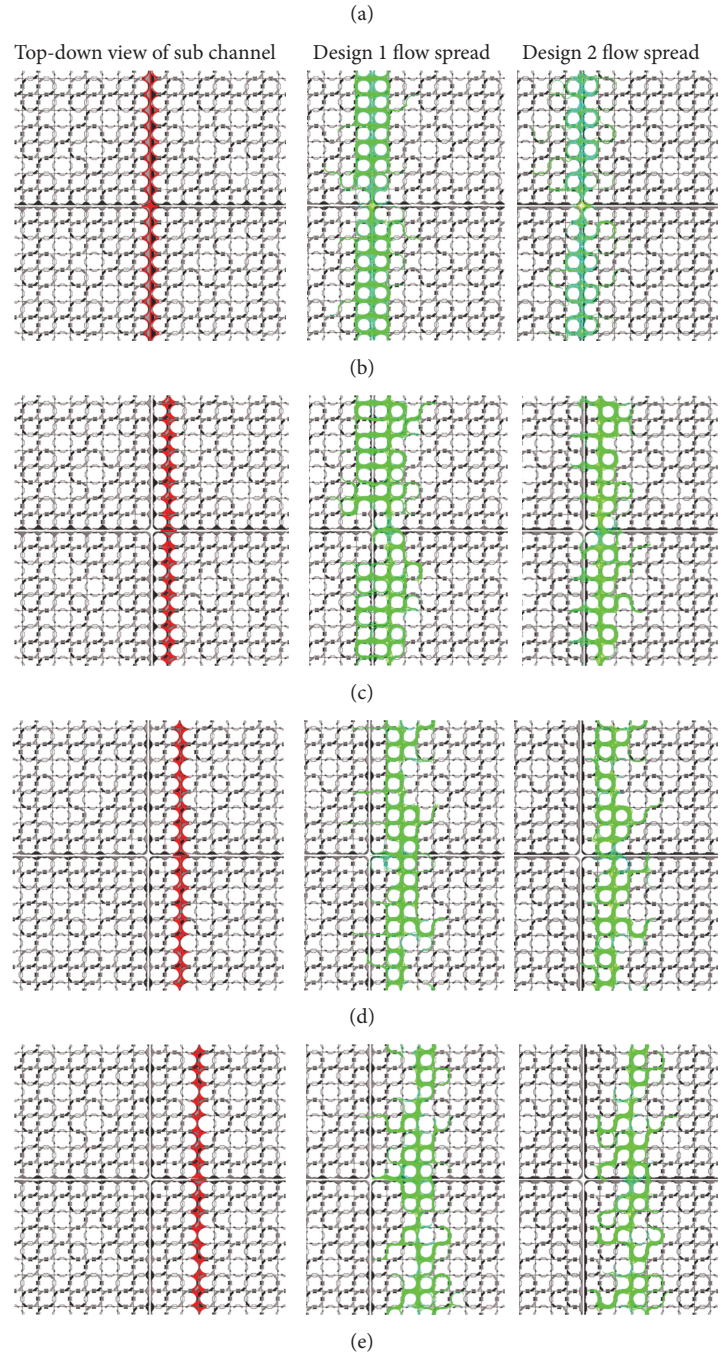
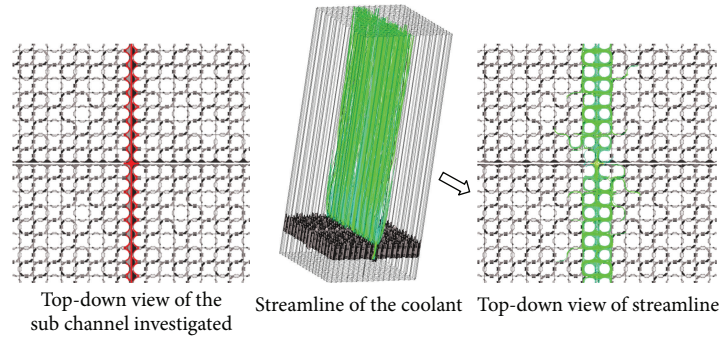


FIGURE 7: Top-down view of streamline at different subchannels near the outer strap.

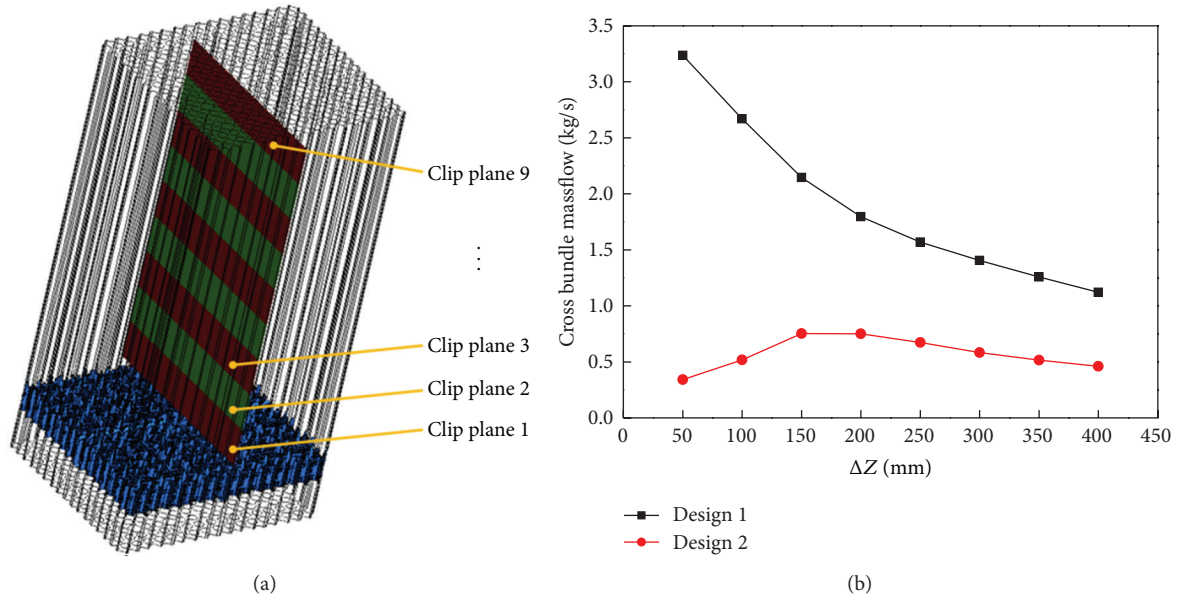


FIGURE 8: Cross-bundle mass flow at different axial location.

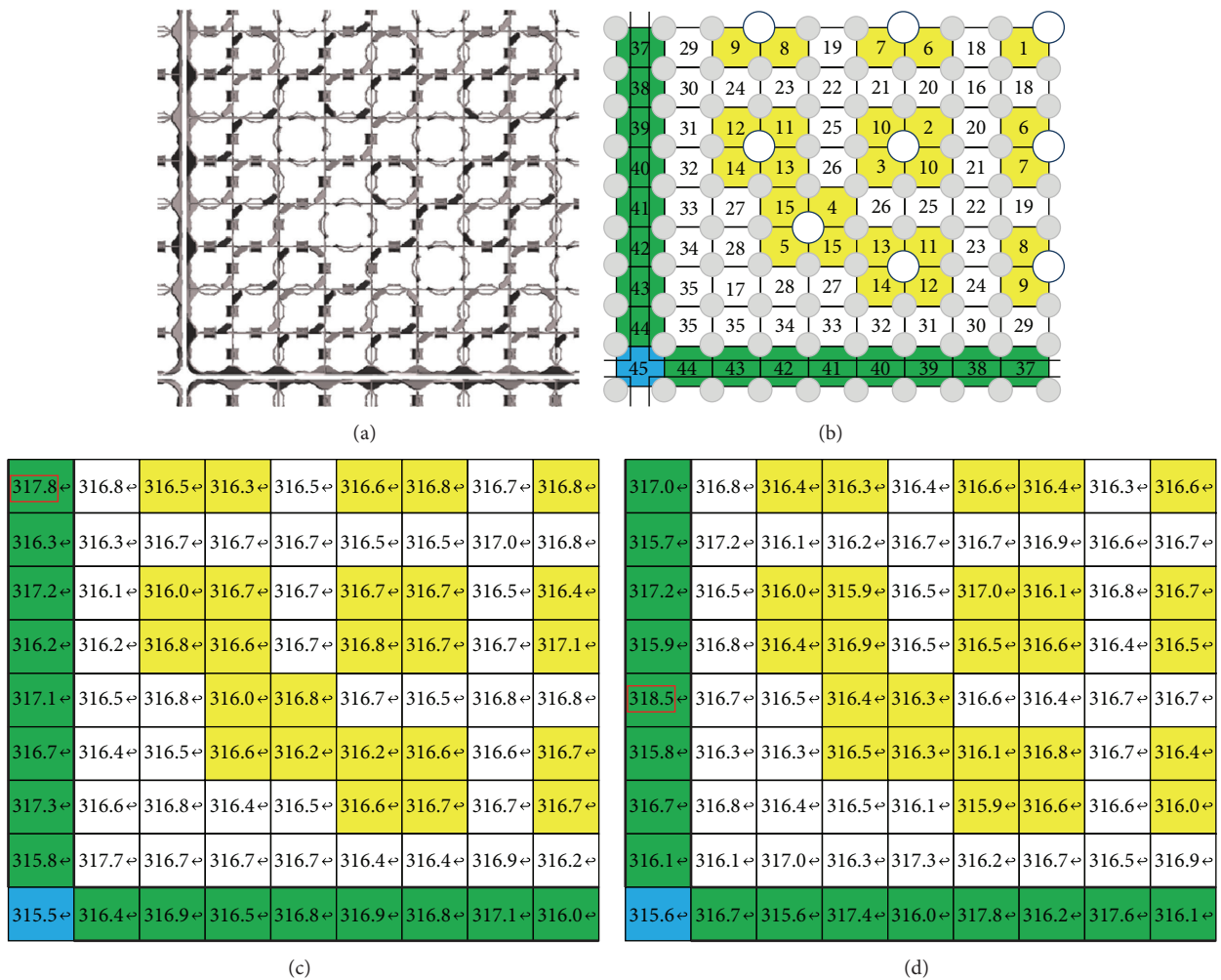


FIGURE 9: Subchannels outlet temperature: (a) outlet location; (b) subchannel numbering; (c) Design 1 temperature, CFX result; (d) Design 2 temperature, CFX result.

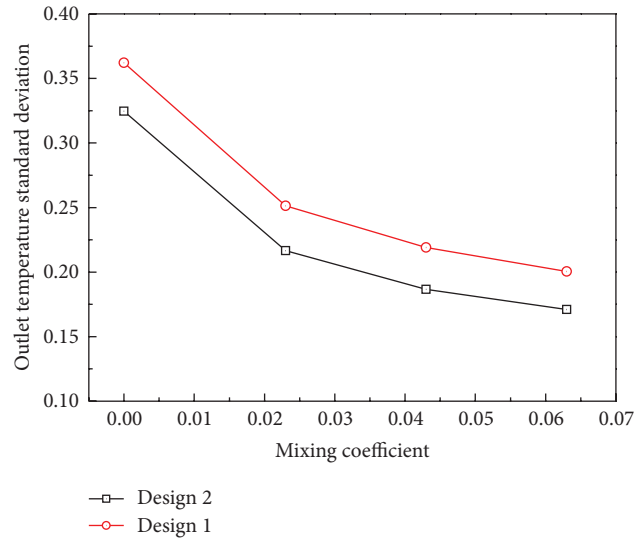


FIGURE 10: Outlet temperature standard deviation variation as mixing coefficient.

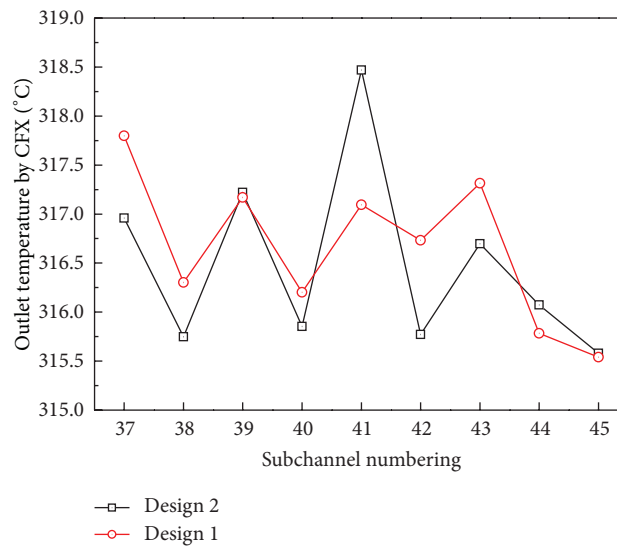


FIGURE 11: Side subchannel outlet temperature calculated in CFX for Design 1 & 2.

the hottest channel of Design 1, subchannel 37, is  $1.6^{\circ}\text{C}$  and for the hottest channel of Design 2, subchannel 41, is  $2.2^{\circ}\text{C}$ . Such big temperature difference (over 10% difference compared to the cross-section averaged temperature rise from inlet to outlet of  $\sim 6^{\circ}\text{C}$ ) between FLICA and CFX results, as well as the  $0.7^{\circ}\text{C}$  difference (or close to 12% variation over the  $6^{\circ}\text{C}$  temperature rise from inlet to exit) between the hottest channels of Design 1 and Design 2 obtained from CFX computation, clearly indicates that subchannel analysis code may miss some useful information in comparison with CFX analysis.

#### 4. Concluding Remarks

Outer straps not only have important effect on enhancing grid mechanical strength and decreasing hang-up susceptibility

but also have significant impact on grid thermal hydraulic performance such as grid pressure drop, lateral flow, and temperature distribution. Due to the larger flow block area of side subchannel of grid Design 2, the pressure drop of Design 2 grid is about 6.9% larger than that of Design 1. The larger side subchannel pressure loss coefficient changes the resistance distribution and subsequently results in larger lateral flow of Design 2 upstream but weaker lateral flow downstream due to the stronger blocking effect of the outer strap. In general, based on the comparison between CFX and FLICA, both computational fluid dynamic method and subchannel analysis code can give reasonable result in single-phase flow simulation, but the application of subchannel analysis code should be very careful because too much geometrical information has been omitted in typical codes.

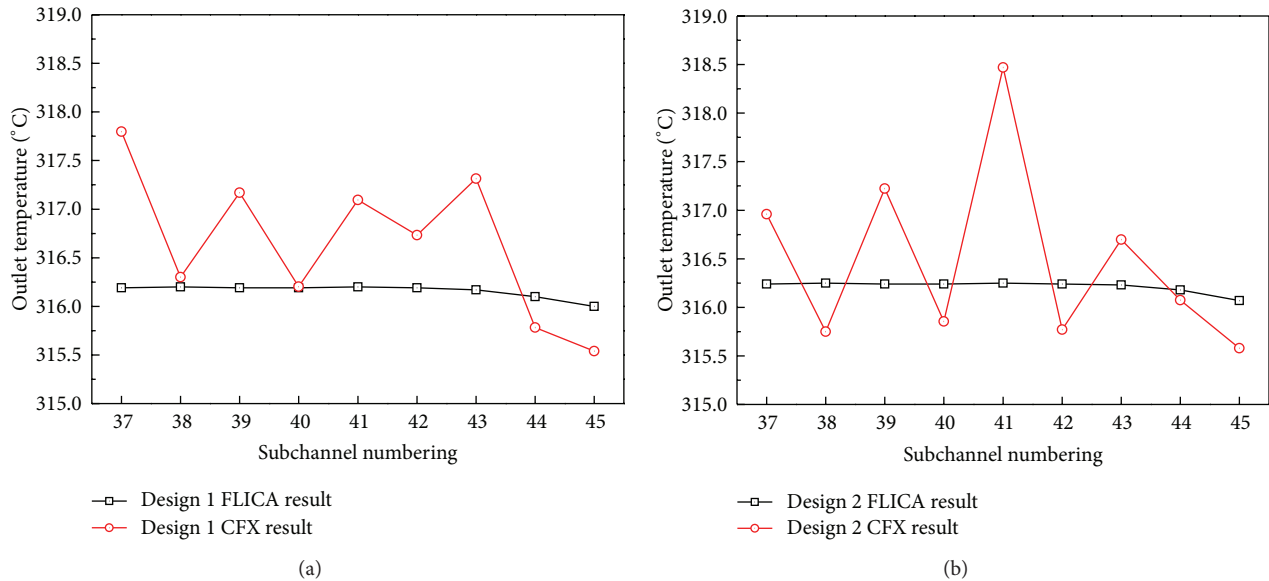


FIGURE 12: Side subchannel outlet temperature in CFX & FLICA (mixing coefficient equal to 0.063) calculation.

## Conflict of Interests

The authors declare that there is no conflict of interests regarding the publication of this paper.

## References

- [1] A. Gandhir and Y. Hassan, "RANS modeling for flow in nuclear fuel bundle in pressurized water reactors (PWR)," *Nuclear Engineering and Design*, vol. 241, no. 11, pp. 4404–4408, 2011.
- [2] C. C. Liu, Y. M. Ferng, and C. K. Shih, "CFD evaluation of turbulence models for flow simulation of the fuel rod bundle with a spacer assembly," *Applied Thermal Engineering*, vol. 40, pp. 389–396, 2012.
- [3] C. C. Liu and Y. M. Ferng, "Numerically simulating the thermal-hydraulic characteristics within the fuel rod bundle using CFD methodology," *Nuclear Engineering and Design*, vol. 240, no. 10, pp. 3078–3086, 2010.
- [4] M. A. Navarro and A. A. C. Santos, "Evaluation of a numeric procedure for flow simulation of a  $5 \times 5$  PWR rod bundle with a mixing vane spacer," in *Proceedings of the International Nuclear Atlantic Conference (INAC '09)*, 2009.
- [5] M. E. Conner, E. Baglietto, and A. M. Elmahdi, "CFD methodology and validation for single-phase flow in PWR fuel assemblies," *Nuclear Engineering and Design*, vol. 240, no. 9, pp. 2088–2095, 2010.
- [6] M. V. Holloway, D. E. Beasley, and M. E. Conner, "Investigation of swirling flow in rod bundle subchannels using computational fluid dynamics," in *Proceedings of the 14th International Conference on Nuclear Engineering (ICONE '06)*, pp. 1–11, Miami, Fla, USA, July 2006.
- [7] M. V. Holloway, D. E. Beasley, and M. E. Conner, "Single-phase convective heat transfer in rod bundles," *Nuclear Engineering and Design*, vol. 238, no. 4, pp. 848–858, 2008.
- [8] W. K. In, T. H. Chun, C. H. Shin, and D. S. Oh, "Numerical computation of heat transfer enhancement of a PWR rod bundle with mixing vane spacers," *Nuclear Technology*, vol. 161, no. 1, pp. 69–79, 2008.
- [9] E. Baglietto and H. Ninokata, "A turbulence model study for simulating flow inside tight lattice rod bundles," *Nuclear Engineering and Design*, vol. 235, no. 7, pp. 773–784, 2005.
- [10] G. Házi, "On turbulence models for rod bundle flow computations," *Annals of Nuclear Energy*, vol. 32, no. 7, pp. 755–761, 2005.